

# Multimodal Chemical Imaging of Amyloid Plaque Pathology in Alzheimer's Disease

Wojciech Michno

Department of Psychiatry and Neurochemistry  
Institute of Neuroscience and Physiology  
Sahlgrenska Academy, University of Gothenburg



UNIVERSITY OF GOTHENBURG

Gothenburg 2019

Cover illustration: Wojciech Michno

Multimodal Chemical Imaging of Amyloid Plaque Pathology in Alzheimer's Disease

© Wojciech Michno 2019

[wojciech.michno@gu.se](mailto:wojciech.michno@gu.se)

ISBN 978-91-7833-568-8 (PRINT)

ISBN 978-91-7833-569-5 (PDF)

Printed in Gothenburg, Sweden 2019

Printed by BrandFactory

To know that we know what we know, and to know that  
we do not know what we do not know, that is true  
knowledge

- Nicolaus Copernicus





# Multimodal Chemical Imaging of Amyloid Plaque Pathology in Alzheimer's Disease

Wojciech Michno

Department of Psychiatry and Neurochemistry, Institute of Neuroscience and Physiology  
Sahlgrenska Academy, University of Gothenburg, Gothenburg, Sweden

## Abstract

Alzheimer's disease (AD) is the most common form of dementia. AD has been linked to the aggregation of amyloid beta (A $\beta$ ) peptides into extracellular deposits, A $\beta$  plaques. These are also found in cognitively unimpaired amyloid-positive (CU-AP) individuals, but these A $\beta$  plaques are primarily diffuse in structure. In AD brains, A $\beta$  plaques often have a dense core and a more diffuse periphery. A $\beta$  exists in various lengths, where the 42 amino acid-long A $\beta$  form (A $\beta$ 1-42) is considered most neurotoxic. A $\beta$ 1-42 is currently used as an AD biomarker when measured in cerebrospinal fluid or plasma. Measurements of the relative amount of different biomolecules within A $\beta$  plaques are generally performed using antibodies. Usually, up to three molecules, can be visualized using this technique. Recently it has been shown that A $\beta$  aggregates can have distinct 3D structures. These differences in structures can be the result of which particular A $\beta$  peptides the aggregates are made of. A $\beta$  aggregates may also differ between AD patients, which makes it difficult to visualize and compare A $\beta$  plaque pathology, and poses challenges in the development of new drugs targeting A $\beta$  aggregates. It is likely that the composition of different A $\beta$  plaques, making them more or less diffuse, could vary depending on different A $\beta$  peptides.

This thesis presents the development of methods to study chemical factors underlying the variation between different types of A $\beta$  plaques. These are mainly based on three advanced technologies. The first is imaging mass spectrometry, which enables the accurate separation and visualization of molecules based on their mass in brain tissue. The second is hyperspectral light microscopy, which utilizes different light wavelengths to characterize the structural properties of A $\beta$  aggregates in different plaque types. The third is high resolution electron microscopy, which enables the visualization of individual aggregates. Furthermore, stable-isotope labelling is used to study the dynamics of A $\beta$  plaque formation. These methods were applied to characterize the biomolecules (different A $\beta$  peptides and lipids) between diffuse and dense structures within and between A $\beta$  plaques in mice, AD patients and CU-AP individuals. It was demonstrated that the shorter A $\beta$ 1-40 peptide localized to the dense core, and, at least in mice, this localization appeared to be a result of A $\beta$  plaque maturation. CU-AP-associated diffuse plaques were not the same as the AD-associated

diffuse or cored plaques, when it came to the aggregation state. The chemical modification of the N-terminal part could be responsible for such structural heterogeneity, and possibly for the neurotoxicity associated with AD. Further, an altered lipid composition was identified between diffuse and dense A $\beta$  aggregate structures. Finally, with the help of stable-isotope labelling, it was verified that A $\beta$  plaque spread starts in the cortex and continues towards the hippocampus. This was initiated through the deposition of A $\beta$ 1-42. Shorter C-terminally truncated peptides were deposited only at a later stage. These peptides were newly produced, and did not stem from already accumulated A $\beta$ 1-42.

In summary, A $\beta$  plaque pathology is much more complex than what it is currently considered during ordinary post-mortem neuropathological assessments. It needs to be researched with the help of advanced methods, to provide us with important information about how, where and why A $\beta$  and other biomolecular factors contribute to the development of AD.

**Keywords:** Alzheimer's disease, beta-amyloid, electron microscopy, imaging mass spectrometry, lipids, luminescent conjugated oligothiophenes, matrix-assisted laser desorption/ionization mass spectrometry (MALDI-MS), molecular imaging, nanoscale secondary ion mass spectrometry (NanoSIMS), neurodegeneration, peptides,

ISBN 978-91-7833-568-8 (PRINT)

ISBN 978-91-7833-569-5 (PDF)

## Sammanfattning på svenska

Alzheimers sjukdom (AD) är den vanligaste demenssjukdomen. AD har kopplats till aggregation och ackumulering av amyloid beta ( $A\beta$ ) peptiden i intra- och extracellulära ansamlingar eller  $A\beta$  plack.  $A\beta$  plack kan också ses hos kognitivt opåverkade amyloid-positiva (CU-AP) individer.  $A\beta$  plack som finns i CU-AP-hjärnor är mestadels diffusa i naturen. I AD-hjärnan har placken ofta en tät kärna och ett mer diffust ytterområde.  $A\beta$  förekommer i flera olika längder (antal aminosyror), där den 42 aminosyror långa  $A\beta$ -peptiden ( $A\beta_{1-42}$ ) anses vara den huvudsakliga neurotoxiska formen. Dess koncentration kan mätas i ryggvätska och blodprover och fungerar då som en AD-biomarkör. Mätning av de relativa mängderna av biomolekyler inom  $A\beta$  plack utförs generellt med antikroppar. Vanligtvis kan upp till tre olika biomolekyler, t.ex.  $A\beta$  peptider av olika längder, visualiseras. Det har nyligen visats att  $A\beta$  aggregat (ansamlingar av  $A\beta$  peptider) kan ha olika tredimensionella (3D) strukturer. Detta kan bero på vilka  $A\beta$  peptider (deras längder), som aggregaten är uppbyggda av.  $A\beta$  aggregat skiljer sig också mellan AD patienter. Detta gör det svårt att visualisera och jämföra  $A\beta$  plack patologin, samt utveckla läkemedel mot  $A\beta$  aggregat. Vidare väcker det tanken att de olika  $A\beta$  placken, som är mer eller mindre diffusa, kan bestå av olika  $A\beta$  peptider.

I denna avhandling presenteras utveckling av metoder som kan användas för att undersöka vilka kemiska faktorer som bidrar till variationen mellan  $A\beta$  plack. Dessa bygger huvudsakligen på tre avancerade tekniker. Masspektrometri-baserad avbildning, som gör det möjligt att extremt noggrant separera molekyler från varandra utifrån deras förhållande mellan massa och laddning, och visualisera deras fördelning direkt i hjärnvävnad, hyperspektral ljusmikroskopi, som utnyttjar ljusets olika våglängder för att karakterisera hur aggregerade  $A\beta$  ansamlingar är, samt högupplösande elektronmikroskopi, som möjliggör visualisering av individuella  $A\beta$  aggregat. Vidare används icke-radioaktiva tunga isotop inmärkning för att studera  $A\beta$  plack formations dynamik.

Dessa metoder applicerades för att karakterisera biomolekyler ( $A\beta$  peptider av olika längder, samt lipider) mellan de diffusa och täta strukturerna inom/mellan  $A\beta$  placken i möss, samt AD patienter och CU-AP individer. Resultaten visade att en kortare  $A\beta$  peptid ( $A\beta_{1-40}$ ) lokaliserades till den täta kärnan av plack. I alla fall i möss, kan detta vara ett resultat av plack åldrande. CU-AP-associerade diffusa plack skiljde sig vad gäller aggregationsgrad och struktur jämfört med både diffusa och täta plack i AD. Kemiska förändringar av den N-terminala delen (början på peptiden) verkade ligga bakom denna strukturella heterogenitet och skulle möjligen även kunna vara associerad med den neurotoxicitet som finns i AD. Vidare identifierades förändrad lipidsammansättning mellan de diffusa och täta  $A\beta$  aggregat. Slutligen, med hjälp av

tunga isotopinmärkning, verifierades det faktum att plackspridning börjar i cortex och fortsätter mot hippocampus. Plackspridningen initierades via deponering av A $\beta$ 1-42, medan kortare C-terminala trunkerade peptider kom först vid ett senare skede. Dessa var nyproducerade och uppkom inte från redan ansamlad A $\beta$ 1-42.

Sammanfattningsvis är det tydligt att A $\beta$  plackpatologin är mycket mer komplex än vad man tidigare har visat vid ordinär neuropatologisk undersökning efter obduktion. Plackuppkomst och utveckling behöver utforskas med hjälp av nya avancerade metoder, för att förse oss med viktig information om hur, var och varför A $\beta$  och andra biokemiska faktorer bidrar till AD utveckling.

# LIST OF PAPERS

This thesis is based on the following studies, referred by their Roman numerals.

- I. Carlred L\*, **Michno W\***, Kaya I, Sjövall P, Syvänen S, Hanrieder J.  
*Probing amyloid- $\beta$  pathology in transgenic Alzheimer's disease (tgArcSwe) mice using MALDI imaging mass spectrometry.*  
J Neurochem 2016; 138(3):469-78. \*contributed equally
- II. **Michno W**, Wehrli PM, Zetterberg H, Blennow K, Hanrieder J.  
*GMI locates to mature amyloid structures implicating a prominent role for glycolipid-protein interactions in Alzheimer pathology.*  
Biochim Biophys Acta Proteins Proteom 2019; 1867(5):458-467
- III. Kaya I, **Michno W**, Brinet D, Iacone Y, Zanni G, Blennow K, Zetterberg H, Hanrieder J.  
*Histology-compatible MALDI mass spectrometry based imaging of neuronal lipids for subsequent immuno-fluorescent staining.*  
Anal Chem 2017; 18;89(8):4685-4694
- IV. **Michno W**, Kaya I, Nyström S, Guerard L, Nilsson KPR, Hammarström P, Blennow K, Zetterberg H, Hanrieder J.  
*Multimodal chemical imaging of amyloid plaque polymorphism reveals A $\beta$  aggregation dependent anionic lipid accumulations and metabolism.*  
Anal Chem 2018; 3;90(13):8130-8138.
- V. **Michno W**, Nyström S, Wehrli P, Lashley T, Brinkmalm G, Guerard L, Syvänen S, Sehlin D, Kaya I, Brinet D, Nilsson KPR, Hammarström P, Blennow K, Zetterberg H, Hanrieder J. *Pyroglutamation of amyloid- $\beta$ -42 (A $\beta$ x-42) followed by A $\beta$ 1-40 deposition underlies plaque polymorphism in progressing Alzheimer's disease pathology.*  
J Biol Chem 2019; 26;294(17):6719-6732.
- VI. **Michno W**, Wehrli P, Sehlin D, Syvänen S, Zetterberg H, Blennow K, Hanrieder J.  
*Chemical imaging of evolving amyloid plaque pathology and associated A $\beta$  peptide aggregation in transgenic AD Mice*  
Submitted to J.Neurochem
- VII. **Michno W**, Stringer K, Escrig S, Enzlein T, Passarelli M, Hopf C, Blennow K, Zetterberg H, Meibon A, Edwards FA, Hanrieder J.  
*Imaging spatial A $\beta$  plaque aggregation dynamics in evolving AD pathology using iSILK.*  
Manuscript

## PAPERS NOT INCLUDED IN THE THESIS

- I. Karlsson O, **Michno W**, Ransome Y, Hanrieder J.  
*MALDI imaging delineates hippocampal glycosphingolipid changes associated with neurotoxin induced proteopathy following neonatal BMAA exposure.*  
Biochim Biophys Acta Proteins Proteom 2017; 1865(7):740-746.
- II. Kaya I, Brinet D, **Michno W**, Syvänen S, Sehlin D, Zetterberg H, Blennow K, Hanrieder J.  
*Delineating amyloid plaque associated neuronal sphingolipids in transgenic Alzheimer's disease mice (tgArcSwe) using MALDI imaging mass spectrometry.*  
ACS Chem Neurosci 2017; 15;8(2):347-355.
- III. Zanni G, **Michno W**, Di Martino E, Tjärnlund-Wolf A, Pettersson J, Mason CE, Hellspong G, Blomgren K, Hanrieder J.  
*Lithium accumulates in neurogenic brain regions as revealed by high resolution ion imaging.*  
Sci Rep 2017; 18;7:40726.
- IV. Kaya I, Brinet D, **Michno W**, Başkurt M, Zetterberg H, Blennow K, Hanrieder J.  
*Novel trimodal MALDI imaging mass spectrometry (IMS3) at 10  $\mu$ m reveals spatial lipid and peptide correlates implicated in A $\beta$  plaque pathology in Alzheimer's disease.*  
ACS Chem Neurosci 2017; 20;8(12):2778-2790.
- V. Jonson M, Nyström S, Sandberg A, Carlback M, **Michno W**, Hanrieder J, Starkenberg A, Nilsson KPR, Thor S, Hammarström P. *Aggregated A $\beta$ 1-42 is selectively toxic for neurons, whereas glial cells produce mature fibrils with low toxicity in Drosophila.*  
Cell Chem Biol 2018; 17;25(5):595-610.e5.
- VI. **Michno W**, Wehrli PM, Blennow K, Zetterberg H, Hanrieder J.  
*Molecular imaging mass spectrometry for probing protein dynamics in neurodegenerative disease pathology.*  
J Neurochem 2018 Jul 24. doi: 10.1111/jnc.14559 (Review)
- VII. Jonson M, Nyström S, Sandberg A, Carlback M, **Michno W**, Hanrieder J, Starkenberg A, Nilsson KPR, Thor S, Hammarström P.  
*Amyloid fibril polymorphism and cell-specific toxicity in vivo.*  
Amyloid 2019; 26(sup1):136-137

# CONTENT

ABBREVIATIONS .....	V
1 INTRODUCTION .....	1
1.1 Dementia, neurodegenerative disorders and protein misfolding .....	1
1.2 Alzheimer's disease .....	2
1.2.1 History and epidemiology .....	2
1.2.2 Clinical symptoms and diagnosis .....	3
1.2.3 Neuropathology .....	6
1.3 Amyloid pathology .....	8
1.3.1 A $\beta$ peptide generation .....	8
1.3.2 A $\beta$ aggregation .....	13
1.3.3 The amyloid cascade hypothesis .....	15
1.3.4 Genetics and AD models .....	17
1.3.5 Other risk factors .....	21
1.3.6 Role of lipids in AD plaque pathology .....	23
1.3.7 A $\beta$ maturation and conformational polymorphism .....	27
2 AIMS .....	30
2.1 General aims .....	30
2.2 Specific aims .....	30
3 METHODS .....	32
3.1 Ethics statements .....	32
3.2 Optical light microscopy .....	32
3.2.1 Confocal microscopy .....	35
3.2.2 Fluorescence microscopy .....	37
3.3 Electron microscopy .....	42
3.3.1 Scanning electron microscope (SEM) .....	46
3.3.2 Transmission electron microscope (TEM) .....	47
3.3.3 Scanning transmission electron microscope (STEM) .....	49
3.3.4 EM preparation of biological samples .....	50

3.4	Mass spectrometry .....	58
3.4.1	Ionization techniques and mass analysers .....	59
3.4.2	Imaging mass spectrometry (IMS) – molecular histology .....	78
3.4.3	Stable isotope labelling with amino acids .....	88
3.4.4	Laser microdissection.....	90
3.5	Immuno-based analysis .....	91
3.5.1	Immunoprecipitation .....	91
3.5.2	Immunohistochemistry.....	94
3.6	Multivariate analysis (MVA).....	99
3.6.1	Principal component analysis (PCA) .....	99
3.6.2	Partial least square (PLS) and orthogonal PLS .....	100
3.6.3	Clustering analysis .....	101
4	RESULTS AND DISCUSSION .....	104
4.1	Paper I.....	104
4.2	Paper II .....	107
4.3	Paper III.....	110
4.4	Paper IV.....	113
4.5	Paper V .....	117
4.6	Paper VI.....	121
4.7	Paper VII.....	124
5	CONCLUSION AND FUTURE PERSPECTIVES.....	127
	ACKNOWLEDGEMENT.....	130
	REFERENCES .....	135



# ABBREVIATIONS

AA	Arachidonic acid
AD	Alzheimer's disease
ADAM	Members of disintegrin and metalloproteinase
AICS	APP intracellular domain
ApoE	Apolipoprotein E
APP	Amyloid precursor protein
Arc	Arctic mutation
A $\beta$	Amyloid $\beta$
BACE	Beta-site APP-cleaving enzyme
BF	Bright field
BSA	Bovine serum albumin
CAA	Cerebral amyloid angiopathy
Cer	Ceramide
CHCA	$\alpha$ -Cyano-4-hydroxycinnamic acid
CR	Congo red
CSF	Cerebrospinal fluid
CTF	C-terminal fragment
CU-AP	Cognitively unaffected-amyloid positive
Da	Dalton
DA	Discriminant analysis
DAN	Diaminonaphthalene

DF	Dark field
DHA	Docosahexaenoic acid
DHAP	Dihydroxyacetophenone
DHB	Dihydroxybenzoic acid
EM	Electron microscopy
EOAD	Early-onset Alzheimer's disease
ESI	Electrospray ionization
fAD	Familial Alzheimer's disease
FFPA	Formalin-fixed paraffin-embedded
FTAA	Formyl thiophene acetic acid
FTICR	Fourier-transform ion cyclotron resonance
GA	Glutaraldehyde
GM	Monosialoganglioside
HexCer	Cerebroside
IHC	Immunohistochemistry
IMS	Imaging Mass Spectrometry
IP	Immunoprecipitation
ITO	Indium tin oxide
LCO	Luminescent conjugated oligothiophene
LMPC	Laser microdissection pressure catapulting
LOAD	Late-onset Alzheimer's disease
MALDI	Matrix-assisted laser desorption/ionization
MAPT	Microtubule associated protein tau gene

MCI	Mild cognitive impairment
MS	Mass spectrometry
MS/MS	Tandem MS
MVA	Multivariate analysis
m/z	Mass-to-charge-ratio
NFT	Neurofibrillary tangles
OCT	Optimal cutting temperature medium
OPLS	Orthogonal partial least squares
PA	Phosphatidic acids
PBS	Phosphate-buffered saline
PCA	Principal component analysis
pE	Pyroglutamate modified
PE	Phosphatidylethanolamine
PET	Positron emission tomography
PFA	Paraformaldehyde
PI	Phosphatidylinositol
PLS	Partial least squares/projection to latent structures
PSEN	Presenilin
PMT	Photomultiplier tube
PTM	Post translational modification
PUFA	Polyunsaturated fatty acids
RMS	Root mean square
ROI	Region of interest

RT	Room temperature
SA	Sinapinic acid
sAD	Sporadic Alzheimer's disease
sAPP	Soluble N-terminal APP fragment
SEM	Scanning Electron Microscopy
SILAC	Stable Isotope labelling with amino acids in cell cultures
SILK	Stable isotope labelling kinetics
SIMS	Secondary Ion Mass Spectrometry
ST	Sulfatide
STEM	Scanning Transmission Electron Microscopy
Swe	Swedish mutation
TEM	Transmission electron microscopy
TIC	Total ion current
TOF	Time-of-flight
UA	Uranyl Acetate

# 1 INTRODUCTION

## 1.1 Dementia, neurodegenerative disorders and protein misfolding

Dementia is a syndrome term that describes a chronic and persistent (lasting more than 6 months) cognitive symptoms severe enough to interfere with a person's daily functioning. These typically include memory loss, reduction of intellectual capabilities, changes in behaviour, decline in social abilities and social withdrawal<sup>1,2</sup>. Advanced age appears to be the greatest contributing factor for dementia. The prevalence increases nearly exponentially after the age of 65 (around 2%), nearly doubling every fifth years, with almost every other person exhibiting dementia symptoms above 90 years of age<sup>3</sup>. Gender appears also to influence the frequency rate of dementia, with elderly females exhibiting higher prevalence<sup>3,4</sup>.

Neurodegeneration defines a pathological process of progressive neuronal dysfunction with loss of neurons ultimately leading to gross atrophy. It is manifested in a variety of clinical symptoms such as amnesia, aphasia, apraxia and agnosia, depending on the brain region that is affected<sup>5</sup>. Progressive neurodegeneration is the main cause of many commonly known neurological diseases, including Parkinson's disease (PD), amyotrophic lateral sclerosis (ALS), Huntington's disease (HD) and Alzheimer's disease (AD). It often leads to dementia, as in the case of AD (the most common cause), or dementia with Lewy bodies (DLB), frontotemporal dementia (FTD) or Creutzfeldt-Jakob disease (CJD).

A common pathological occurrence in many neurological diseases is the progressive accumulation and aggregation of misfolded proteins as extra- and/or intracellular deposits. Native protein folding, a process guided by protein primary amino acid sequence, results in a three-dimensional structure that is necessary for proper protein interaction. The native folding is believed to be the most energetically favourable state, achieved through continuous rearrangement and influenced by the local environment. When misfolded, the protein is recognized by the cellular machinery and rapidly

degraded. Sustained balance between correctly folded proteins and degradation of misfolded ones is necessary for maintenance of cell function<sup>6</sup>. If failure to degrade a misfolded protein occurs, multiple copies of the proteins might stick together and begin to aggregate<sup>7,8</sup>. This leads to the formation of larger intracellular and extracellular insoluble fibrillary deposits, referred to as amyloid<sup>9</sup>. Indeed, amyloid formation and deposition is characteristic for many neurodegenerative that share similar morphological features, even though the aggregates themselves comprise a variety of different proteins<sup>7,10</sup>. This is also the case for the earlier mentioned dementias, including AD, DLB, FTD and CJD. The presence of amyloid appears however not to be necessary for development of dementia, as for instance in the case of Vascular dementia, or dementias as result of infections, e.g. herpes simplex virus.

## 1.2 Alzheimer's disease

### 1.2.1 History and epidemiology

Alzheimer's disease is the most common type of dementia. It was first described in 1901 by a German physician at the Frankfurt Psychiatry Hospital, Dr. Alois Alzheimer, in a 50-years-old woman Auguste Deter who suffered early clinical symptoms of the disease<sup>11</sup>. Dr. Alzheimer followed symptomatology and progression of Auguste Deter's condition and after her death in 1906 he also investigated the morphology and histopathology of her brain. *Post-mortem* examination revealed severe atrophy, neuronal tangles, extracellular aggregates, lipid droplets, and signs of inflammation. He reported these findings later that year at a meeting in Tübingen, and published them in 1907<sup>12</sup>. Few years later, the condition was reported as a separate disease, a subtype of senile dementia, by Dr. Emil Kraepelin in Leipzig<sup>13</sup>.

Over the years the medical nomenclature has changed and became refined based on better understanding, classification of the disease, and differential symptoms and diagnosis. Currently, the disease is typically divided into early-onset AD (EOAD) and late-onset AD (LOAD). EOAD comprises primarily cases with inherited, rare genetic form of AD, referred to as familial AD (fAD), that affects people younger than 65 years<sup>2</sup>. While some non-genetic cases of EOAD occur, the majority of the non-genetic

cases are considered Late-onset AD (LOAD), also known as sporadic AD (sAD)<sup>2</sup>. These affect people above the age of 65 years. The sAD is considered the most common type of dementia, even though the actual causes of the disease remain unknown<sup>2,14</sup>.

Today 1 in 3 elderly die from AD or other dementias, with AD accounting for almost 80% of all dementia cases<sup>3,15</sup>. The disease kills more than breast cancer and prostate cancer combined, and is the 6<sup>th</sup> leading cause of death in the world<sup>3</sup>. While the rate of, for instance, heart diseases has decreased by almost 15% since 2000, the rate of AD has increased by almost 90%<sup>3</sup>. One of the main causes of this rise in AD is the growing geriatric population (particularly in developed countries), which remains the main risk factor for sAD. In the US, this factor is estimated to contribute to a rise in the number of people with AD from a current 5.2 million to almost 16 million cases by 2050<sup>3</sup>. This puts immense costs and strains on society, with the estimate of an increase in annual cost from the current \$250 billion, to over \$1 trillion by 2050<sup>3</sup>. This makes the current cost of treating AD and other forms of dementia more expensive than the treatment of cancer and equal to that of heart diseases<sup>3</sup>.

## **1.2.2 Clinical symptoms and diagnosis**

Initially patients who suffer from AD experience mild memory impairments, especially in episodic memory, which may be accompanied by other symptoms such as depression. These symptoms are often “unnoticed”, develop slowly and worsen over time. At later stages, cognitive symptoms such as confusion, general behavioural changes, impaired judgement, and finally problems with motor functions and speech develop<sup>2,16,17</sup>.

Until today there is no single test to diagnose AD or other forms of dementia. Rather, the diagnosis is made based on the history of the patient, mental status and mood testing, physical and neurological examination, and variety a of medical tests of blood and cerebrospinal fluid (CSF) in order to rule out alternative causes of dementia.

The cognitive functions are typically judged based on CERAD (Consortium to Establish a Registry for Alzheimer's Disease)<sup>18,19</sup>, however other methods of

assessment such as MMSE (Mini-Mental State Examination)<sup>20</sup>, CDR (Clinical Dementia Rating Scale Sum of Boxes)<sup>21</sup>, and BDRS (Blessed Dementia Rating Scale)<sup>22</sup> are also used. In combination with other assessments, the disease is then diagnosed following the revised criteria of NINCDS-ADRDA (National Institute of Neurological and Communicative Disorders and Stroke and the Alzheimer's Disease and Related Disorders Association)<sup>23</sup> and/or DSM-IV-TR (Diagnostic and Statistical Manual of Mental Disorder)<sup>24</sup>. Progression of AD is typically categorized into preclinical stages, followed by mild cognitive impairment (MCI) and finally full blown AD dementia, however the progression spectrum is very diversified<sup>2</sup>.

Given that brains of AD patients display characteristic neuropathological features including A $\beta$  and tau aggregates (discussed in detail in section 1.2.3), as well as brain atrophy, the clinical assessment is now complemented with imaging techniques and neurochemical techniques to examine, biological-, molecular- and metabolic-, as well as structural-changes associated with the disease.

Analyses of AD-related biomarkers in CSF are becoming increasingly common in guiding clinical diagnosis, assessment of disease risk or progression, and monitoring of eventual treatments. Here CSF concentration of total tau (T-tau) and phosphorylated tau (P-tau<sub>181</sub>) and A $\beta$ <sub>42</sub> are commonly used<sup>25-27</sup>. While increased levels of both T-tau and P-tau<sub>181</sub> reflect general neuronal and axonal damage associated with the neurodegeneration<sup>26-29</sup>, P-tau<sub>181</sub> provides additional information about altered phosphorylation and is a good predictor of increased deterioration rate of AD patients<sup>30</sup>. On the other hand decreased CSF levels of A $\beta$ <sub>42</sub> reflect the brain A $\beta$  aggregation and accumulation<sup>26,27,31</sup>.

In addition to these classical biomarkers, other proteins, lipids and metabolites, including synaptic proteins, signalling molecules, markers of inflammation and many others, alone or in combination, are being evaluated for their diagnostic value in CSF<sup>25</sup>. Given the limited applicability of CSF biomarkers due to the need of a lumbar puncture for collection, evaluation of biomarkers in blood is under development, for



detailed review see Hampel et al<sup>32</sup>. While certain lipids and metabolites have shown promising results, the reliability of these techniques has not been proven so far.

Alongside fluid biomarkers, static imaging techniques, such as non-enhanced computed tomography (CT), and magnetic resonance imaging (MRI), as well as dynamic, temporally resolved imaging techniques, including functional MRI (fMRI), positron emission tomography (PET) and single photon emission computed tomography (SPECT), have been shown to be useful for *in vivo* evaluation of structural, respective functional and metabolic changes in variety of brain regions.

Here MRI (CT is often no longer used) has been shown useful for high resolution evaluation of brain atrophy and shrinkage<sup>33-35</sup>. Measurement of brain activity caused by changes in oxygen levels during blood flow using MRI<sup>36</sup>, measurement of metabolic processes through positron emission in PET<sup>37</sup> and gamma emission in SPECT<sup>38,39</sup>, all provide functional and/or metabolic information about any alterations in physiological processes associated with AD. They are extensively used for research and, in some cases, for diagnosis<sup>40</sup>. Each technique offers its own advantages but all are nowadays combined in order to improve their diagnostic properties.

In AD, PET has become commonly adapted technique, with the possibility to directly and indirectly monitor AD associated changes. Direct monitoring of metabolic activity of neurons is typically performed using radioactive fluorine-18-labelled fluorodeoxyglucose (FDG-PET)<sup>37,41</sup>. Indirect visualization of, for instance, A $\beta$  plaques, is accomplished thanks to the development of ligands, and also antibodies, conjugated to the radioactive tracers (<sup>11</sup>C or <sup>18</sup>F, the latter of which exhibits longer half-life), such as Pittsburgh compound B (PiB) based <sup>11</sup>C-PiB<sup>42</sup> or the close structural analogue, <sup>18</sup>F-flutemetamol<sup>37,43,44</sup>. While the imaging techniques proved robust, and provide the most information about brain related changes, they are expensive, involve radiation exposure, and are yet not readily accessible.

Both the fluid biomarkers and the imaging techniques provide us with general trends related to biological, molecular/metabolic and structural changes over the course of aging. These methods are constantly refined and are gradually incorporated into

revised diagnosis criteria. The definite diagnosis of a suspected AD patient is however performed first *post-mortem* after a careful neuropathological examination and assessment of AD staging based on cerebral profile of A $\beta$  aggregates as plaques and tau aggregates in form of neurofibrillary tangles (NFT) is performed.

### **1.2.3 Neuropathology**

Macroscopic pathological features of AD comprise a general reduction in cortical brain volume, referred to as atrophy, most prominent in parietal and temporal lobes, as well as widened sulci and enlarged ventricles. On a microscopic scale, neurofibrillary tangles (NFTs) and plaques are the main lesions present in AD<sup>45</sup>.

NFTs are intracellular deposits composed mainly of truncated and hyperphosphorylated microtubule-associated protein tau. In AD, tau becomes truncated and excessively phosphorylated. It then loses its ability to bind to and stabilize microtubules, misfolds and begins to aggregate<sup>2,45,46</sup>. This loss of function may be induced by plaque pathology, and has been suggested to underlie the axonal and dendritic breakdown, and eventually neuronal loss, that occurs in AD.

Extracellular plaques are composed mainly of A $\beta$  peptide, produced from sequential cleavage of amyloid precursor protein (APP) (discussed below), and are hence commonly referred to as A $\beta$  plaques<sup>45,47-49</sup>. These deposits are typically divided into dense cored plaques, often referred to as “congophilic” based on their detection with Congo Red (CR) stain, and diffuse plaques, which cannot be visualized with CR<sup>50</sup>. The former, dense cored plaques, are the dominating type of A $\beta$  plaque pathology in AD patients<sup>51</sup>. They are associated with dystrophic neurites, signs of inflammation, activated microglia and astrocytes, as well as a general loss of synapses and neurons<sup>52,53</sup>. Diffuse plaques are, on the other hand, more common in non-demented, cognitively normal elderly individuals, a pathological condition previously referred to as pathological aging, and nowadays as cognitively unaffected amyloid positive (CU-AP)<sup>54</sup>. Most AD patients (and some CU-AP individuals) also display aggregation of A $\beta$  peptides on the walls of arteries, a condition referred to as cerebral amyloid angiopathy (CAA)<sup>45</sup>.

In line with the high hydrophobicity and consequently increased aggregation propensity of the A $\beta$ <sub>1-42</sub> peptide (42 amino acid-long peptide)<sup>55</sup>, A $\beta$  plaque formation has been shown to involve N-terminal truncated A $\beta$ <sub>x-42</sub> peptides<sup>45,56-58</sup>. The shorter, less hydrophobic A $\beta$ <sub>1-40</sub> peptide has been suggested to be present particularly in cored plaques as observed in AD<sup>56,57,59,60</sup>, and to be a necessary constituent of the CAA (nature of A $\beta$  peptides discussed below)<sup>56,61</sup>. The exact differences in the peptide composition of individual plaque morphotypes remains unknown.

Further, A $\beta$  plaque pathology has long been believed to result from extracellular aggregation of the A $\beta$  peptide. Recent studies have however suggested a potential, intracellular origin of the A $\beta$  peptide aggregation, as highlighted by in vitro studies and histological assessment of brain tissue<sup>62,63</sup>. Therefore, potential mechanisms and factors that influence such proposed plaque “aging”, or the alternative independent aggregation pathway, as well as the origin for primary plaque deposition remain controversial.

Stereotypical spatiotemporal distribution of NFT and A $\beta$  plaque pathology differs in AD and have been described extensively by Braak & Braak and Thal et al respectively. The NFTs spread “outwards” in 6 stages starting from locus coeruleus, transenthorinal and enthorinal regions (stages I, II), progressing to the limbic system, with the innermost neocortical areas and hippocampal formation (III, IV), and finally spreading to the isocortical areas, including primary and secondary sensory and motor areas of the neocortex (V, VI). This pathological spread correlates well with the cognitive decline in AD patients<sup>64-66</sup>.

The spread of the A $\beta$  plaque pathology on the other hand can be considered an “inward” progression that occurs in 5 stages, with the isocortical areas being affected first (stage I), followed by the limbic system and allocortical structures, including the rest of the neocortex, hippocampal formation, basal nuclei, diencephalon and amygdala (II, III), and lastly spreading to subcortical structures, including mesencephalon, pons, and cerebellar cortex (IV, V). The progression of the disease does not correlate with either the spread or size of the A $\beta$  plaques<sup>64,66,67</sup>.

## 1.3 Amyloid pathology

### 1.3.1 A $\beta$ peptide generation

Amyloid  $\beta$  (A $\beta$ ) has been identified to be critical in initiating and driving AD pathology leading to downstream processes including Tau pathology, synaptic changes and neurodegeneration. A $\beta$  is a product of sequential cleavage of amyloid precursor protein (APP) by the  $\beta$ - and  $\gamma$ -secretase<sup>2,68,69</sup>.

#### 1.3.1.1 APP processing pathways

Amyloid precursor protein (APP) is a receptor-like transmembrane protein that comprises a large extracellular N-terminal domain, and a smaller, intracellular C-terminal domain<sup>70</sup>. The most commonly expressed isoforms are APP695, APP751 and APP770 (these are 695, 751 and 770 amino acid-long proteins) with APP695 being the predominant variant expressed in neurons<sup>71,72</sup>. In addition, paralogues of APP, known as amyloid precursor-like proteins, characterized by their lack of A $\beta$  domain, exist in mammals<sup>73</sup>.

APP has been suggested to be involved in a variety of neuronal functions, including neurogenesis and neuronal differentiation, neurite outgrowth and branching, as well as synaptogenesis<sup>74</sup>. While some of the APP localizes to the cell surface, the majority of it localizes to the Golgi complex or is internalized into endosomes, either to be recycled back to neuronal surface or to be targeted for lysosomal degradation<sup>74-77</sup>.

APP is sequentially cleaved by several proteases along two major pathways, commonly referred to as the non-amyloidogenic and the amyloidogenic pathways (Figure 1)<sup>76,78</sup>. Three major classes of enzymes have been shown to be involved in these two pathways, the  $\alpha$ - and  $\beta$ -secretases (non-amyloidogenic pathway), and  $\beta$ - and  $\gamma$ -secretases respectively (amyloidogenic pathway)<sup>78,79</sup>.

The members of a disintegrin and metalloproteinase (ADAM) enzyme family, are cell-membrane expressed proteases that are responsible for the  $\alpha$ -secretase cleavage within the brain<sup>80</sup>. Their processing of APP is protein kinase C (PKC)-regulated. ADAM-mediated processing of APP occurs mainly at the neuronal surface, and only to some

extent in the trans-Golgi network (TGN)<sup>81,82</sup>. In addition to APP,  $\alpha$ -secretases are also involved in processing of several other substrates, including interleukin 6 (IL-6) and tumour necrosis factor (TNF), both implicated in AD<sup>77</sup>.

The beta-site APP-cleaving enzymes 1 and 2 (BACE1/BACE2), also known as Asp-2 and memapsin-2, are ubiquitous transmembrane enzymes, members of the pepsin family of aspartyl proteases responsible for  $\beta$ -secretase activity<sup>83-85</sup>. While the brain enriched BACE1 is involved in cleavage of APP to produce A $\beta$ , the expression of BACE2 is much lower and its activity results in cleavage within the A $\beta$  sequence<sup>86,87</sup>. BACE1 is active mainly in TGN and the endosome, where its activity is favoured by the acidic environment<sup>84,88</sup>. Some of the activity also occurs at the neuronal surface<sup>84,85</sup>. Recently, the lysosomal cysteine protease cathepsin B has also been suggested to have  $\beta$ -secretase activity<sup>89,90</sup>. This protease may be involved in the production of pyroglutamylated (pE) forms of A $\beta$ , formed when N-terminal glutamate is cyclized by glutaminyl cyclase<sup>91,92</sup>.

The  $\gamma$ -secretase is a multi-subunit protease complex that consists of four individual proteins: presenilin 1 or 2 (PSEN1/PSEN2), nicastrin (NCSTN), anterior pharynx defective 1 (APH1), and presenilin enhancer 2 (PEN2)<sup>93,94</sup>. When activated,  $\gamma$ -secretase cleaves off the C-terminal fragment of APP to generate A $\beta$ <sup>83,95,96</sup>. As this cleavage can occur at multiple positions, several A $\beta$  species of different lengths can be generated<sup>83,96</sup>. The activity of  $\gamma$ -secretase has been shown to occur within various subcellular units, and the cleavage sites have been suggested to depend on the subcellular localization and conditions<sup>68,78,83,97,98</sup>.

Processing of APP695 (predominant in neurons) along the non-amyloidogenic pathway is characterized by  $\alpha$ -secretase-mediated cleavage within the A $\beta$  domain, which results in a short intracellular and a long extracellular fragment<sup>78,79</sup>. The short intracellular fragment is an 83 amino acid-long C-terminal fragment (known as CTF $\alpha$  and C83), which spans the APP intracellular domain (AICD), including its YENPTY interaction motif, as well as p3 peptide (A $\beta$ 17-42) region that is sequentially cleaved off by  $\gamma$ -secretase<sup>70,77</sup>. The longer, soluble extracellular N-terminal fragment (sAPP $\alpha$ )

consists of the heparin-binding domain (HBD) and the copper-binding domain, shown to bind both copper and zinc (CuBD), together referred to as a cysteine-rich globular E1 domain; an acid domain (AcD), a second heparin binding domain (HPD2) and a random coil region, together referred to as a helix rich E2 domain; as well as the remaining A $\beta$  peptide region (A $\beta$ 1-16)<sup>70,99-102</sup>. The APP751 and APP770 contain, respectively, an additional Kunitz-type protease inhibitor (KPI) domain, or both KPI and an Ox2 region, located between the E2 and Ac domain<sup>70,72</sup>.

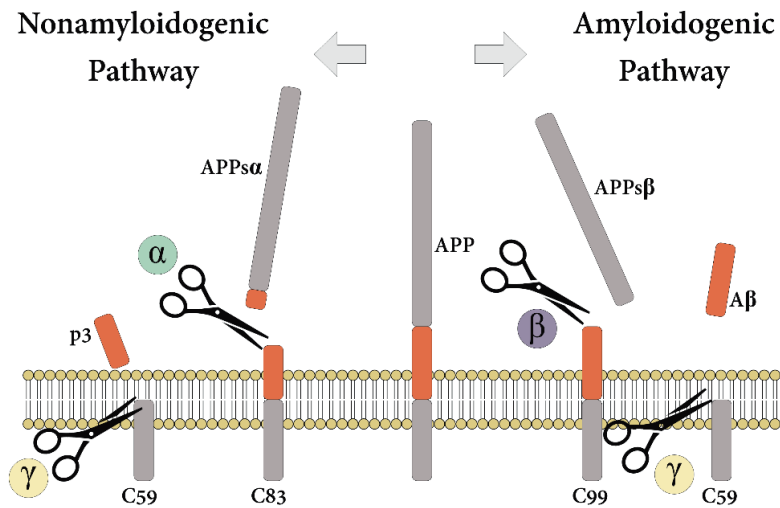


*Figure 1. Schematic of the APP processing by either:  $\alpha$ - and  $\gamma$ -secretase through non-amyloidogenic pathway (left), and  $\beta$ - and  $\gamma$ -secretase in amyloidogenic pathway (right). Both pathway result in generations of soluble N-terminal fragments (sAPP $\alpha$  or sAPP $\beta$ ), and either p3 fragment or the amyloid-forming A $\beta$  peptide.*

If instead APP is processed along the amyloidogenic pathway,  $\beta$ -secretase cleaves APP into a shorter 99 amino acid long C-terminal fragment (known as CTF $\beta$  and C99), which is sequentially processed by  $\gamma$ -secretase into AICD and intact A $\beta$  peptide, as well as a longer soluble N-terminal fragment (sAPP $\beta$ )<sup>70,78,79</sup>. As a result of the predominant activity of  $\beta$ - and  $\gamma$ -secretase within the cell, the majority of APP processing to generate A $\beta$  peptides (along the amyloidogenic pathway) occurs within the intracellular compartments<sup>77</sup>. Cell surface-processing of APP on the other hand, proceeds through the non-amyloidogenic pathway<sup>77,88</sup>.

In addition to these three secretases, novel  $\delta$ -secretase,  $\eta$ -secretases, and meprin  $\beta$  have been recently discovered as additional APP proteases<sup>103</sup>. Here, asparagine endopeptidase (AEP) and matrix metalloproteinase MT5-MMP, a  $\delta$ -secretase respective  $\eta$ -secretase, have been suggested to result in production of proteolytic fragments that contribute to the AD pathology<sup>104,105</sup>. Likewise, meprin  $\beta$ , which is a zinc metalloprotease, has been also been linked to AD, through its generation of A $\beta$ 2-X peptides and potential  $\beta$ -secretase activity<sup>106</sup>.

### 1.3.1.2 Amyloid $\beta$ truncations and homeostasis

A $\beta$  exists in over 15 different isoforms and truncations with varying length of the amino acid sequence<sup>107</sup>. Depending on the site of  $\gamma$ -secretase cleavage, the C-terminal can vary in length, ending anywhere from amino acid 37 to 43<sup>68,69</sup>. The most common isoforms are, however, the A $\beta$ x-38, A $\beta$ x-40, and A $\beta$ x-42<sup>68,96</sup>. The N-terminal part of the A $\beta$  peptide also varies, with A $\beta$ 1-x, A $\beta$ 3-x, A $\beta$ 4-x, A $\beta$ 5-x, and A $\beta$ 11-x as common truncations<sup>68,69</sup>. The A $\beta$ 3-x and A $\beta$ 11-x truncated peptides have been shown to result from  $\beta$ -secretase activity<sup>68</sup>. In addition, these N-terminal glutamate residues (A $\beta$ 3-x and A $\beta$ 11-x), get cyclized to form pyro-glutamylated forms of A $\beta$ , the A $\beta$ pE3-x and A $\beta$ pE11-x, both of which have been frequently detected in brains of AD patients<sup>108,109</sup>.

As most of other naturally synthesized peptides, A $\beta$  production is normally balanced by its enzymatic degradation and/or clearance<sup>110</sup>, but its concentration has been shown to naturally become elevated in an age-dependent manner<sup>111</sup>. In the non-pathological state, A $\beta$  has been shown to have a short half-life of a few hours<sup>112,113</sup>. Therefore, it has been hypothesized that non-genetic sporadic AD (sAD) is caused by the imbalance in the A $\beta$  production and clearance<sup>114,115</sup>. This, in turn would lead to its aggregation and exertion of a wide variety of neurotoxic effects, eventually resulting in A $\beta$  plaque formation. Recent studies of A $\beta$  turnover rate in CSF has indeed shown such a misbalance in sAD patients<sup>116</sup>. The cause of impairment and precise components of the clearance mechanism that underlie this misbalance remain unknown.

A $\beta$  is normally degraded by a wide variety of enzymes<sup>110</sup>. This depends on protease related factors, such as their subcellular localization, optimal working pH, and many other A $\beta$  related factors, such as its source and location<sup>110,117</sup>. Further, the dynamic equilibrium of the A $\beta$  peptide, between various interconnected compartments, and between its passive and active transport, will affect the relative A $\beta$  levels at various sites<sup>110</sup>. An example of this is the decreased CSF levels of A $\beta$ , believed to correspond to aggregation of the peptide in the brain<sup>26,31</sup>. Finally, proteases responsible for A $\beta$  degradation also have their specific substrates, including non-aggregated and/or aggregated A $\beta$ <sup>110</sup>. Combined, all these factors will affect the overall concentration of the peptide (and possibly its isoforms), at different sites.

Two of the major A $\beta$  degrading enzymes, both degrading non-aggregated A $\beta$ , are the metalloproteases neprilysin (NEP) and the insulin degrading enzyme (IDE)<sup>110,118</sup>. NEP degrades A $\beta$  in Golgi, the endoplasmic reticulum and the extracellular space<sup>110,118,119</sup>. IDE, on the other hand, plays a major role in cytosolic, endosomal, lysosomal, extracellular and, in particular interstitial A $\beta$  degradation<sup>110,117,120</sup>. Other proteases able to degrade fibrillary (and oligomeric) A $\beta$  include matrix metallopeptidase 2 and 9 (MMP2 and MMP9), active in the extracellular space, Golgi and endoplasmic reticulum; the cysteine protease - cathepsin B (mentioned earlier in relation to its  $\beta$ -secretase activity), active in the extracellular space, lysosome and endosome; and the aspartyl protease - cathepsin D, active in endosomes and lysosomes<sup>110,118</sup>.

Under physiological conditions, A $\beta$  is believed to be present at picomolar (pM) concentration<sup>121</sup>. While the precise physiological role of A $\beta$  remains unclear, it is believed to be involved in several cellular processes. Low A $\beta$  concentration has been suggested to possess trophic properties, exhibiting anti-oxidant activity, including metal ion sequestration, playing a role in neurogenesis and in calcium homeostasis, and maintaining the structural integrity of the blood-brain barrier (BBB)<sup>122</sup>. Further, studies have shown a low concentration of A $\beta$  to be important in modulation of synaptic activity and plasticity, thereby having an effect on the memory and learning<sup>121,123</sup>. Clear alterations of these processes are related to higher than physiological levels of A $\beta$ , and represent physiological changes observed in AD patients<sup>2,122,124</sup>.



### 1.3.2 A $\beta$ aggregation

A common feature of all amyloidogenic proteins is the presence of a hydrophobic component (that consists of hydrophobic amino acids). In the case of A $\beta$ , the aggregation propensity has been attributed to two highly hydrophobic components, the C-terminal end of the peptide, and the so-called KLVFF motif that is present in the mid-region of the peptide <sup>125-128</sup>.

The initial stage of A $\beta$  aggregation is the formation of a  $\beta$ -hairpin, as result of the C-terminal region folding onto the mid-region of the peptide <sup>125,126,128</sup>. Here, the longer peptides are more prone to aggregate than the shorter ones <sup>125,129</sup>. This folding process itself is believed to depend on the aromatic-stacking interaction of the two phenylalanine residues present in the KLVFF<sub>17-21</sub> (lysine-leucine-valine-phenylalanine-phenylalanine) amino acid motif. These aromatic moieties stabilize both intramolecular (within a single  $\beta$ -hairpin) and intermolecular interactions in a larger assembly <sup>127,130,131</sup>. Further, the salt bridge (hydrogen bond and electrostatic interaction) between the anionic carboxylate (RCOO<sup>-</sup>) of D<sub>23</sub> (aspartic acid) and cationic ammonium (RNH<sub>3</sub><sup>+</sup>) of K<sub>28</sub> (lysine) further stabilizes the loop region <sup>132,133</sup>.

Subsequent aggregation of multiple  $\beta$ -hairpins, along with conformational rearrangements and formation of hydrogen bonds between adjacent strands, results in the formation of first dimers, and later different oligomers (Figure 2) <sup>126,128,134,135</sup>. The pattern present in this assembly can be parallel, with the same directions of C-terminus and N-terminus on the adjacent strands, anti-parallel, with opposite directions, or with both parallel and anti-parallel patterns being present in larger assemblies <sup>135,136</sup>. If the formation of oligomerization stops, the process is referred to as off-pathway aggregation <sup>137-139</sup>. Otherwise, aggregation continues along the fibrillogenic pathway <sup>126,128,135</sup> and eventually leads to the formation of  $\beta$ -sheet structures, stacked in either parallel or anti-parallel way, that build up protofibrils <sup>128,136,140,141</sup>. Finally, two or more protofibrils can twist around one-another, leading to formation of fibrils. This is considered the end state of fibrillogenic aggregation <sup>127,128,141</sup>.

Interestingly, the  $\beta$ -sheets organization (parallel/anti-parallel) has been suggested to be subject to structural rearrangement between aggregation states <sup>135,136</sup>. Further, it has been proposed that this structural rearrangement may depend on which A $\beta$  peptides are involved. While the collapsed (stacked  $\beta$ -sheets) conformation of A $\beta$  1-42, and the extended state (anti-parallel  $\beta$ -sheets) of A $\beta$  1-40 <sup>140</sup> result in the assembly of protofibrils with a similar structure <sup>135</sup>, the continuation of this self-aggregation process results in the formation of mature A $\beta$  fibrils with different  $\beta$ -sheet organization within each fibrillary layer <sup>142</sup>. Here, the most thermodynamically stable conformation for A $\beta$  1-40 fibrils has been shown to be a three-fold conformation comprising three  $\beta$ -sheets in each layer of the fibril <sup>142</sup>. This imposes a major challenge to any form of conformation specific antibody detection of aggregated A $\beta$ .

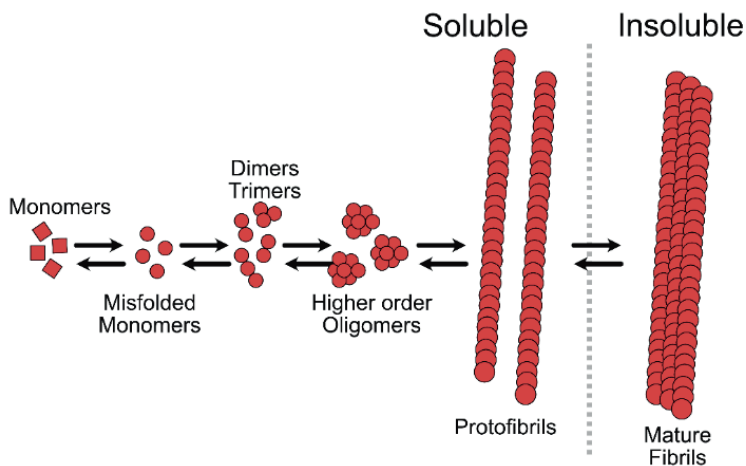


*Figure 2. Simplified overview of aggregation process of A $\beta$ . The monomers become misfolded and aggregate into low order aggregates (such as dimers and trimer), then higher order oligomers, and eventually protofibrils. Multiple protofibrils can aggregate and form long, insoluble mature fibrils.*

Based on whether extracted aggregates of A $\beta$  remain in the aqueous phase following high speed centrifugation, they are referred to as “soluble” or “insoluble” A $\beta$  aggregates <sup>143</sup>. All forms of A $\beta$  aggregates prior to fibrils are considered soluble. For extraction of insoluble aggregates, detergents and acids, such as 70% formic acid, are used. This concept has become widely applied since the identification of cognitively unaffected amyloid positive (CU-AP) patients who display both A $\beta$  plaque pathology

Whole brain extracts (combined “insoluble” and “soluble” A $\beta$  extracts) of CU-AP (previously referred to as pathological aging) and AD patients have suggested an overlapping A $\beta$  peptide profile between two groups<sup>144,145</sup>, but higher levels of A $\beta$ 1-40 were found to be present in CU-AP<sup>144</sup>. Interestingly, in a study where soluble and insoluble fractions were separated, 10-fold higher levels of insoluble A $\beta$ 1-40 (and only 2-fold higher insoluble A $\beta$ 1-42) were found present in brains of AD patients as compared to CU-AP<sup>146</sup>. On the other hand, the soluble A $\beta$ 1-40 and A $\beta$ 1-42, as a fraction of total A $\beta$ , were higher in CU-AP<sup>146</sup>. Given that A $\beta$  plaques are considered to be mostly made up of insoluble fibrils, this suggests that A $\beta$  plaques, in particular the cored pathology in AD, comprise the majority of insoluble A $\beta$ 1-40 in AD brain.

### **1.3.3 The amyloid cascade hypothesis**

Since its discovery 1984, and later its cloning, A $\beta$  has played a central role in AD research<sup>72,147,148</sup>. The focus on A $\beta$  aggregation, and its interplay with downstream event as the driving force or trigger in AD was only first put forward in 1991 with the amyloid cascade hypothesis<sup>48,49,149-151</sup>. The originally postulated hypothesis placed deposition of A $\beta$  in parenchymal space as the trigger for AD. This was supported by the missense mutations in APP itself, or two presenilin genes (PSEN1 and PSEN2, encoding the active region of  $\gamma$ -secretase), both leading to either an increased A $\beta$  production or an increased propensity for aggregation<sup>152-155</sup>. The observation that trisomy 21 in Down’s syndrome, associated with an extra copy of APP, leads to early-onset dementia with A $\beta$  plaque pathology strengthened this view<sup>156</sup>. Interestingly, mentally disabled adults who do not have Down’s syndrome, and have no additional copy of APP have been shown to have just as many A $\beta$  plaques and NFT as individuals with Down’s syndrome<sup>157,158</sup>. Since its initial postulation, the amyloid hypothesis has been challenged and refined; it does still however place A $\beta$  and its dyshomeostasis at the centre of AD<sup>114,159,160</sup>.

In its current form, the amyloid cascade hypothesis proposes either failure in A $\beta$  clearance or an increase in A $\beta$  production as initial steps driving AD<sup>160</sup>. On the one hand any mechanism contributing to faulty A $\beta$  degradation, including genetic risk factors (e.g. APOE  $\epsilon$ 4), are the initial triggers in sporadic AD (sAD)<sup>161,162</sup>. On the other

hand, the earlier mentioned missense mutations lead to an increase in the relative A $\beta$  production throughout life in familial AD (fAD). Both of these characteristics eventually lead to the accumulation and oligomerization of A $\beta$  (particularly A $\beta$ 1-42) in the limbic system and association areas of the cerebral cortex. Besides gradual deposition into diffuse plaques, the A $\beta$  oligomers can affect synaptic activity, lead to activation of inflammatory responses (comprising both microglial and astrocytic involvement), induce oxidative stress, and alter neuronal ionic homeostasis. At the same time, A $\beta$  oligomers can also directly affect kinase and phosphatase activities, leading to tau hyperphosphorylation and formation of neurofibrillary tangles (NFT). Together these processes cause direct injury to synapses and, later, to neurons, inhibit long-term potentiation (LTP), lead to neuronal loss, neurodegeneration, and eventually end in dementia.

The amyloid cascade hypothesis has been challenged in multiple ways<sup>159,163,164</sup>. For instance, A $\beta$  pathology has been found in cognitively unaffected-amyloid positive (CU-AP) subjects<sup>54,165</sup>. Further, there is no correlation of A $\beta$  plaque pathology with cognitive symptoms<sup>64,66,67</sup>. Most importantly, the majority of clinical trials where anti-A $\beta$  therapies have been used have failed<sup>166,167</sup>. While clearly undercutting the initial version of the hypothesis, these can be explained in the light of the redefined postulates, in which general A $\beta$ , including soluble oligomers, lies in focus.

With regard to CU-AP subjects, these display predominantly diffuse, rather than cored plaque pathology, which dominates in sAD. Diffuse pathology in CU-AP does not appear to be associated with gliosis or neurodegeneration, and therefore might not be neurotoxic. In support of this, a limited presence of soluble oligomers in CU-AP patients as compared to sAD has been reported<sup>168</sup>. Further, also with regard to limited correlation between cognitive symptoms and A $\beta$  plaque pathology, soluble A $\beta$  oligomer species, rather than full-blown A $\beta$  plaques, have indeed been found to correlate with disease severity<sup>169</sup>.

Along the line of the revised amyloid hypothesis, A $\beta$  itself might not cause the cognitive impairment (and hence not correlate as well as, for instance, tau), but rather

causes initial cellular and molecular changes that in turn lead to observed dysfunctions. In support of this, a similar duration has been observed for both fAD and sAD (regardless of APOE  $\epsilon$ 4 carrier status), in spite of different age-at onset of the disease<sup>166</sup>.

Further, this causative, but not necessarily symptom-driving role of A $\beta$  might also explain the negative results in most anti-A $\beta$ -based clinical trials that often target patients with mild cognitive impairment (MCI) or mild to moderate AD. The trial failures may further highlight that A $\beta$  pathology occurs much earlier in life than we previously thought; most data suggests that it might appear already in mid-life. Early intervention would thus mean intervention at a preclinical disease stage, which highlights the need for biomarkers for screening.

The amyloid cascade hypothesis does not explain the heterogeneity in A $\beta$  aggregation states, or A $\beta$  pathology polymorphism (described below); neither does it address the physiological function of A $\beta$ , the mechanism of A $\beta$  pathology spread, or for that matter how long it takes for A $\beta$  to transition from a soluble to an insoluble state. Still, given the finding of APOE  $\epsilon$ 4-impaired A $\beta$  clearance being a risk factor for AD, as well as low CSF A $\beta$ 42 levels and amyloid-PET positivity preceding other clinical and molecular manifestations in AD (e.g. tau), the amyloid cascade hypothesis continues to provide a framework for AD research.

### **1.3.4 Genetics and AD models**

A small portion of AD cases are caused by autosomal dominant mutations (less than 5%)<sup>170</sup>. These are referred to as familial AD (fAD). Patients with fAD have the disease onset generally before 65 years of age (depending on the mutation). The rare fAD mutations are caused by mutations in genes encoding amyloid precursor protein (APP) located on the chromosome 21 (Figure 3), as well as two  $\gamma$ -secretase components, presenilin 1 and 2 (PSEN 1 and PSEN2) located on chromosomes 14 respective 1. There is a wide variety of different mutations that have been identified for each of the genes (see Alzforum for updated list, (<https://www.alzforum.org/mutations>)).

Overall, the fAD mutations lead to either an increase in A $\beta$  production if they are N-terminal of A $\beta$  (e.g. Swedish mutation, KM670/671NL)<sup>171-174</sup>; an increase in the propensity of A $\beta$  to aggregate, if within A $\beta$  sequence mutations (e.g. Arctic mutation, E693G)<sup>174-176</sup>; or an increase in the relative amount of A $\beta$ 1-42 production as compared to less aggregation prone A $\beta$  peptides, such as A $\beta$ 1-40, if modifying the C-terminal processing (e.g. London mutation V717I in APP, or presenilin mutations)<sup>152,174,177-182</sup>.

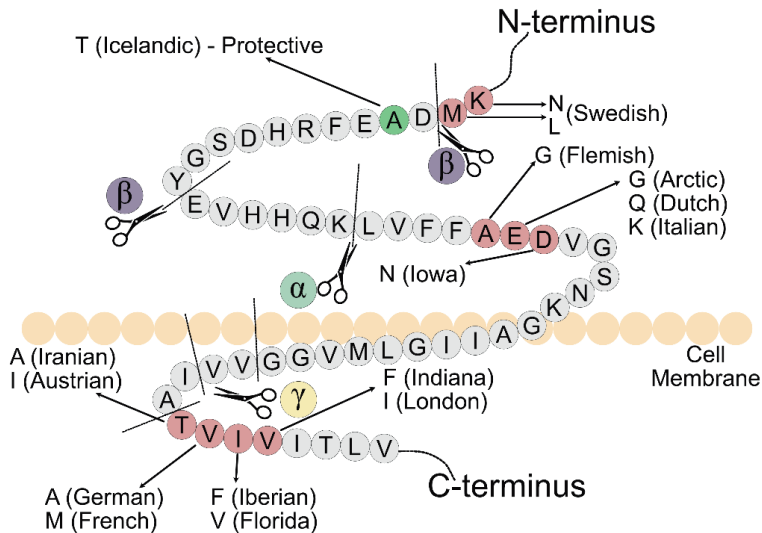


*Figure 3. Schematic overview of the APP sequence highlighting some of the well-known mutations. The cleavage sites ( $\alpha/\beta/\gamma$ ) are marked with straight black lines. APP mutations which increase the amyloidogenic processing are marked in red, these are present before, within, and after the A $\beta$  peptide sequence. A recently discovered protected mutation is highlighted in green.*

The etiology of idiopathic AD remains unknown. However, the pathological and clinical symptoms of familial AD (fAD) and sporadic AD (sAD) are similar. Therefore, despite the initial trigger, the assumption that downstream events of AD are alike between fAD and sAD allows for the use of genetic mutations associated with fAD in AD animal modelling (particularly in mice). While these models do not fully reproduce the spectrum of AD symptoms, they are still useful for examining critical aspects and pathology associated with this disease. Importantly, these models develop extracellular A $\beta$  plaques, and in specific cases also neurofibrillary tangles (NFTs), in an age-dependent manner.

#### 1.3.4.1 Mice models

AD modelling in mice is typically done by overproducing mutant APP<sup>183-185</sup>. Here, the amino acid sequence of A $\beta$  itself is most often humanized through substitution of three amino acid substitutions at positions 5, 10 and 13 (respectively G5R, F10Y and R13H)<sup>184,186</sup>. Besides the overexpression of APP, the A $\beta$  associated symptoms of AD are modelled using presenilin 1 mutations (PSEN1)<sup>183-185</sup>.

Multiple mutations in APP and PSEN1 are often used at the same time. This is in order to facilitate either an increase in total A $\beta$ , increase in aggregation propensity, increase in A $\beta$ 42/40 ratio, or a combination of these options. These models have been used, for instance, to demonstrate that elevated levels of the longer, more aggregation prone A $\beta$ 1-42, lead to earlier and more severe cognitive decline, and more exacerbated A $\beta$  plaque pathology. On the other hand, the shorter, less aggregation prone A $\beta$ 1-40, without a prior A $\beta$ 1-42, does not lead to A $\beta$  plaque formation<sup>56</sup>. The Swedish mutation is most often used for AD modelling, either alone or in combination with other mutations<sup>183-185</sup>.

Technically, mutations in microtubule associated protein tau (MAPT) gene are not linked to fAD, and instead cause other tauopathies (without A $\beta$  plaques), including frontotemporal dementia (FTD)<sup>187</sup>. However, hyperphosphorylation of tau and formation of NFTs is central to AD<sup>46,188-191</sup>. Pathogenic mutations in MAPT can lead to an increase in the production of tau isoforms, changes in the microtubule assembly, or make tau more prone to aggregate. Given the fact that APP-overexpressing mice do not develop NFTs, even though increased hyperphosphorylation has been shown, introduction of MAPT mutation (or removal of nitric oxide synthase 2) has been used to induce NFT development in mice<sup>183,192-194</sup>. These mice models have been used to demonstrate that A $\beta$  plaque pathology precedes the NFT development<sup>195,196</sup>. This, for instance, through interference of A $\beta$  oligomers in the ubiquitin protease-based degradation of tau.

In addition to transgenic models overexpressing A $\beta$  and tau, knockout (KO) mice lacking AD related genes have also been developed<sup>197,198</sup>. These mice have no

pathological features. Still they have provided useful insight into the molecular mechanism underlying AD and the role of the implicated proteins. Here, APP and tau KO mice have together been used to demonstrate the necessity of tau, particularly soluble tau, for the mediation of APP and A $\beta$  associated negative effects on cognitive deficits and long-term potentiation (LTP)<sup>199,200</sup>. Interestingly, while tau KO mice have been shown to exhibit axonal and neuronal defects, app KO mice did not reveal abnormalities, including no neuroanatomical changes, at least at a young age<sup>197-199</sup>.

Besides APP and tau KO mice, mice lacking APP secretases, including BACE, Presenilin 1 and 2, and ADAM 10 and 17 have also been developed<sup>201-204</sup>. Here, Presenilin 1 KO mice were used to demonstrate the crucial role of Presenilin 1 and  $\gamma$ -secretase, in neuronal and skeletal development, with homozygote KO being lethal<sup>201</sup>. In contrast, while BACE1 KO mice have implicated this protein in myelination or regulating the expression of voltage-gated ion channels, these mice were shown to be generally healthy<sup>203</sup>. Importantly, they do not produce any A $\beta$ . Therefore, BACE1, rather than Presenilin 1 or  $\gamma$ -secretase complex, appears to be a safer target for drug intervention.

There are many translational concerns regarding the use of animal models and their suitability to model human AD<sup>183,205,206</sup>. Broadly these are associated with the lack of concordance with clinical trials, the heterogeneity of patients enrolled in clinical trials and homogenous nature of these models, and insufficient cellular and synaptic loss compared to human subjects. More specifically, the overexpression of the APP in transgenic mouse models pose additional concerns.

The artificial promoters do affect the gene expression, not only the levels but also the site, or cell type of expression. Further, the expression of the gene varies between lines, as well as between different time points. Besides the actual gene expression, the overexpression itself results in unphysiologically high levels of both APP, but also its proteolytic fragments. This may have numerous undesired side effects, and exacerbates the degree and time-line of pathological feature development<sup>183,205,206</sup>.



In order to address some of these challenges, a novel approach based on knock-in (KI) strategy has been developed<sup>207,208</sup>. In terms of APP KI mouse models, this allowed for the identification of APP expression regulatory function of intron 16 spanned by the A $\beta$  sequence<sup>208</sup>. Therefore, the new generation AD KI mouse models exhibit physiological levels of A $\beta$ . Still, in order to model the pathology, these mice have fAD mutations. Two of these more established models, exhibit Swedish and Iberian (APP<sup>NL-F</sup>); or Swedish, Arctic and Iberian mutations (APP<sup>NL-G-F</sup>)<sup>207,208</sup>. These models develop significant A $\beta$  pathology and neurodegeneration, have an accumulation of both astrocytes and microglia, and eventually also develop memory impairment. Depending on the expression of the Arctic mutation (APP<sup>NL-G-F</sup>) the pathology can be present as early as 2-months (or 6-months in APP<sup>NL-F</sup>), and memory impairment already at 6-months (respective 18-months in APP<sup>NL-F</sup>).

### 1.3.5 Other risk factors

Besides fAD-causing mutations, several gene polymorphisms have been implicated in an increased risk of sporadic AD (sAD) or also referred to as late-onset AD (LOAD), which accounts for 95% of all AD cases<sup>209</sup>. These are referred to as “risk” or “susceptibility” genes and are identified by genetic association studies. AD genes are involved in a wide variety of cellular processes including, for example, lipid metabolism and transport, or immune function (e.g. apolipoprotein E [APOE] and triggering receptor expressed on myeloid cells 2 [TREM2])<sup>170</sup>.

The apolipoprotein E encoding gene APOE is the most important susceptibility gene unequivocally associated with AD<sup>162</sup>. The gene is located on chromosome 19, and exhibits three common forms of polymorphism including allele  $\epsilon$ 2,  $\epsilon$ 3 and  $\epsilon$ 4<sup>210,211</sup>. The three ApoE protein isoforms generated by these alleles differ only in single amino acids, either the cysteine (Cys) or the arginine (Arg), located on the on positions 112 or 158 ( $\epsilon$ 2: (C112, Cys158);  $\epsilon$ 3: (Cys112, Arg158);  $\epsilon$ 4: (Arg112, Arg158)). Here, the  $\epsilon$ 3 allele is the most common one. Further, while the  $\epsilon$ 2 allele has been suggested to have a protective role, the  $\epsilon$ 4 is associated with increased risk of AD<sup>161,211-214</sup>. This risk of AD has been shown to increase 2- to 4-fold in heterozygote carriers, and 8- to 12-

fold in homozygotes<sup>214,215</sup>. Besides the increase in AD risk, the  $\epsilon 4$  allele appears to lower the age of onset of AD in a “dose-dependent” manner<sup>162,188</sup>.

In the central nervous system, apoE is produced primarily by astrocytes. It regulates lipid homeostasis by mediating lipid transport, in particular that of cholesterol, to neurons via the low-density lipoprotein receptors (LDLR) for apoE<sup>162,216</sup>. Besides affecting the risk of AD, peripheral apoE isoforms have also been implicated in atherosclerosis, stroke and coronary heart disease, by causing lipidemia and hypercholesterolemia<sup>210</sup>.

Different APOE alleles influence the way this protein interacts with lipids, receptors and the A $\beta$  itself<sup>162</sup>. This affects the metabolism, aggregation, and deposition of A $\beta$ , both in terms of extracellular A $\beta$  plaques, as well as vascular amyloid (the cerebral amyloid angiopathy, CAA)<sup>217-219</sup>. Specifically, the A $\beta$  plaque load has been shown to increase in an isoform-dependent manner ( $\epsilon 4 > \epsilon 3 > \epsilon 2$ ), both in mice and human<sup>220</sup>. In line with this,  $\epsilon 4$  carriers have lower A $\beta$ 42 concentrations in the CSF, and higher amyloid PET (PiB) signal in the brain<sup>42,221</sup>.

The isoform effect is believed to stem from the differences in the lipidation status between isoforms, which in turn affects the efficiency with which apoE mediates A $\beta$  clearance<sup>162</sup>. Here, differences in both binding efficiency of the apoE isoforms towards A $\beta$  and the cellular uptake and degradation of the apoE-A $\beta$  complexes, have been demonstrated<sup>222,223</sup>. In particular, the E4 isoform has been shown to have a lower binding affinity towards A $\beta$  than the E3. Interestingly, complete APOE gene knockout essentially eliminates A $\beta$  plaque deposition in transgenic AD mice<sup>224</sup>.

The triggering receptor expressed on myeloid cells 2 (TREM2) gene is located on chromosome 6 and was recently identified as a risk factor for AD<sup>225,226</sup>. Here, two rare arginine to histidine point mutations on positions 47 and 62 (R47H and R62H) have been implicated<sup>227,228</sup>. Both of these mutations lead to loss of function of ligand-binding. Other mutations in this gene have also been discovered; however, these are not considered risk factors for AD<sup>229,230</sup>. Instead, they have been implicated in

microglia dysfunction in the context of other diseases, e.g. FTD, by affecting the trem2 stability or expression.

Trem2 is a cell membrane protein present on microglia and myeloid cells<sup>225</sup>. It is involved in innate immune response and cell proliferation<sup>231</sup>. Activation of trem2 can be done by a large range of ligands, both lipids and proteins, including phospholipids, HLD and LDL, as well as apoE and A $\beta$ <sup>232-236</sup>.

TREM2 deficiency impairs microglia migration towards apoptotic neurons<sup>237</sup>. TREM2 knock-out in primary microglia decreases general immune response in aging, but also in AD<sup>238-240</sup>. Intramembrane proteolysis of trem2 by ADAM metalloproteases (ADAM10/ADAM17) has been shown to generate a soluble extracellular fragment (sTREM2)<sup>241</sup>. This fragment is elevated in the CSF of early symptomatic stage AD patients<sup>242</sup>. Furthermore, the two mutations involved in AD have been suggested to result in impairment of microglia recruitment towards the A $\beta$  in plaque pathology. This results in less efficient encapsulation of the A $\beta$  plaques, and thereby decreased efficacy with which microglia restrict plaque growth<sup>239,240,243</sup>.

In addition to fAD mutations and risk genes, several risk factors have been implicated in AD<sup>209</sup>. The strongest risk factors are aging and gender<sup>244,245</sup>. Women are more prone to develop AD. Other diseases, including heart disease, diabetes, and stroke, as well as high blood pressure and high cholesterol, have also been demonstrated to be risk factors for AD<sup>209,246-248</sup>. Epidemiological association studies have further suggested head trauma, low education level, as well as low social and/or physical activity to increase AD risk<sup>209,249,250</sup>. However, these studies are not always replicable.

### **1.3.6 Role of lipids in AD plaque pathology**

Over 100 years ago, Alois Alzheimer described a third hallmark of AD, the adipose inclusions<sup>251</sup>. While this suggested an abnormal lipid metabolism to be associated with the AD pathological progression, the subject of lipids in context of AD has until now gained only limited attention of the AD field<sup>252</sup>. The discovery that the APOE allele  $\epsilon$ 4, a major lipid transporter, directly interacts with A $\beta$  itself (described earlier) and is a major risk factor of sAD has however shifted more focus on the matter<sup>162</sup>. Recently

other genes associated in some way with functional lipids mechanisms have been elucidated, including TREM2, and also ATP-binding cassette, subfamily A, member 7 (ABCA7) and phosphatidylinositol 3,4,5-trisphosphate 5-phosphatase 1 (SHIP1)<sup>170</sup>.

Alongside the genetic components, epidemiological studies have shown cholesterol in particular and its derivatives play a major role in AD pathogenesis<sup>252-254</sup>. Further, lipidomic studies of brain extracts have now also implicated the majority of other lipid classes to be associated with AD<sup>253,255</sup>. For instance, lipids have been shown to underlie the regulation of A $\beta$  trafficking as well as proteolytic activity of membrane bound proteins, including APP itself, but also,  $\beta$ - and  $\gamma$ -secretase activities, associated with production of the A $\beta$  peptide (described earlier).

Cholesterol, or rather the balance between cholesterol and the acyl-coenzymeA:cholesterol acyltransferase (ACAT) converted cholesteryl-esters (and possibly also 24(S)-hydroxy cholesterol) has been suggested as a key component controlling amyloidogenesis<sup>256,257</sup>. Here, elevated levels of cholesteryl-ester, have been implicated as a driver of the A $\beta$  peptide release from the cells however, the exact mechanism remains unknown. Further, cholesterol efflux itself can affect this process either by accumulating intracellularly, or indirectly through APOE's lipidation process, which is mediated by the ATP-binding cassette transporter A1 (ABCA1)<sup>258,259</sup>.

In addition to cholesterol's metabolism and its transport being implicated in AD, cholesterol has also been shown to play a crucial role in lipid rafts and modulation of the activity of A $\beta$  generating enzymes and APP localization<sup>260</sup>. In particular, high cholesterol content directly regulates  $\beta$ - (BACE1) and  $\gamma$ -secretase (particularly Presenilin) activities by affecting the association of these enzymes (enzyme complex) with the lipid rafts (and also association of APP with lipid rafts) thereby promoting processing along the amyloidogenic pathway, which results in elevated A $\beta$  production<sup>261-263</sup>.

Alongside cholesterol, sphingolipids (including ceramides, sphingomyelin and glycosphingolipids) have also been implicated in AD by modulating the  $\beta$ - (BACE1)

and  $\gamma$ -secretase activity<sup>253,264</sup>. Here ceramides, which are central to the sphingolipid metabolism, have been shown to be elevated in the earliest clinical stages of AD, likely by mediating the oxidative cell death<sup>265</sup>. These species have also been demonstrated to enhance the stability of the BACE1, thereby affecting A $\beta$  generation<sup>266</sup>. Further, enhanced activity of sphingomyelin phosphodiesterase (SMase), responsible for conversion of sphingomyelin to phosphocholine and ceramide, has been shown in cells with PSEN1 mutation, suggesting the key role balance between sphingomyelin and ceramides plays in AD<sup>267,268</sup>. Indeed, inhibition of SMase and hence sphingomyelin accumulation, results in impairment of  $\gamma$ -secretase activity, and leads to reduction of A $\beta$ <sup>267</sup>.

Gangliosides, membrane glycosphingolipids, found in cholesterol-rich lipid raft-like microdomains, have also been implicated in AD<sup>253,269,270</sup>. The monosialogangliosides (GM, a-series) in particular, species containing single sialic acids, have been suggested to play a critical role in A $\beta$  aggregation<sup>270,271</sup>. In general, the tissue levels of shorter GM2 and GM3 species have been demonstrated to be increased in multiple brain regions of AD patients<sup>272</sup>. Interestingly, it is the longest, GM1, that has been suggested to act as an aggregation seed by binding A $\beta$  and altering its conformation to an ordered  $\beta$ -sheet structure<sup>273-276</sup>.

Indeed, the presence of GM1-A $\beta$  complexes has been shown to be associated with the early changes in AD<sup>277</sup>. However, injection of the GM1 has been shown to decrease the A $\beta$  burden, likely by promoting A $\beta$  degradation<sup>278</sup>. Along this line, ablation of the GM2 synthase, resulting in loss of GM1 and accumulation of GM3 has been shown to result in deposition of A $\beta$ <sup>279,280</sup>. Further, ablation of the ganglioside GD3 synthase (GD3S) responsible for shift towards b- and c-series gangliosides, increases a-series gangliosides and has been shown to be protective against A $\beta$  induced neurotoxicity<sup>281</sup>. Therefore, while clearly implicated in the A $\beta$  pathogenesis, the exact role of different gangliosides in AD remains unknown.

Finally, besides cholesterol (and its derivatives) and sphingolipids, a third large class of lipids, phospholipids, has also been implicated in AD<sup>252-254</sup>. Here changes in

phosphoinositides (phosphorylated phosphatidylinositols (PIs)), and phosphatidic acid (PA) in particular, have been demonstrated to affect the A $\beta$  generation, including the APP trafficking and presenilin modulation. Further, alteration of phosphoinositide kinases and phosphoinositide phosphatases, as well as phospholipases, including A2, C and D (PLA2, PLC and PLD), enzymes responsible for phospholipid metabolism have also been demonstrated in AD.

The phosphatidylinositol 3-kinase (PI3K) pathway has been shown to play a crucial role in A $\beta$  production<sup>263</sup>. Its inhibition results in reduced A $\beta$  levels<sup>282,283</sup>. Here, the phosphatidylinositol-4,5-bisphosphate [PI(4,5)P<sub>2</sub>] in particular modulate the  $\gamma$ -secretase activity by exhibiting competitive binding to this enzyme<sup>262,263</sup>. Indeed, there is an inverse correlation between PI(4,5)P<sub>2</sub> and A $\beta$ 42 levels in cultured fibroblasts cells<sup>284</sup>. In terms of AD, PSEN1 mutations have been shown to be associated with an increased turnover of PI(4,5)P<sub>2</sub> through the PLC pathway<sup>284,285</sup>. Reduction of this turnover decreases A $\beta$ 42 production.

The PLD pathway responsible for hydrolysis of phosphatidylcholine to phosphatidic acid (PA) and free choline, has been implicated in AD due to its role in modulating the APP processing<sup>286</sup>. In particular, studies have demonstrated that the overexpression of PLD1 compensates for the impairment in APP trafficking to cell membrane in fAD PSEN1 mutant neurons<sup>287</sup>. Further, the PLD1 has been shown to negatively regulate processing of the APP by the  $\gamma$ -secretase, likely by modulating the PSEN1 activity<sup>288</sup>.

Finally, previous studies have revealed that the PLA2 pathway regulates neuroinflammation and neurodegeneration in AD<sup>289</sup>. It has been demonstrated to exhibit elevated activity in vicinity of A $\beta$  plaques<sup>291</sup>. The enzymatic activity of this enzyme results in release of the lysophospholipids and polyunsaturated fatty acids (PUFAs) such as arachidonic acid (AA)<sup>290,291</sup>. Indeed, reduced levels of phospholipid bound AA, as well as increased levels of AA and metabolites have been observed in AD brain<sup>292</sup>.

Further, involvement of PUFAs and their metabolites in AD, in particular the  $\omega$ -6 (e.g. linoleic acid (LA) and arachidonic acid (AA)) as well as  $\omega$ -3 (docosahexaenoic acid (DHA)) acids, have also been shown in relation to the oxidative stress induced lipid

peroxidation<sup>293-295</sup>. Here, this process has been suggested to be either direct oxidation of PUFAs by the reactive oxygen species (ROS), or by peroxide mediated oxidation which itself can be generated through A $\beta$  induced reduction of metal ions (such as copper (Cu<sup>2+</sup>) or zinc (Zn<sup>2+</sup>)), or from the PUFAs themselves acting as an electron donor to the A $\beta$ -metal ion complex<sup>296,297</sup>. The oxidized PUFAs degrade to toxic metabolites.

### **1.3.7 A $\beta$ maturation and conformational polymorphism**

Presence of A $\beta$  plaque pathology is considered the major hallmark of AD<sup>45</sup>. In sporadic AD, A $\beta$  plaque pathology manifests itself in cored, “congophilic”, neurotoxic deposits, and diffuse plaques<sup>50</sup>. As mentioned earlier, diffuse plaques have also been found in CU-AP patients (previously known as pathological aging)<sup>54</sup>.

Based on these observations of plaques in CU-AP it has been put forward that at least in sAD and CU-AP, diffuse plaques might represent an early, immature state of the A $\beta$  plaque pathology that eventually, would progress to the “mature” dense cored A $\beta$  plaques<sup>51,54,298</sup>. Studies in transgenic animals have suggested that the two types of deposits might however be formed through different and independent pathways, and might instead represent a neuroprotective mechanism<sup>299</sup>.

Along this typical morphological classification of extracellular amyloid plaques, into diffuse and cored/dense/mature deposits, a new focus has emerged, the amyloid polymorphism<sup>300,301</sup>. Here, recent studies of higher order amyloid assemblies implicated in neurodegenerative diseases, particularly A $\beta$ , have demonstrated a high degree of conformational variation among oligomers, protofibrils, fibrils and even plaques<sup>301-303</sup>. In the context of AD, this polymorphism has been shown to originate from the differences in folding of individual peptides and protomers (oligomers), and respectively the assembly of individual protofibrils into fibrils and plaques (introduced earlier)<sup>304</sup>.

Recent cryo-EM and solid-state NMR studies have visualized folding polymorphism not only in-between different peptide aggregates, e.g. A $\beta$ 1-40 respective A $\beta$ 1-42, but also that the same peptide, such as A $\beta$ 1-42, can fold differently resulting in multiple

structural models of A $\beta$  fibrils<sup>305,306</sup>. In addition to synthetic in-vitro studies, extracts of the clinical subtypes of Alzheimer's disease have also demonstrated a high degree of conformational polymorphism<sup>307</sup>. This poses tremendous challenges to development of any therapeutics targeting higher order aggregates (e.g. oligomers), as these then face issues “fitting” the shape of the amyloid<sup>301</sup>. Further, it poses problems related to the detection and visualization of amyloid structures for diagnostic purposes<sup>302</sup>.

In clinical diagnosis, Congo Red (CR) is typically used for detection of amyloid assemblies. However, a wide variety of other amyloid probes have also been developed for more sensitive detection of a small amount of the amyloid structures. In the context of AD, CR staining is complemented with more specific peptide directed antibody staining (most often toward A $\beta$ 1-40 or A $\beta$ 1-42), in order to identify less A $\beta$  aggregated structures not detected with CR, for instance diffuse plaques. Such antibody-based staining is also the golden standard for the visualization of different A $\beta$  truncation present in plaques. Together, these approaches offer the possibility to, according with current practices, classify detected amyloid into diffuse and compact/mature/cored structures. Nevertheless, these cannot distinguish between different degrees of aggregation, such as oligomers, protofibrils, and fibrils. Nor can they distinguish between the structural and conformational polymorphism of same order structures as introduced above.

An approach to overcome this has been the development of conformation specific antibodies that target the aggregated, rather than monomeric structures (e.g. oligomers or protofibrils)<sup>308,309</sup>. While potentially offering the possibility to classify aggregation states in pharmaceutical contexts, the conformational antibodies suffer multiple limitations. These include the general limitations of antibody-based approaches (e.g. affinity, issues caused by post translational modifications, tissue penetration, and multiplexing), but also include the challenges associated with their targets' conformational flexibility.



An alternative method for sensitive and conformation specific detection of polymorphic amyloid structures, is the use of electro-optically active chromophores<sup>310</sup>. Depending on the binding site of their target, these can rotate, thereby changing the effective  $\pi$ -electron conjugation length within their backbone structure. This in turn yields different fluorescence emission. Here, luminescent conjugated oligothiophene probes (LCO), with such flexible backbones, have been used to demonstrate age-dependent changes in conformational polymorphism within individual plaques, conformation specific properties of prions, and, most recently, variability in A $\beta$ -amyloid aggregate structures between plaques of AD subtypes (e.g. fAD, sAD)<sup>303,311-313</sup>. Still, while these probes can to some extent be multiplexed with peptide specific antibodies (and spectrally delineated, described in Method), the degree of multiplexing is limited, making it hard to determine the proteomers and peptides underlying the amyloid heterogeneity. Therefore, alternative approaches are needed in order to investigate the broad diversity of A $\beta$  truncated peptides, as well as other biomolecules, in the context of AD.

Mass spectrometry (MS) offers the possibility of directly identifying tens, and even hundreds of different molecular species at the same time (based on their m/z value). Further, in contrast to antibodies that might suffer specificity issues, the molecular identification in MS is based on the precise mass of the actual molecule (rather than indirect detection as with antibodies), which can often be confirmed by the fragmentation of the molecule. Indeed, MS has been used in the context of AD, to identify a wide diversity of A $\beta$  peptides present in human CSF<sup>314-316</sup>. Therefore, MS should be considered a powerful tool for future investigation of molecular complexing in AD.

Taken as a whole, the A $\beta$  pathogenicity is highly complex with morphologically heterogeneous plaques, the structural polymorphism of A $\beta$  fibrils, and complex molecular changes. Given the lack of understanding, an integration of recent developments needs to be explored. In particular it is crucial to readdress the well acknowledged, yet poorly understood, key pathological feature of AD, the A $\beta$  plaques.

## 2 AIMS

### 2.1 General aims

The overall aim of this thesis was to gain a deeper understanding of WHERE, WHEN, and HOW A $\beta$  aggregates and precipitates into extracellular A $\beta$  plaques, and what other biochemical factors, besides A $\beta$  itself, promote A $\beta$  aggregation in AD pathogenesis.

Further, the aim was to examine biochemical factors that might underlie amyloid plaque polymorphism. In particular, the intent was to elucidate potential factors responsible for the formation of A $\beta$  plaque morphotypes associated with neurotoxicity in Alzheimer's disease (AD) patients, which are not observed in cognitively normal amyloid positive (CU-AP) individuals.

### 2.2 Specific aims

#### Paper I

Matrix-assisted laser desorption/ionization (MALDI) imaging mass spectrometry (IMS) has been proven suitable for analysis of protein and peptides directly on tissue sections. The aim of this work was therefore to investigate suitability of MALDI-IMS to study protein and peptides content within individual A $\beta$  deposits, across different brain regions in tgAPP<sub>ArcSwe</sub> mice.

#### Paper II

Lipids have been suggested to be involved in AD pathology. Therefore the aim of this work was to investigate whether different, complementary IMS techniques can be used to probe the lipid-peptide interplay associated with plaque pathology in tgAPP<sub>ArcSwe</sub> mice.

#### Paper III

Laser irradiation in MALDI IMS could be destructive to tissue morphology. The aim of this work was therefore to study the impact of MALDI IMS on tissue surface, and establish whether MALDI IMS can be interfaced with immunohistochemical (IHC)

analysis and fluorescent microscopy for multimodal, comprehensive chemical imaging.

#### Paper IV

Structural polymorphism within individual amyloid plaques has been reported to be associated with heterogenous AD pathogenesis. Amyloid polymorphism can be probed using luminescent conjugated oligothiophenes (LCOs). This work did therefore seek to combine MALDI IMS with LCO based structural amyloid imaging to identify neuronal lipid patterns associated with intraplaque heterogeneity in-between diffuse and cored plaques structures in tgAPP<sub>Swe</sub> mice.

#### Paper V

Diffuse and cored A $\beta$  plaques are both present in AD pathology, while plaques in CU-AP are predominantly diffuse in morphology, suggesting plaque maturation into cored plaques to be critical in AD pathogenesis. Various A $\beta$  truncations have been suggested to be responsible for the formation of polymorphic plaques. The goal of this work was therefore to identify potential aggregation-promoting A $\beta$  species associated with plaque polymorphism (diffuse and cored plaques) in sAD, CU-AP, as well as tgAPP<sub>Swe</sub> mice.

#### Paper VI

A $\beta$  aggregation is believed to be a continuous process, where A $\beta$  plaque pathology has been shown to progressively spread across brain regions. The aim of this work was therefore to follow the evolution of plaque pathology in terms of A $\beta$  processing and deposition, across main pathologically relevant anatomical regions in tgAPP<sub>Swe</sub> mouse brain over different ages.

#### Paper VII

The chain of events underlying A $\beta$  aggregation, plaque formation and plaque growth is not well understood. This work therefore sought to establish a novel *in vivo* stable isotope labeling method for spatiotemporal A $\beta$  imaging, to study A $\beta$  plaque deposition, from its earliest onset until full development in knock-in mice model of AD.

## 3 METHODS

### 3.1 Ethics statements

Experiments on human post mortem brain tissue were approved by the ethical committee in Gothenburg (DNr 012-t5; 150416). The ethical committee at Uppsala University has approved all the animal experiments on transgenic mice (#C233/8; #C216/11; #C49/10; #C17/14 (Uppsala)) needed to carry out the work in papers I-VI. The ethical committee at the University College London (UCL), London, United Kingdom, has approved all the experiments based on knock-in mice model needed for method development in paper VII (160506). All animal experiments were performed in accordance with the principles of the Declaration of Helsinki.

### 3.2 Optical light microscopy

An optical microscope, commonly referred to as a light microscope, relies on the use of light, in combination with a lens (or lenses), to generate magnified images of the analysed object. While the early microscopes consisted of a single lens, the majority of modern microscopes consist of multiple lenses. This includes an objective lens that focuses the image of the analysed sample inside the microscope, and ocular lenses, also referred to as an eyepiece, that magnify the image.

In general, there are two basic, common sample illumination principles in light microscopy. Either the entire sample is permanently illuminated, referred to as wide-field microscopy, or a single focal spot is illuminated, which is known as confocal microscopy (described in more detail below).

Wide-field microscopes, are commonly used with transmitted white light. Here contrast can be obtained in several ways with the sample either by: absorbing the light (bright-field contrast), scattering it (dark-field contrast), or refracting it, which will result in a phase shift of the transmitted light (phase contrast). Illumination can be from above or below (inverted, respective upright configuration)<sup>317</sup>.

Both confocal and wide-field illumination can also be used for fluorescence imaging (described in detail below). Here, rather than white light, only light of specific frequencies is used to excite fluorescent molecules present in the sample. This can provide specific information about their localization.

The resolution ( $\delta$ ) of light microscopes is the minimum distance between two points that can be viewed as separated. The limit of this distance, referred to as diffraction limit, is imposed by the diffraction of light as it passes through a circular aperture. This results in the production of diffuse circular discs by the passing light. These are known as Airy's discs. In practice, this implies that image formed in light microscopes is generated from the diffraction pattern produced by the circular apparatus at the back focal plane, after they been converged on the focal point<sup>317,318</sup>.

The resolution for optical microscopy can be described by the Rayleigh Criterion for lateral resolution (equation I)<sup>317,319</sup>. Here, the resolution is limited by the wavelength of illumination ( $\lambda$ ), and the numerical aperture (N.A.), which is a measure that reflects the objective lens' ability to collect light.

$$\delta = \frac{0.61\lambda}{N.A.} \quad (I)$$

In a simplified view, the numerical aperture is dependent on the refractive index of the medium ( $\mu$ ), and the angle subtended by the lens between the sample and objective ( $\alpha$ ) (equation II). Therefore, the equation for resolution (equation I) can be rearranged to account for these (equation III).

$$N.A. = \mu \sin \alpha \quad (II)$$

$$\delta = \frac{0.61\lambda}{\mu \sin \alpha} \quad (III)$$

From the equation III it is clear that the resolution is dependent on the wavelength of light with shorter wavelength of illumination light yielding higher resolution. Further, resolution can also be improved by increasing the refractive index of the medium. This refers to the relative ratio of the speed of light through a substance, as compared to

vacuum. With increasing  $\mu$ , the speed of light decreases, shortening the wavelength and thereby increasing resolution. This can be achieved through the use of immersion oils which have  $\mu$  around 1.5. Due to obvious reasons, higher resolution is needed for smaller objects, which require high magnification. In practice, the high magnification objectives (63x, 100x) also have higher N.A. and rely on the use of immersion oils. In theory, when simplified, the diffraction limit implies that an optical system has a maximal lateral resolution of approximately half the wavelength of light used for illumination.

The N.A. of a lens however also depends on the imperfection in the objective lens referred to as aberration<sup>320</sup>. These are either the spherical or chromatic aberrations. The spherical aberration is caused by the differences in the focusing of the light passing through the periphery versus the centre of the lens. This results in the image of an object not being in sharp focus. The chromatic aberration originating from the differences in refractive indices of light with different wavelengths, is termed dispersion (e.g. blue light refracted more than red). This results in light of different wavelengths being focused at different focal points.

The majority of modern microscopes address the problem of spherical aberrations in multiple ways<sup>317</sup>. One of these is simply limiting the light exposure of the lens only to its central part using diaphragms. The issues of chromatic aberration are also corrected with lens that are either achromatic, converging blue and red light, or even more advanced apochromatic, that bring blue, green and red light into a single focal point.

In light microscopy the limit in lateral resolution is roughly 200nm (fluorescence imaging, described in more detail below). This is theoretically the case for both the wide-field microscope but also the confocal microscope. In practice however the actual resolution of a wide-field microscope is affected by the background fluorescence and emission of out-of-focus light, which results in lower signal-to-noise ratio, and hence also contrast.

### 3.2.1 Confocal microscopy

Confocal microscopy refers to an optical imaging technique where a pinhole is used to block the light coming from outside of the focus plane<sup>317,321,322</sup>. This results in the illumination of a relatively small volume of the sample, instead of a whole specimen being exposed to the light from the light source in a conventional wide-field microscope. This allows for the control of depth of field in images, the reduction in background, and the possibility to obtain optical sections of specimen. Together, these advantages have made the confocal microscope a go-to technique for obtaining high-quality images in the field of cell biology.

A typical confocal microscope relies on seven main components. These are the laser, the beam splitter, laser scanner, objective lenses, motorized Z-axis control, a pinhole and photomultiplier tube (PMT)<sup>322</sup>.

The lasers (rather than an e.g. halogen lamp commonly used in wide-field microscopes) offer a very intense, bright, stable, narrow, non-divergent and easily focusable beam of light (point-like) that comes at a particular wavelength. This is necessary to ensure a homogenous illumination. Further, this offers the possibility to focus the laser to a diffraction-limited spot. At the same time however, as lasers exhibit specific wavelengths, several different laser sources might be needed to cover the wide range of excitation wavelengths of the common fluorophores in the visible spectral range (ca 350nm – 750nm). This is in contrast to the lamps typically employed in wide-field microscopes that provide excitation wavelengths across almost entire visible spectra.

A crucial component of a confocal microscope, particularly needed when performing fluorescent imaging is a beam splitter (also needed for wide-field fluorescence, described below)<sup>317,322</sup>. The beam splitter, which is typically the first component in the laser path, separates the excitation wavelength of light from the light that is emitted from the sample.

After passing through the beam splitter, the laser is directed to a set of scanning mirrors that tilt the laser beam in X-Y directions, and raster it pixel-by-pixel across the sample.

On its way to the sample surface the beam is passed through the objective lens, where it's focused in the back-focal plane of this lens, before being focused on the sample. The level of the optical section at which the laser light will be focused is achieved by adjusting the z-control. This can be done with high precision, and hence is employed for 3D analysis (referred to as Z-stacks). The reflected light emitted from the specimen is then collected back through the objective lens, and passes as a stationary (not scanning) light further along the scanning mirrors onto the detection system. Here the light is first passed through a pinhole aperture.

The pinhole is of adjustable size, and is the main component that allows for the exclusion of out-of-focus light in a confocal image<sup>317,322</sup>. It defines the thickness of the optical slice, and hence it is also crucial for optical sectioning. In general, the choice of the pinhole size reflects a compromise between the efficiency of light collection and the optical sectioning. Typically, the size of the pinhole is set to 1 Airy unit (Airy disc). It's an automatically calculated value that is dependent on what objective is used, objective's N.A., and magnification (as described above). This value will correspond to the diameter calculated for inner most circle produced as a diffraction pattern produced by a point light source (the Airy disc).

After being directed onto the pinhole, only a small central portion of light is used to create a point-like image at the detector. Therefore, the detectors in a confocal microscope typically consist of photomultiplier tubes (PMT). In simplified terms, these are vacuum tubes with electron multiplying components inside. These are necessary as the light that reaches past the pinhole might have very low intensity (some of the photons that indeed originate from the focal plane, might also have been blocked as if out-of-focus). The PMTs are used to amplify the signal, even up to 1,000,000 times, without introducing additional noise. This is in contrast to wide-field microscopes where the image is captured by a camera, such as a Charge Coupled Devices (CCD), the Complementary Metal Oxide Semiconductors (CMOS) camera.



## **3.2.2 Fluorescence microscopy**

### **3.2.2.1 Optical molecular spectroscopy – fluorescence**

Optical spectroscopy deals with the way light interacts with atoms and molecules, such as e.g. absorption and emission (or scattering). Here, the visible light corresponds to only a small fraction of the electromagnetic spectrum. In general, spectroscopy, deals not only with visible light but also longer wavelength radiations, such as for instance microwaves or infrared light (IR), and shorter wavelength radiation, such as ultraviolet light (UV), or X-rays.

Absorption of light (photons of distinct energy) by a molecule, leads to the promotion of electrons to an energetically higher state, referred to as the excitation state. The photoexcited molecules can then undergo several different steps in order to return to its ground state. These are commonly described in a Jablonski diagram, and include e.g. radiation-less vibrational relaxation or internal conversion, or photoluminescence. Photoluminescence refers to the processes where the return of an electron from its excited state is accompanied by emission of light. Two common types of photoluminescence include fluorescence and phosphorescence.

Fluorescence, is a type of photoluminescence. It is a process where the return to the ground state takes place without the change in electron spin (in difference to phosphorescence, where the change in electron spin takes place). It is very short lasting (nanoseconds), and typically results in emission of light of lower energy, and longer wavelength, than the absorbed light (due to co-occurrence of other processes).

#### **3.2.2.2 Fluorophores and fluorescence microscopy**

A molecule that can undergo the process of fluorescence is commonly referred to as a fluorophore. Such molecules both absorb and emit light of a wide variety of specific wavelengths, and therefore exhibit excitation and emission spectra. The difference between the maximal excitation and emission wavelength of a molecule is referred to as Stokes shift. The spectral properties of fluorophores depend on their structure.

Fluorophores are typically organic, carbon-based aromatic molecules with  $\pi$ -conjugation (alternating single and multiple bonds). Such structure allows for delocalization of  $\pi$ -electrons along the conjugation backbone, and the emission of light in form of fluorescence. In general, the intensity of a fluorescent emission of a fluorophore, referred to as quantum efficiency or quantum yield, does depend both on the backbone of the molecule, and its side substitutions.

Knowledge of the excitation and emission spectra of fluorophores is critical when dealing with fluorophores, in particular in the context of fluorescent microscopy, where light filters limiting the wavelengths need to be chosen (described in more detail below). If dealing with multiple fluorophores whose spectra overlap, the signals might “bleed through”.

For analytical purposes, fluorophores are attached to biological molecules, or other targets of interest, in order to enable identification, quantification, and even real-time observation of their biological/chemical activity. Fluorescence is widely used in biotechnology and analytical applications due to its extraordinary sensitivity, high specificity, and simplicity. Fluorescence microscopy is one of the most common applications. Regardless of the technique when working with fluorescence one needs to keep in mind potential photo-bleaching of the fluorophore, its brightness, and contrast that it can generate.

Fluorescence imaging can be performed on both a wide-field and confocal microscope. In the case of a wide-field microscope, fluorescence imaging is referred to as Epi-fluorescence. For both types of instruments, the illumination and collection of fluorescent emission is performed through the objective lens.

For the light to efficiently excite the fluorophore of interest only light of specific wavelengths (usually excitation maxima peak) should reach the sample. For an Epi-fluorescent microscope, this is achieved by passing the white light coming from the light source via a set of filters, before letting it into the objective for magnification and focusing (nowadays these are often confined in a single filter cube). After reaching, and being reflected back from the sample, the light again passes first through the

objective, and then through the filter cube, before it is finally imaged either by a camera, or visualized directly in the eyepieces. In a modern microscope, there is typically more than one filter cube, allowing for the detection of signals from several fluorophores distinct spectral properties.

The filter cube consists of three main components: the exciter filter, a dichromatic beamsplitter, and a barrier filter. Dichromatic beamsplitters, and nowadays also majority of the exciter and barrier filters, rely on so called interference filters. Interference filters are made of glass that has a dielectric coating. This gives the filter highly specific refractive and reflective properties. These filters are designed to reflect certain spectral bands (wavelengths), and efficiently transmit others.

The exciter filters (excitation filter) are responsible for selection of the illumination wavelengths. Here, either short pass filters (SP), which efficiently block light of longer wavelengths than the wavelength of maximum transmission, or band pass (BP) filters, which cut-off light both at shorter and longer wavelengths, are commonly used. These are especially useful when a given fluorophore has only small Stokes' shift.

The dichromatic beamsplitters, more commonly known as dichroic mirrors, are specialized interference filters. Their role however is to selectively reflect the excitation wavelengths of light and direct them towards the sample, while letting the fluorescence emission wavelengths coming from the sample to pass. They are positioned in the light path, between the exciter filter and the barrier filter, and are mounted at a 45° angle in relation to these two filters.

The barrier filter (emission filter) selectively permits certain emission wavelengths to pass towards the eyepiece/camera (while also suppressing or blocking the excitation wavelength). Just like exciter filters, the barrier filters are often BP filters. Alternatively, they can also be long pass filters (LP), which selectively block or suppress shorter wavelengths.

In terms of fluorescent imaging, confocal microscopes offer several advantages. These originate from the use of lasers and the pinhole. Given that lasers generate light of

distinct wavelength, selection of an excitation band using a filter cube is not necessary. Instead, a laser of appropriate wavelength is chosen in order to excite the fluorophore of interest (this can sometimes be problematic).

Given that the lasers do yield a point-like illumination, and that confocal systems rely on the use of a pinhole, such microscopes can be used to illuminate selected regions and focal planes in the specimen. Therefore, a general decrease of photo-bleaching of the sample will be observed. Further, reduced background fluorescence and increase contrast thanks to optical sectioning will be obtained. Still, modern wide-field microscopes are able to perform post-acquisition deconvolution of the images (by reassigning the origin of fluorescent signal) and remove a large majority of blurring, generating improved sharpened images.

### **3.2.2.3 Hyperspectral fluorescent imaging**

Luminescence conjugated oligothiophenes (LCO) are a special type of fluorophores used for detection of amyloid aggregates<sup>311,323,324</sup>. They have been shown to display unique spectral shifts upon binding to amyloid structures, both in solution, cells, and tissue sections. Further, they are particularly useful, due to their ability to recognize both the different aggregation state of same amyloidogenic protein, but also in some cases are specific for different amyloid proteins (e.g. amyloid- $\beta$  respective tau)<sup>324-326</sup>.

In comparison to conventional amyloid ligands, which possess sterically rigid structures due to their conjugated polymer backbone, LCOs display high conformational freedom<sup>310,327</sup>. The polar and hydrophobic character of LCOs backbone enables the probes to intercalate in the binding pockets of the fibrils, in a fashion similar to that proposed for Congo Red<sup>324,328</sup>. Upon interaction with the cationic residues present in the groves of the fibrils, a change of net charge on the acetic acid side chains occurs. This leads to the restriction of conformational freedom

of the probes, more planar arrangement, a change of effective conjugation, and hence a shift in excitation/emission of the probe <sup>324</sup>.

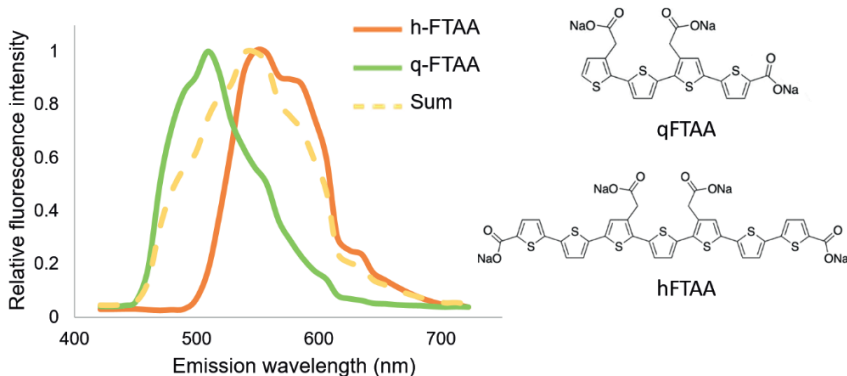


Figure 4. Schematic of normalized spectra of qFTAA (green) and hFTAA (red), and their mathematical sum (yellow), obtained from amyloid plaques in tissue. Chemical structures of the two fluorophores displays their four (quadro – qFTAA), respective seven (hepta – hFTAA) thiophene ring backbone. Adapted from Paper IV, Figure 1 <sup>329</sup>.

In general, the distance along the conjugation backbone along which the electrons can move, known as conjugation length, is the primary variable that gives the LCOs their distinct electrical and optical properties. The longer the conjugation, the longer the wavelength of light emitted by the LCO probe. Therefore, when in planar conjugation the emission is red-shifted, while in the twisted arrangement, the emission is blue-shifted.

Hyperspectral imaging represents a combination of light microscopy and spectroscopy. It relies on the use of a spectral detector for collection of spectrally separated emission light for each and every pixel in an image. This imaging technique has emerged to tackle the problem of overlapping fluorophores (which emission bands often span around 100nm) leading to signal bleed-through, and the limited possibilities of fluorophore multiplexing<sup>317</sup>.

Imaging based on spectral collection enables high-speed acquisition of multiple spectral profiles at the same time. If the emission spectra of individual fluorophores

have previously been acquired, these can be separated from a combined single spectral scan using software-based linear-unmixing algorithms (possible even when a high degree of spectral overlap exists between multiple fluorophores). This approach can further be employed to distinguish imaging artefacts from the real fluorophore signal in the sample (e.g. auto-fluorescence).

Even though most commonly performed using a confocal microscope, hyperspectral imaging can also be performed using a wide-field microscope. For this task, several different methodologies for spectral separation, and multiple detector designs, have been developed. Typically, spectral collection in hyperspectral imaging is performed by generating so called Spectral Image Lambda Stacks. These are three-dimensional datasets, where the same image field is acquired at different wavelengths that span over selected spectral regions. This is in comparison to a single or successive group of images as acquired in a conventional fluorescence imaging experiment.

In order for this to be possible, the emission light that emerges from the sample, is dispersed by either a diffraction grating or a prism. This light is then directed and focused at a multi-anode photomultiplier with the help of multiple mirrors. Such multi-anode photomultiplier most often consists of 32-channels. If operating in parallel with other detectors, such as PMT (typically present at the confocal microscopes), this can potentially offer more detection channels (often up to 34-channels). Depending on the spectral range in the hyperspectral imaging experiment, the spacing of the collection wavelength will differ (the range divided by number of detectors). This is referred to as wavelength resolution (spectral resolution). Depending on the instrument, this spacing can be brought down to a few nanometres.

### 3.3 Electron microscopy

Electron microscopy is a high resolution imaging technique, which relies on the use of accelerated beams of electrons rather than photons for sample illumination. The first electron microscope was built in 1932 by Knoll and Ruska<sup>330,331</sup>. Since then a wide variety of applications for the electron microscopes have been developed, allowing for

the study of structure-function relationship both in material sciences but also in biology and medicine<sup>332,333</sup>.

Electron microscopes utilize a beam of electrons as the sources of illumination. Here, several different beam source are used. These include heated tungsten filament, a more efficient thermal lanthanum hexaboride (LaB<sub>6</sub>), or tungsten field emission gun (FEG) that uses a powerful electric field to expel electrons from filament tip. The energy distribution of the electron sources as a fraction of the average energy varies, with the smallest being most optimal for high resolution imaging. Here, FEG electron guns are most coherent when it comes to electron energy distribution and are therefore used for high resolution imaging.

The generated electron beam is then accelerated towards the target surface guided by the positive electric potential. Along the way the beam is focused and confined with the help of lenses and apertures. Here, the electron lenses are composed of magnetic coils tuned to focus electrons of a particular wavelength, and bend away electrons of other wavelengths. The apertures on the other hand are metal holes that limit the diameter of the electron beam and are located after the lenses. Depending on their positioning they can for instance: adjust the coherence of the beam (condenser aperture), or the contrast of the image (objective aperture). Finally, “fine-tuning” of the electron beam’s asymmetric astigmatism, can be performed using weak electric and magnetic stigmators. Together, all these components are referred to as the column of the electron microscope.

Upon interaction of the incident electron beam with the matter in the sample, a wide variety of signals, (in the form of scattered or generated electrons, and radiation) can be detected. Broadly, these can be divided into signals that are either scattered back, and signals that are transmitted. In general, while signals that are scattered back are commonly analysed using a scanning electron microscope (SEM), the signals that are transmitted are analysed using a transmission electron microscope (TEM) (described in detail below). Together collection of these signals can provide unique information about the specimen and its properties in form of images.

Contrast in the electron microscopy images (commonly referred to as micrographs) arises from interference between the electrons. Here, the electron scattered from the sample, interfere with the primary electron beam coming from the electron source. Depending on the constructive or destructive interference of the electrons, darker and brighter regions in the image will be present. In general, electrons are more scattered by heavy elements, and only weakly scattered by light elements (such as Carbon or Nitrogen). Therefore, methods for enhanced contrast, such as staining with heavy elements, are often used when needed, especially in biology (described in detail below).

The column of the electron microscope, and in the majority of the set-ups the entire system including the sample chamber, are operated in a high vacuum. An exception to this is e.g. environmental scanning electron microscope (ESEM), where the sample chamber can be filled with a gas vapour, such as H<sub>2</sub>O.

Thanks to the use of electrons as a source of sample illumination, an electron microscope can achieve a much higher resolution than a conventional light microscope. This is clear when one considers the simplified version of the de Broglie relations, and the Rayleigh Criterion for lateral resolution described before. According to the de Broglie hypothesis, electrons have a wave-particle duality. Here, the de Broglie wavelength on an electron ( $\lambda$ ) is related to its momentum ( $\rho$ ) through the Planck's constant ( $h$ ) (equation I). Where the momentum of the electron is related its velocity ( $v$ ) and mass ( $m$ ) (equation II).

$$\lambda = \frac{h}{\rho} \quad (\text{I})$$

$$\rho = mv \quad (\text{II})$$

Given that the electrons potential energy of the electron (reflected in the acceleration voltage) (equation III) is converted to kinetic energy (equation IV), the wavelength of electron can be calculated by rearrangement of these equations and by substituting them into the de Broglie wavelength equation (equation V). This is the simplified version not taking into consideration special relativity theory.



$$E_{PE} = eV \quad (\text{III})$$

$$E_{KE} = \frac{1}{2}mv^2 \quad (\text{IV})$$

$$\lambda = \frac{h}{\sqrt{2meV}} \quad (\text{V})$$

Now, recalling the Rayleigh Criterion (equation VI), the refractive index ( $\mu$ ) for TEM corresponds to vacuum and is therefore equal to 1. Furthermore, given that the half angle of collection ( $\beta$ ) for electron beam is very narrow the entire denominator can generally be approximated to  $\beta$ . Therefore, for an electron microscope the simplified theoretical resolution is directly related to the wavelength of the electron (equation VII), and can be in the sub Angstrom range (less than a nanometre). As seen in the equation for the de Broglie wavelength, it will depend on the acceleration of acceleration voltage of the beam.

$$\delta = \frac{0.61\lambda}{\mu \sin \beta} \quad (\text{VI})$$

$$\delta = \frac{0.61\lambda}{\beta} \quad (\text{VI})$$

The practical resolution of an electron microscope is however lower than this due to the imperfection of the electron optical system. In particular, spherical and chromatic aberrations of the lenses affect the sharpness and size of the beam. The spherical aberrations originate from the difference in the strength of the lens, across the plane of the lens. Here, electrons that are further away from the optical axis, are deflected more than those closer to it. The Chromatic aberrations on the other hand come from the energy spread of the electrons. Electrons of higher energy move faster, and therefore are less deflected by the lens. Together, these result in the electrons being focused in different planes. Today, spherical aberration correction is common and is based on the introduction of additional multipole lenses (typically a hexapoles), either only to pre-but also to post specimen lenses depending on the microscope setup/operation mode (described in more detail below).

### 3.3.1 Scanning electron microscope (SEM)

Scanning electron microscope is one of the two common electron microscope setups, and is commonly used to analyse the surface and composition of a sample. Here the electron beam that exits the column is scanned across the sample with help of electromagnets/coils. This is done in a raster-like pattern across a rectangular area. Electron detectors capture the generated electrons and, when sent through a photomultiplier, the signal is converted into a voltage signal, which eventually is used to generate an image. Due to this setup, the area of analysis, referred to as the field of view (FOV), can be very large in an SEM instrument (in difference to TEM, discussed below).

The majority of the electrons detected in SEM are either secondary electrons (SE), or backscattered electrons (BSE), for surface analysis, as well as energy dispersive x-rays (EDX), which are useful for analysis of the composition of the samples (particularly in material science, details in TEM section). An SEM instrument is most often operated at voltages up to 30kV, which results in it having the maximal resolution of down to sub-nanometre. While this is much less than a TEM (discussed below) SEM does have its advantages.

The SE generated in SEM can produce images that appear to have a topographic contrast. This takes place due to the fact that even though the SE are generated throughout the entire interaction volume of the electron beam, they can only escape if they are near the surface. As a result, brighter and darker regions appear in the image due to the topography of the sample. Further, topographic contrast is also obtained thanks to the great depth-of-field of an SEM (as compared to a conventional optical microscope). An SEM is also able to provide surface atomic number contrast thanks to the detection of the BSE. As described above, this arises due to the fact that heavier elements scatter electrons more efficiently than lighter elements. These show up as brighter regions when the BSE detector is used.

An important advantage of an SEM is the simplicity of the sample preparation needed, namely minimal or no sample processing is needed. Instead the samples are typically

mounted, and maybe sputter coated. Sample sputter coating is done through the deposition of a very thin (nm thick) layer of, for instance, gold, carbon or palladium. This increases the surface conductivity and decreases the surface charging, which otherwise would perturbate the primary beam and affect image generation.

Biological samples are typically not very conductive, and sputter coating is thus very useful. Further, they are often “hydrated”. In those instances, the use of an environmental scanning electron microscope (ESEM), mentioned above, can be very beneficial when working with such samples. An ionization gas (such as H<sub>2</sub>O) is used to amplify the SE signal and suppress surface charging artefacts as the positive gas ions that get attracted to the negatively charged surface. This Setup removes the need for sputter coating. Importantly, samples can be analysed without vacuum. Unfortunately, this comes at the cost of resolution.

### **3.3.2 Transmission electron microscope (TEM)**

Transmission electron microscope (TEM) is the second of two common electron microscope setups<sup>334</sup>. As suggested by the name, the electrons that have been passed/transmitted through the sample are collected. These can provide information about the inner structure of the sample, such as the morphology in a biological sample, or the crystal structures and stress mechanics that are often of interest in material sciences.

In a TEM a broad stationary electron beam is focused on the samples, rather than scanned as is done in a SEM. Further, the image generation is done directly, either by projecting the electrons through intermediate and projection lenses (located below the sample) onto a fluorescent screen or a charge-coupled device (CCD) camera. As a result, the field of view (FOV) of a TEM is much smaller than that of an SEM. This also implies that only two-dimensional projections are generated, with no depth-of-field which is maintained in SEM.

In contrast to an SEM, a TEM is also operated at a much higher voltage of 60-100 kV, but measurements at 300kV have also been performed. The higher acceleration voltage

implies that the TEM can achieve a significantly higher resolution. With the use of pre-and post-sample aberration correction of the beam, a resolution down to as low as tens-of-picometres has been achieved (below 1 Angstrom). Typically, the images generated in a TEM result from the electrons that are transmitted through the entire thickness of the sample. Therefore, the samples need to be very thin (around 100nm), otherwise many electrons from the primary electron beam will be absorbed. TEM is always operated at a high vacuum, and therefore requires much more sophisticated sample preparation than SEM. This is particularly important for biological samples (described in detail below).

Generally, the number of transmitted electrons in a TEM is proportional to the brightness. The contrast on the other hand can be obtained by monitoring the electron scattering (as well as the phase of diffracted electron in a more advanced analysis). The principle behind the scattering contrast is that the electrons that are scattered at a large enough angle will not reach the detector (darker). Obviously the thickness of the sample will affect the scattering, but importantly, the contrast will also depend on the atomic number of the elements in the sample. As mentioned above, heavier elements will scatter electrons more broadly. In biological samples, the scattering contrast is most commonly used and is achieved by the means of sample staining with heavy metals (described later).

Importantly, the scattering can be both inelastic and elastic. The inelastic scattering implies that the electrons lose energy. This loss can be characteristic to particular atoms, and can be analysed by earlier mentioned energy dispersive x-ray (EDX) spectroscopy, or Electron energy loss spectroscopy (EELS). Together, these spectroscopic approaches can be useful in identifying chemical composition of the materials.

If the scattering is elastic, diffraction contrast can also be obtained in TEM. Here the contrast is obtained from the constructive interference of electrons that have not lost their energy. This approach is particularly useful for the analysis of atom organization in a crystal lattice. Finally, due to the fact that the transmitted electrons and diffracted

electrons are not in phase, an interference pattern is generated. This pattern is referred to as a phase contrast. Together, diffraction contrast and phase contrast are extremely useful in material sciences (particularly nanoscience), not only to analyse earlier mentioned crystal structures, but also to identify dislocations, boundaries or areas of mechanistic stress in the samples.

### **3.3.3 Scanning transmission electron microscope (STEM)**

The scanning transmission electron microscope is a third “setup” on an electron microscope. Technically, however, it is not an independent electron microscope, but rather a mode of operation. It is compatible with both the TEM and SEM system. In fact, it is a combination of both these systems. In the STEM, the beam is finely focused and scanned across the sample (as in SEM), the image generated however is that of transmission electrons (like in TEM), rather than that of SE or BSE. Therefore, the sample preparation for STEM is similar to that of TEM (discussed below).

STEM can take advantage of both setups, such as operating at both low and high voltages. At the same time, it is still possible to be used in combination with the earlier mentioned spectroscopic techniques such as EDX and EELS. The true advantage of STEM originates however from the fact that this setup uses scintillators, rather than a CCD camera (as in TEM), to collect transmitted and scattered electrons. As a result, the image is constructed on a pixel-by-pixel basis (similarly to SEM), and is therefore capable of providing information about the inner structure of the samples at an extremely high resolution (even higher than that of TEM)<sup>335</sup>.

In detail, if the electrons are scattered at a low angle, a standard fixed scintillator is used for collection (bright field, BF). The BF-STEM signal relies on phase contrast, and hence the signal intensity is not directly proportional to either the thickness or the atomic number. Therefore, it is more suited for use when the contrast dependent on elemental composition is less relevant. This is typically the case for biological samples.

When electrons are scattered at a higher angle, they are collected using a movable annular (ring shaped) scintillator (high angle annular dark field, HAADF). The signal in these images is not dependent on the phase contrast, but is rather directly

proportional to the atomic number. This allows for quantitative analysis, such as mass measurements, also shown to be possible in biological setting.

### **3.3.4 EM preparation of biological samples**

As mentioned above, both TEM and STEM analysis require very thin samples. There exists a wide variety of sample preparation methods available, some of them are tailored to biological analysis, others to the analysis of materials<sup>334,336,337</sup>. The focus here lies on biological sample processing.

Biological samples must be able to sustain high vacuum of the electron microscope. In order to do so they must be fixed and immobilized. Typically this is achieved through chemical fixation (described in detail below). Alternatively, given the recent developments of cryogenic (Cryo-) SEM and TEM, samples can be immobilized in the hydrated state by freezing. This approach offers tremendous advantages for the analysis of small molecules, such as proteins, where the native structure and conformation are of interest. Further, it offers the possibility to maintain the native localization of small molecules and ions in the specimen. However, the Cryo approaches are not very useful for large samples (beyond >500nm), such as tissue pieces.

#### **3.3.4.1 Fixation**

Tissue samples (and commonly also cells) are typically prepared through chemical fixation. This involves chemical stabilization/fixation of the sample, followed by dehydration, embedding in plastic resin and sectioning (typically on a scale of few 100-200nm). Often this is also complemented with contrasting.

The aim of chemical fixation is to protect the sample from any kind of damage that could occur during follow up dehydration and embedding. Two of the major commonly used groups of fixatives include aldehydes (paraformaldehyde (PFA) and glutaraldehyde (GA)), and oxidizing agents (osmium tetroxide (OsO<sub>4</sub>), and potassium permanganate (KMnO<sub>4</sub>)). These stabilize the tissue by cross-linking proteins. The fixatives are typically buffered and also include substrates such as electrolytes and non-electrolytes, or even dyes.

The idea behind fixatives is that they will preserve morphology and structure by preserving the cellular components. This is done by stabilizing the main macromolecules, particularly through cross-linking of proteins. Other macromolecules, such as carbohydrates, lipids or chromatin network (RNA, DNA) are typically less preserved. PFA is the smallest molecule, and also the fastest penetrating fixative, however its chemical reaction with the substrate is reversible. GA, on the other hand, is much slower, but its reactions with the substrate are irreversible and stabilization of the substrate is facilitated through cross-linking reactions with the amino groups. The  $\text{OsO}_4$  is the slowest of these fixatives. It is a heavy metal that denatures the proteins, by causing them to unfold. Unfolding exposes the interaction sites for osmium, and hence  $\text{OsO}_4$  acts as a contrasting agent. It is however not able to cross-link the majority of proteins, and is therefore used as a post-fixative.

Optimization of chemical fixation is not easy as the process can introduce different artefacts. These can be distinguished from disease related processes by, the changes in size, shape, electron density or the location of the cellular components within the cell. Therefore, in order for the chemical fixatives to achieve their aim several aspects need to be considered. These include osmolality, pH and temperature.

Given that cells have semipermeable membranes that discriminate between molecules and ions, the concentration of these outside and inside the cells can differ. Together they will exert osmotic pressure that might lead to either the swelling or the shrinkage of the cells. Therefore fixatives (and buffers they are dissolved in) need to be adjusted to compensate for this effect. This can be done with help of electrolyte salts (e.g. NaCl), or non-electrolyte molecules (e.g. sucrose). The osmolarity needed depends on the type of the tissue, as well as the fixation method (perfusion, immersion etc.). Generally, for tissue a total osmolarity of ca 700 mOsm is used, and effective of 300 mOsm is used.

The pH of the fixative affects the nature of the proteins, their structure and conformation, and thereby the cellular morphology. The charge on the proteins reflects the content of the basic and acidic groups present. When the protein is at its isoelectric point, it is least soluble. While the isoelectric point of the majority of the proteins is 4-

7, the pH of the cellular components is slightly higher at a range of 7-8. At a higher pH, the hydroxide ions react with positively charged groups on the protein, making it negatively charged. The pH of the fixative has to be close to the physiological pH of the cells or tissue, otherwise it will affect the structure and properties of the protein, thereby affecting its morphology. The pH of the fixative is generally adjusted depending on the tissue, cells and the target analysis, e.g. cytoplasmic vs nuclear constituents.

Temperature affects the majority of cellular processes that take place after death, e.g. speed of leakage of cellular components or rate of enzymatic degradation processes. These processes, which result in the deterioration of ultra-structures, proceed faster at higher temperatures. At the same time however there is a trade-off, the temperature also affects the speed of chemical reactions between the fixative and cellular constituents, and the speed of a fixative's penetration. These processes advance more quickly at high temperatures. Optimally, the fixation should be carried out in as close to the physiological temperature of the specimen as possible. Depending on the fixative, what specimen is analysed, a combination of cold and long fixation, as well as the length of exposure to these, is typically determined. Commonly, quickly penetrating fixatives are used at room temperature for a short period of time (e.g. PFA), whereas slowly penetrating fixatives are used over a long period of time at low temperatures, 4°C. (e.g. OsO<sub>4</sub>).

As mentioned above, fixatives are prepared in buffers. These ensure that no acidification of cellular components takes place in the specimen. The majority of the buffers used are most effective in the physiological range (pH 7.2-7.4). Hence, dimethylarsinic acid sodium salt trihydrate, known as the sodium cacodylate, is most commonly used. While toxic, this buffer offers great buffering capacity (pH 5-7.4), can be stored for long periods of time, typically does not form precipitates, and can be spiked with divalent ions (such as Ca<sup>2+</sup> or Mn<sup>2+</sup>) in order to adjust osmolarity, and is compatible with PFA, GA, and OsO<sub>4</sub>.



A common, non-toxic alternative is the phosphate buffer, either Millonig's, or Sörensen. While these mimic the extracellular fluids, they are hypotonic (low osmotic pressure), and therefore need to be supplemented with sodium chloride. Further, during fixation they can form precipitates, in particular in the presence of calcium ions, or uranyl acetate (UA) during *en bloc* staining (described below). Few other buffers include veronal-acetate buffer (useful for UA *en bloc* staining, but reactive with aldehydes), toxic collidine buffer (useful for post-fixation with OsO<sub>4</sub>, but works poorly with PFA, and with GA), and Tris buffer (has great buffering capacity at higher pH, which is sometimes needed, but contains primary amines that react with GA).

#### **3.3.4.2 Dehydration**

Dehydration is a crucial step before the specimen enters the vacuum of the electron microscope. It is also important since the majority of the embedding media that are used for further processing are non-polar, and hence not soluble in water. The dehydration process does however destabilize the interactions of the non-polar chains on the inside of the protein, which makes it unfold and more likely to be extracted. In general, it is responsible for significant tissue shrinkage and a loss of proteins, lipids and carbohydrates. Therefore, it should be carried out at low temperatures (ca 4°C), and be performed quickly. A prior fixation (as described above) is also crucial for proper tissue preservation due to this reason. At the same time, however, the specimen needs to be rinsed in buffer between fixation and dehydration steps. This is done because the fixative and the dehydrating agents might interact with one another. This should also be done at a low temperature (ca 4°C), with a few quick rinses, to minimize protein denaturation.

Dehydration is carried out in several steps. Here the specimen is subjected to serial rinsing in increasing concentration of solvent(s) that gradually remove the water. These can be ethanol, methanol, or acetone. While an increasing gradient of ethanol is very effective to remove water, ethanol is not optimal to dissolve the embedding media. Therefore, following the rinses with an increasing gradient of ethanol, specimens are often rinsed in absolute acetone (water free). Not only is it compatible with the majority of embedding media, it also causes less shrinkage of the specimen, and retains

more macromolecules, such as phospholipids. An alternative to acetone that is often used is 1,2-epoxy propane (propylene oxide). It is very efficient at dissolving many of the embedding media, however it is also very reactive and can interact directly with cell constituents, or even the embedding media itself, preventing its polymerization. Therefore, acetone is often recommended as the intermediate between dehydration and embedding.

#### **3.3.4.3 Embedding**

Embedding of the specimen is done in an embedding media, known as resin. The aim of using a resin for embedding is to stabilize the specimen and help to preserve fine structure (by further cross-linking). This means that the resin should induce as little changes in the specimen as possible during the embedding, while providing it with stability both for sectioning but also exposure to electron beam. Resins are typically described in terms of their polarity, viscosity, and hardness. Polar resins are compatible with water, and often can be used for embedding without prior fixation. Less viscous resins (before polymerization) penetrate the specimen quicker. The resin's hardness will affect how easy it will be to section the specimen.

There are a wide variety of resins available, and their use depends on the purpose of the study. However, the majority of the resins belong to either epoxy or acrylic resins. These are typically prepared by mixing the resin itself with a plasticizer, hardener and an accelerator, which modify the properties of the resin during the infiltration, polymerization, sectioning and analysis. All of the resins are strong irritants

Infiltration with the resin is typically done in several steps, where ratio of the intermediate solvent to resin is gradually decreased, and is finished off with a few exchanges of pure resin. Following the infiltration, resins are polymerized (cured) with the help of either heat (at around 60°C) or UV light in small capsules (these aid in further sectioning). In some cases, resin can also be polymerized at low temperatures (-40°C to -80°C) with the help of UV and accelerator (e.g. *Lowicryl* resin). This is typically done through freeze substitution, where a frozen thin specimen is processed at negative temperatures until fully embedded in resin. Though expensive, this

approach offers the possibility to obtain samples of extremely high morphological preservation (often not needed).

Among epoxy resins, *Epon*- and *Araldite* resins are the most commonly used<sup>338-340</sup>. These resins are well suited for high resolution EM analysis. Further, *Spurr's* resin is compatible with ethanol and has very low viscosity. Therefore, it can be used for quick preparation of the sample<sup>339,341</sup>, but it is highly carcinogenic. Among acrylic resins, *LR White* and *LR Gold* have the advantage of being hydrophilic, having low viscosity and being suitable for cold polymerization<sup>342,343</sup>. Another acrylic resin, *Lowicryl*, can be either hydrophilic or hydrophobic, and polymerizes at low temperatures<sup>339,344</sup>.

In general, the hydrophilic acrylic resins, such as *LR White* and *LR Gold* are well suited for follow-up immunolabelling, without the need for special treatment of the tissue that could affect the antigens<sup>339,345</sup>. However, staining of highly cross-linked and very stable epoxy resin is also possible, but requires sample pre-treatment<sup>346,347</sup>.

#### **3.3.4.4 Sectioning**

Following embedding the capsules with the specimen are sectioned. This is done on an ultramicrotome. Here the capsules/blocks are typically first trimmed using a glass knife. The glass knives are not very durable, but are cheap. They are useful for obtaining 1-4µm thick sections, which can be used for finding regions of interest in the specimen. The edges of the specimen block can then be trimmed and a diamond knife can be used to cut very thin (several tens of nm, generally 80-150nm) sections. Diamond knives are very expensive and can easily be damaged; therefore they should only be used for cutting sections up to 500nm in thickness. Generally, while trimming with the glass knife can be performed at a fairly high speed, cutting with the diamond knife should be done much more slowly.

Once cut, the ultra-thin sections are typically mounted on grids. These are usually made of copper or nickel, however gold grids are also available. These are typically 3.05 mm in diameter. The number of bars present in the grid, per inch of the grid, is referred to as mesh. A smaller number means fewer squares (but often thicker individual bars), and hence a larger percent of the area is open. However, this implies

that the grid provides less support for the sample. Generally, the number of mesh in the grid ranges from 50-1000 mesh. In order to provide extra support, grids can be coated with new nanometre thick layers of, for example, carbon or plastic (formvar) or even both. While these support films improve sample stability, they might negatively affect the final resolution, cause charging or even interact with contrasting agents if such are used.

#### **3.3.4.5 Staining**

Generally, biological sections have poor contrast (although osmium tetroxide often used as post-fixative is a heavy metal and does provide some contrast)<sup>348,349</sup>. Therefore, they are often stained/contrasted. This can be done during the chemical preparation (after dehydration but prior to infiltration), referred to as *en bloc* contrasting, or after sectioning (by floating the grids with the sections upside-down in the contrasting agent). Staining of the samples after embedding however is generally not the easiest. This is due to the fact that the commonly used embedding media (e.g. *Epon* och *Araldite*) are non-polar, while the stains are most often polar. Further, in ideal case, contrasting should be specific to certain components in the specimen. It is however generally not the case and the commonly used staining solutions contrast several different components of the specimen at the same time. Therefore, staining recipes and protocols are often adjusted based on the type of specimen and its processing.

Contrasting is categorized into negative staining (where the background is stained) and positive staining (where the actual specimen is stained). The interaction of the stain with the specimen depends on several different factors. In particular, the pH of the stain and sample, and to some extent the isoelectric point of the proteins, will significantly influence the staining. These are in turn affected by the fixation and buffers used. Further, even the support film (if used) might modify the way the stain interacts with the sample.

In general, if the pH of the stain is higher than the isoelectric point of the protein, this will result in an overall negative charge on the protein, making it more prone to interact with cations in the stain. If the stain pH is lower, the opposite will be the case. The pH

of the stain also has a broad effect on the overall staining efficiency. Generally, at low pH, the staining agent will interact with the acidic environment on the surface making the surface detail well pronounced. On the other hand, at a high pH the staining agent will penetrate better. Taken together, the same stain at different pH values might actually stain different cellular constituents.

Two of the typically used stains have either lead or uranium as their contrasting agents<sup>350,351</sup>. Both of these stains come in different solutions, and therefore have different pH values. Lead is always alkaline, and is used for instance as lead acetate, lead hydroxide, or lead citrate (in increasing pH order). The higher the pH, the higher the binding capacity of the  $Pb^{2+}$  ion. It interacts for instance with -SH groups of proteins, -OH groups of carbohydrates, forms complexes with nucleotides and nucleic acids, and results in strong staining of extracellular membranes.

Uranyl, the oxycation of Uranium, is mostly available as an acetate or a nitrate. It is acidic and the acetate salt of uranyl (UA) is widely used for negative staining. In fact, the solution typically contains both positively and negatively charged ions, which can interact with not only positive but also negative side-chains of a protein, providing stark contrast. UA can be used for both staining of cut sections but also for *en bloc* staining. *En bloc* staining with UA might however enhance the extraction of the membranes during dehydration. UA has a high affinity for phosphate groups in phospholipids, and even more so for the nucleic acid. Often, lead citrate and uranyl acetate are used together for tissue staining in order to enhance contrast (lead interacts with uranyl). In such case, however, uranyl acetate has to be used first, and the specimen needs to be thoroughly rinsed with an alkaline solution before and after lead citrate staining. Otherwise, lead precipitation at low pH will result in artefacts.

In addition to the more general contrast staining agents used in electron microscopy, more targeted approaches have also been developed. One of these is immunogold labelling<sup>352</sup>. Here, following the sectioning, the specimen is incubated with gold-nanoparticle conjugated antibodies. The electron dense gold-nanoparticle appear as dark spots at the regions of antibody binding. While useful, this approach is suitable

primarily with polar resins, such as LR White. Unfortunately, it suffers penetrability and specificity issues, associated with extensive tissue fixation, dehydration and embedding.

Another approach is a 3,3'-diaminobenzidine (DAB) photooxidation-guided analysis<sup>353</sup>. Here, selective fluorescence labelling of a particular tissue structure prior to chemical fixation is combined with photo-oxidation of osmiophilic DAB. The precipitated DAB is prone to interact with OsO<sub>4</sub> during fixation, resulting in localized electron dense features. This approach has been recently expanded to facilitate “multicolor EM” analysis, through the use of electron energy-loss spectroscopy (EELS) (mentioned above)<sup>354</sup>. The authors generated DAB-Metal Chelate Conjugates that contain different lanthanides (Ln). Through subsequent fluorescent stainings, and photooxidation of DAB-Ln conjugates, the metals are deposited at the selected location. The conventional TEM analysis can then be complemented with an EELS analysis of these rare metals. This enables visualization of specific cellular constituents at the electron microscopy resolution.

### 3.4 Mass spectrometry

Mass spectrometry (MS) is a powerful analytical technique that has become a valuable tool in bioscientific research. MS analysis offers the possibility to determine the molecular mass of a variety of compounds, including among others, metabolites, lipids, peptides, intact proteins, and even protein complexes<sup>355</sup>. An MS instrument consists of 3 major parts: a source, an analyser and a detector. In the source, the analytes are ionized (gaining either a positive or negative charge), and transferred into the gas-phase. Generated ions are then separated according to their mass-to-charge ratio (expressed as  $m/z$  value) in the mass analyser. Finally, they are measured when they reach the detector. Given that the ions are very reactive species, mass analysis operation requires a very low pressure.

The expression  $m/z$  that is commonly used in mass spectrometry is considered a dimensionless quantity that corresponds to the mass of an ion (in unified atomic mass units (u)), divided by the charge of that ion (regardless of its polarity). This can be

confusing as neither mass nor charge are dimensionless. The  $z$  value however, which represents the number of charges, is indeed dimensionless. In MS, the unified atomic mass unit will most often not be written as “u”, but rather as Dalton (Da). Therefore, when the mass of the parent neutral molecule detected in an MS experiment is calculated from the  $m/z$  value, it will be expressed simply in Da units.

For a spectral peak in MS to be considered an actual signal, it should preferably be Gaussian shaped, and consists of at least 3 sampling points. That being said, a greater number of sampling points is desired. Further, these peaks should be at least 3 times the size of standard deviation of the background noise (referred to as signal-to-noise (S/N) ratio). This is also considered the general detection limit in MS.

When working with MS, there are often discrepancies between the measured mass and the actual theoretical mass of an analyte. This deviation is referred to as mass accuracy. Mass accuracy is represented in terms of mass error. This is calculated as the difference between the monoisotopic mass of the theoretical exact mass, and the measured accurate mass (equation 1). By convention, it is however often expressed as mass error in parts per million (ppm) (equation 2).

$$\text{Mass Error} = (\text{Exact Mass}) - (\text{Measured Mass}) \quad (\text{I})$$

$$\text{Mass Error (ppm)} = \left( \frac{(\text{Exact Mass}) - (\text{Measured Mass})}{(\text{Exact Mass})} \right) 10^6 \quad (\text{II})$$

Often, one mass spectrometry approach cannot handle all the demands posed by the problem. Therefore, one often needs to prioritize the parameters of an analysis based on the target. Sometimes, it is also useful to combine several different techniques. This allows for the utilization of technique-specific advantages for confident and sensitive identification of target analytes in complex settings.

### 3.4.1 Ionization techniques and mass analysers

In order to perform an analysis of analytes by mass spectrometry these need to be introduced into the gas-phase and ionized. Sometimes, the analytes are already in the gas-phase and require only ionization. Oftentimes, however, samples are introduced as

either solids or liquids and therefore need to be volatilized either prior to or during the ionization process.

There exists a variety of ionization techniques. Depending on the analytes of interest, different ionization approaches need to be chosen (for volatile/non-volatile and atomic/molecular ions etc). Here, one typically refers to either “soft” or “hard” ionization techniques. Soft ion sources produce intact ions of large molecules, e.g. intact proteins. Hard ion sources yield fragmented molecules. The “softness” and “hardness” of an ionization approach can vary ranging from enabling characterization of weak molecular interactions in clusters formed by aggregation, to isotopic ratio measurements by atomizing the analyte. There are a large number of methods for ion generation, and new ion sources are constantly being developed. These are then coupled to a variety of different mass analysers and, later, detectors, to make the highly complex mass spectrometer suitable for different purposes.

When it comes to intact peptide and protein analysis, two techniques are commonly used: the soft ionization techniques are electrospray ionization (ESI) and matrix-assisted laser desorption/ionization (MALDI). These approaches have also been extended to apply in form of imaging mass spectrometry (IMS). Another, technique used in the context of imaging MS is the secondary ion mass spectrometry (SIMS). MALDI and SIMS are discussed in detail below.

Mass analysers are used to separate ions according to their mass-to-charge ratio (expressed as  $m/z$  value). There are multiple different mass analysers used at MS instruments (and often their combinations). These include low-resolution analysers such as quadrupoles and iontraps, medium resolution time-of-flight (TOF) analysers and high-resolution magnetic sector, orbitrap, or fourier transform ion cyclotron resonance (FTICR) analysers. The use of different analysers often represents a trade of between their cost, and size, speed of operation and mass range suitable for analysis, and ability to separate, two closely spaced in mass, analytes (mass resolution).

The measure of the smallest difference in mass between two spectral peaks that can be separated by a mass analyser is referred to as mass resolution. In this context, the mass



resolving power is a term used as an indicator of performance of an instrument. The mass resolution, or mass resolving power, are reported using a dimensionless ratio  $m/\Delta m$ . There are more than one ways to establish the  $\Delta m$  and thereby the ratio. A commonly used peak width definition, is based on the full width at half-maximum (FWHM) measurement. Here the peak width,  $\Delta m$ , of a given  $m/z$  is measured at 50% of the peak height. This value is easy to obtain; however, it does not directly address the peak separating capability. Mass analyser common for MALDI and SIMS are discussed below.

#### **3.4.1.1 Matrix-assisted laser desorption/ionization MS (MALDI-MS)**

Matrix-Assisted Laser Desorption/Ionization (MALDI) is a special case of laser desorption/ionization (LDI), where a chemical compound (matrix) is used to assist sample ionization and desorption. Here, two related approaches were independently introduced in 1988. One was created by Karas and Hillenkamp (organic matrix), and the other by Tanaka et al (inorganic matrix)<sup>356,357</sup>. Since its development, MALDI revolutionized the biological research by allowing the detection of analytes in complex mixtures that contain large amount of salts. MALDI has been demonstrated to be suitable for analysis of not only non-volatile, but thermally labile compounds without the need for derivatization. This even includes proteins and peptides with posttranslational modifications (PTMs). Further, it has been shown to be suitable to produce gas-phase ions of intact, high molecular weight molecules, even up to few hundred kDa.

The idea behind matrix assisted LDI is that the sample is prepared with an excess of matrix-to-analyte ratio. Upon irradiation laser energy delivered to the surface, rather than directly impacting the analyte (like in LDI), is dispersed as vibrational energy across the matrix molecules. Consequently, this affects binding forces and the integrity of the co-crystallized matrix and analyte molecules. Their reduction results in an explosive breakup, with the matrix and the analytes (previously trapped in the crystals) being ejected. These can be either neutral or charged. As the ejected matrix and analyte might interact with one another in the ion source, the source is typically operated at a high vacuum (ca  $10^{-6}$  torr).

In MALDI (just like in LDI) the sample is irradiated with short and intense laser pulses (typically in nanosecond range). In general, two types of lasers are used for this purpose, either the IR or the UV wavelength range lasers. While the IR lasers have several advantages, the UV lasers are most commonly used.

There is a wide variety of sample preparation methods available for MALDI that have been used. Commonly solid matrix-analyte based deposition approaches are used (some described in more detail below). In addition, the use of liquid matrices has also been demonstrated<sup>358</sup>. While less common, the liquid matrices offer the possibility to obtain a very even distribution of the analyte-matrix mix.

One of the most common methods (and simplest) used for MALDI sample preparation of the solid matrix- analyte mixes is the dry-droplet method<sup>359</sup>. It involves mixing the matrix with the analyte and then depositing the combined solution at the target surface. When on target, the droplet starts to crystalize due to evaporation. Here the crystallization process is initiated at the surface of the droplet where it is in contact with air. From there, the crystallization progresses throughout the sample by convective heat transfer. This method, while easy to perform, results in the formation of a highly inhomogeneous surface, where larger crystals are typically formed at the edges of the dried droplet, and the crystal size and numbers varies greatly, both within and between preparations. Of course, this process is dependent on the type and amount of solvents and matrix used. Overall, the dry-droplet method does however suffer from poor spectra quality and mass accuracy. Worth mentioning is a modification of this method, namely the vacuum drying method. Here, instead of free evaporation, the drop is instead rapidly dried under a vacuum<sup>360</sup>. This has been shown to yield a better mass accuracy and resolution, which has been attributed to a decrease in the size of individual crystals and an increase in overall crystal homogeneity.

In order to further improve the signal strength and quality, several multi-layer approaches have been developed. Here a common technique is the seed-layer method which involves pre-deposition of a matrix layer (with the matrix being dissolved in a highly volatile solvent, e.g. acetone), prior to standard dry-droplet deposition of the

analyte-matrix mix<sup>361</sup>. Similarly, in the crushed-crystal approach, twisting a flat glass object on top first crushes the “seed”. The loose material is then brushed away before the dry-droplet deposition is performed<sup>362</sup>. The crushed crystals function as the seed and shift the crystallization process away from the top liquid-air interface towards the bottom and the pre-formed microcrystals. Both approaches yield a more uniform analyte surface, facilitate ion formation, and result in improved mass accuracy and resolution. Finally, derived from the vacuum drying and seed-layer method, comes the sandwich method where the matrix, then analyte, and then the matrix again, are deposited separately<sup>363</sup>.

Finally, worthy of mention are the electrospray and the airbrush methods. In an electrospray, the matrix or the matrix-analyte mixture are ejected from a stainless-steel capillary onto a grounded target plate by applying a high voltage potential<sup>364</sup>. The airbrush, which is considered a simpler and cheaper version of the electrospray, uses a compressed airbrush to spray the solution onto the target plate<sup>365</sup>. Both have shown excellent reproducibility and superior crystal homogeneity. Airbrush is commonly used in sample preparation for MALDI based imaging mass spectrometry (IMS, discussed below).

MALDI matrix compounds should be able to facilitate ionization of the analytes they surround without excessive heating (analytes are often thermally labile). They should reproducibly provide maximum possible ion intensity, while minimizing analyte fragmentation, and adduct formation (which reduces sensitivity and accuracy). Most importantly, due to obvious reasons, MALDI matrices themselves should not produce ions of the same  $m/z$  value as the analytes of interests.

For their optimal performance, matrix molecules have to incorporate the analyte molecules into the lattice structure during the crystallization. In order to do so, they have to reduce the intermolecular forces between the analyte molecules to prevent their precipitation and/or aggregation. Therefore, matrix compounds and analyte have to be soluble in the same solvent. At the same time, they should not react with the analyte, as this might result in undesirable modifications. Further, they must also be relatively

vacuum stable, as majority of the instruments used (UV-MALDI) are operated at high vacuum.

There is a wide variety of matrix compounds available. The UV-MALDI matrixes are typically low molecular weight organic aromatic compounds (in IR-MALDI H<sub>2</sub>O ice or glycerol are often used). Different matrices (and their derivatives) are more or less suitable for the analysis of various analytes. Typically, they are small molecules that yield high background/interference (overlapping m/z values), up to 500Da. Several of the common matrices, and their use is provided below (Table 1). The ionization processes are not well understood; therefore, most often the choice of the matrix, and optimization of the solvent system is based on an educated trial-and-error approach.

The key characteristic of MALDI matrices is their high molar absorptivity at a certain laser wavelength that allows for their easy transfer into the gas-phase. Given that the majority of the instruments have a fixed wavelength laser, matrices might more or less efficiently absorb the laser light and may require an adjustment in the laser fluence. This will in turn affect the mass resolving power, as higher velocity ions will be generated (this is particularly true in axial TOF mass analyser, for detail see below).

Different matrices form different lattice structures during the crystallization process. In fact, the resulting crystals are dependent on the nature of the matrix-analyte combination, their concentration (absolute and relative), solvent used, as well as additives and/or contaminations (such as salts - can cause adduct formation and/or peak broadening). Indeed, modifying the matrix/solvent system has been shown to yield different relative intensities of various analyte components. Therefore, when optimizing the use of certain MALDI matrix one needs to consider these factors in order to achieve the best possible result. This is particularly the case when performing MALDI Imaging MS analysis where the spatial aspect is important (described in more detail below).

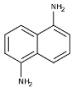
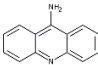
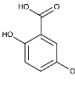
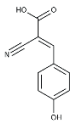
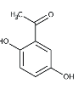
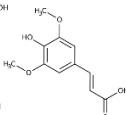
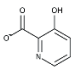
Matrix	Structure	Application
1,5-Naphthalenediamine (DAN)		lipids
9-aminoacridine		lipids
2,5-dihydroxybenzoic acid (DHB)		lipids, peptides, proteins
$\alpha$ -Cyano-4-hydroxycinnamic acid (CHCA)		lipids, peptides, proteins
2',5'-Dihydroxyacetophenone (DHAP)		lipids, peptides, proteins
3,5-dimethoxy-4-hydroxycinnamic acid (Sinapinic acid (SA))		proteins
3-Hydroxypyridine-2-carboxylic acid (3-Hydroxypicolinic acid (3-HPA))		oligonucleotides

Table 1. Common MALDI matrices and their use.

MALDI generates primarily singly and doubly charged positive and negative ions. However, the ionization process (transfer of charge between matrix and analyte), which is believed to take place following the generation of the plasma cloud by the laser, is generally considered to be highly inefficient. Recently, MALDI-2, an approach relying on secondary, laser induced ionization has been developed to improve the ion generation<sup>366-368</sup>.

The charge on the ions generated through MALDI (+/-1, +/-2), also imposes limitations when it comes to which mass analysers can be used. As mentioned above, an axial TOF mass analyser is typically used. This because the ions are generated in short bursts following the laser pulses. However, Fourier-transform ion cyclotron resonance (FTICR) instruments are the go-to standard when it comes to high resolution analysis. The FTICR instruments do however suffer from mass to charge range limitation (suitable for smaller molecules, but not proteins). Since the introduction of atmospheric pressure MALDI (AP-MALDI), where the ejected ions enter the vacuum through an orifice, other analysers, such as e.g. Orbitraps, have been used<sup>369</sup>.

### 3.4.1.2 Secondary ion mass spectrometry (SIMS)

Secondary ion mass spectrometry (SIMS) is an ionization technique that relies on the use of an ion beam (primary ions) for the desorption of molecules (secondary ions) from a given surface<sup>355</sup>. Typically, SIMS does not require any prior sample preparation. This with the exception of Nano-resolution SIMS (NanoSIMS, described below), and matrix-enhanced SIMS<sup>370-373</sup>. The applications of SIMS in a biological setting are much more limited than those of MALDI, or ESI, due to the high degree of molecular fragmentation induced by the primary ion beam (limited  $m/z$  range). In recent years, a growing number of imaging mass spectrometry (IMS) studies of biological samples have taken place. Here the profiling of lipids by TOF-SIMS, or isotopic distribution by NanoSIMS is most common. This profiling became possible mainly due to the development of new primary ion sources.

Upon interaction of the primary ions with the surface of the sample, the energy of the primary ions is transferred to the analysed material through a collision cascade, resulting in ions being sputtered away. The process of secondary ion generation is described in the SIMS equation (equation I).

$$I_m = I_p Y_m \alpha \theta_m \eta \quad (I)$$

Here, the secondary ion current of a species  $m$  ( $I_m$ ), depends on the primary ion flux ( $I_p$ ), the sputter yield ( $Y_m$ ), the ionization probability ( $\alpha$ ), the concentration of the species  $m$  in the surface layer ( $\theta_m$ ), and the transmission of the analysis instrument ( $\eta$ )<sup>374</sup>.

Given that the SIMS is typically operated on the order of several tens of keV, the majority of the molecular bonds (e.g. covalent, ionic etc.) in proximity of the impacted area are broken, resulting in extensive molecular fragmentation (with mainly atomic secondary ions being generated). The further from the impact area, the lesser the molecular fragmentation, and the higher chance that an intact molecular species will be detected. Overall, the process of secondary ion generation can therefore be considered rather destructive in nature. However, as the degree of surface damage

depends on the ion dose of the primary beam, SIMS can be categorized into static and dynamic SIMS.

For an analysis to be considered static, the instrument needs to be operated below the “static limit”, that is where the primary ion is below approximately  $10^{13}$  ions/cm<sup>2</sup> (the estimated 1% of surface atoms). Such analysis is considered “soft”, leaving the area generally unaffected, and yielding minimal molecular fragmentation. Unfortunately, this mode of operation is not very sensitive (less sample desorbed). When the primary ion dose exceeds the “static limit”, that is when the number of primary beam ions exceeds that of the surface atoms, and the analysis is referred to as dynamic SIMS. Dynamic SIMS results in both erosion of the sample, and high fragmentation of molecules.

SIMS analysis initially relied on the use of monatomic primary ion sources (e.g. gallium ions, Ga<sup>+</sup>). These ions, however, penetrated deeply below the surface, causing extensive fragmentation, and resulting in low secondary ion yield. Recently, the monoatomic ion probes have been complemented by cluster ion sources (e.g. Bismuth, Bi<sup>n</sup>, Argon, Ar<sup>n</sup>). These have been shown to induce a much lesser degree of fragmentation (and hence be much more suitable for the analysis of organic biomolecules), while also improving the yield of secondary ions. The introduction of these polyatomic cluster ion sources have also enabled the so called “depth profiling” (that is dynamic SIMS analysis) of biological samples, thanks to their lesser penetration depth upon impact. Lesser penetration, implies lesser degree of interlayer mixing, and lesser damage of the “deeper” atomic layers. In practice, this implies that the data is obtained as a function of depth, rather than a representative of the characteristic of the surface. This is of particular importance for 3-dimensional (3D) analysis in the context of SIMS based IMS.

The nature of the primary ion beam used in a SIMS analysis, that is for instance, size (mono-/poly-atomic, atomic number), charge, and current, result in a trade-off between resolution, sensitivity, and molecular fragmentation. The higher the energy of the primary electron beam, the more it can be focused. This concept is of particular

importance in IMS setting. At the same time, higher energy causes a higher degree of fragmentation. Here, in static SIMS, molecular ions above 300Da are often fragmented, while the dynamic SIMS produces primarily atomic secondary ions. As a result, SIMS has a relatively low mass range limitation (approximately  $m/z$  1000-1500).

Most often in the biological context, the SIMS is equipped with a pulsed ion source. Use of a pulsed ion offers several advantages, in particular when performing IMS. Most importantly, it allows for an effective compensation of surface charging (prominent in biological samples). This can be done by employing a low-energy electron gun (still, this can cause additional surface damage). Furthermore, instead of an electron gun, a second, interlaced ion gun can be employed to etch away the damaged surface. Here, a high sputtering rate, low penetration gun causing low damage (e.g. fullerene,  $C_{60}^+$ ) can be used. This can be particularly helpful for depth profiling (e.g. when performing IMS) in static SIMS mode.

The use of pulsed ion source also impacts the mass resolution and, in the context of IMS, the spatial resolution. In general, higher mass resolution is obtained with shortened ion beam impulses (e.g. in bunched mode with narrow, hundreds of picosecond long impulses). The result is a smaller spread in the energy distribution of the ions (especially important with TOF mass analyser, described below). However, this small distribution will negatively affect the spatial resolution, as the primary ion beam cannot be focused to the same extent. Hence, operating in non-bunched mode, with tens of nanoseconds impulses is better for spatial resolution (sub-micrometre).

The phenomenon of secondary ion generation greatly depends on the inner environment of the analysed material (both the chemical and electric). Therefore, it is important to consider these when designing an analysis. In the context of biological samples, aspects such charge compensation are important. Further, to correlate the concentration of an analyte with the intensity of the secondary ions generated, it's important to keep the ionization efficiency and extraction constant across the samples (important in IMS, and particularly in NanoSIMS). To facilitate this, SIMS



instruments are operated at ultrahigh vacuum. Working in ultrahigh vacuum conditions also helps preserve the morphology of the sample and analytes.

### 3.4.1.3 Time of flight (TOF)

First introduced by Stephens in 1946, the time-of-flight (TOF or ToF) mass analyser determines mass ( $m$ ) to charge ( $z$ ) values of analytes based on the flight time between the initial ionization event (e.g. laser pulse in case of MALDI, or primary ion beam pulses in SIMS) and the generation of an electric pulse when they hit a detector<sup>375</sup>.

Here, following the ionization, all ions with the same charge are accelerated towards the TOF mass analyser by applying an electrostatic extraction potential (either positive or negative,  $U$ ) between the sample (referred commonly to as target) plate and the ground potential at the mass spectrometer inlet. When leaving the acceleration region of the applied electric field, the electric potential energy ( $E_{PE}$ ) of the analyses (equation I) is converted into kinetic energy ( $E_{KE}$ ) (equation II). This conversion allows for correlation of the mass-to-charge ( $m/z$ ; where  $z$  is charge on the ion in electrostatic units  $\pm 1e$ ) to the velocity ( $v$ ) of the ions (equation III).

$$E_{PE} = zU \quad (I)$$

$$E_{KE} = \frac{1}{2}mv^2 \quad (II)$$

$$\frac{m}{z} = \frac{2U}{v^2} \quad (III)$$

Given that the ions are passing through a fixed length field-free tube ( $l$ ), and the electrostatic extraction energy ( $U$ ) is kept constant, a quadratic relation of time of flight ( $t$ ) with  $m/z$  can be established (equation IV).

$$\frac{m}{z} = \frac{2U}{l^2}t^2 \quad (IV)$$

$$\frac{m}{z} \propto t^2 \quad (V)$$

Therefore, given the direct proportional of mass-to-charge ratio to the square of time-of-flight (equation V), the smaller the mass-to-charge ratio of the ion, the faster the ions will arrive at the detector. In principle, this operational setup allows for the analysis of all ions that are fed into the MS instrument in a single experimental cycle.

Ideally, all ions of the same  $m/z$  value would leave the electrostatic extraction potential region at the same time. For this to be possible, ions should be extracted in a pulsed, rather than continuous matter. Here, both MALDI, and most often also SIMS, are pulsed sources and hence highly suitable sources for use with a TOF. This is in contrast to continuous sources, such as electrospray ionization (ESI).

MALDI-TOF (and SIMS) instruments, are typically set up in an axial configuration that allows ions to be directly accelerated into the TOF mass analyser, making them highly sensitive. An orthogonal set up of the TOF mass analyser, on the other hand, allows overcome the limitation of the continuous nature of a source, such as ESI. Here, trapping continuously generated ions and splitting them into small packages before sending them into the orthogonally set up TOF tube can be performed. Such orthogonal set up does however sacrifice sensitivity and speed of analysis. On the other hand, it provides higher resolution of the spectra by compensating for any spread of energy in the extracted ions.

In general, pulsed ion sources, such as MALDI, generate ions with a rather inhomogeneous energy profile due to the uneven spatial distribution and initial velocity of the analyte ions. This impacts both the inner energy and the kinetic energy of the generated ions, right at the moment of desorption. In order to compensate for this, two approaches have been developed: one is the delayed extraction (also known as time-lag focusing) and the other is the use of electrostatic ion reflectors (also known as mirrors).

The delayed extraction was introduced in 1955 by Wiley and McLaren, and is nowadays commonly used in MALDI-TOF instruments<sup>376</sup>. Here, the single-stage acceleration region was replaced by two-stage region. First, no electric field is applied at the time of desorption, but is instead switched on with a few nanoseconds delay. In

practice, this implies that before the acceleration voltage is switched on, ions of lower energy will travel less far towards the mass analyser inlet, than those of high energy. As a result, the slower ions of lower initial energy end up at a higher potential, and thereby are more accelerated than those of higher initial energy. When properly set up, the delayed extraction can compensate for the initial energy discrimination between the same  $m/z$  ions that originates from both the velocity spread and spatial dispersion. This setup results in higher mass resolution. The delay extraction time is mass dependent and hence the optimum settings will vary with the mass range of interest.

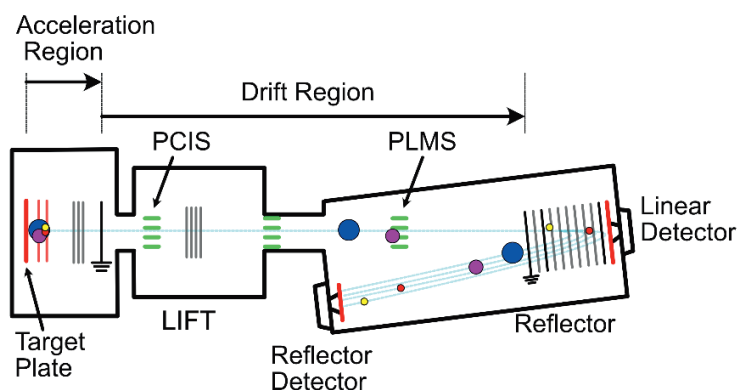


*Figure 5. Schematic view of MALDI TOF MS instrument including the component for LIFT-MS/MS. Following desorption, ions are accelerated (acceleration region), and enter the flight tube (drift region), where they are separated based on their  $m/z$  values. When operated in the normal mode, they can be either detected using linear detector, or reflected and detected using the reflector detector. When performing MS/MS analysis, post source decay (PSD) induced fragmentation is used. Here, a precursor ion selector (PCIS) is used to select precursor/mother ions and their fragments. All the fragment ions are then reaccelerated in the LIFT cell. The precursor ions (still highly abundant) are then deflected through the post LIFT metastable ion suppression (PLMS). (Figure modified from Bruker Daltonics Ultraflex II Manual)*

The use of reflector in addition to the classical linear TOF setting was first introduced in 1973 by Mamyryn et al.<sup>377</sup>. Here, a reflector made up of a set of electrodes of variable electric potential, opposite to that of acceleration potential, is utilized. Ions with the same  $m/z$ , but different  $E_{KE}$  penetrate into the reflector to a varying degree. Higher  $E_{KE}$  ions, penetrate deeper, and thereby have an increased flight path, compared to ions of lower  $E_{KE}$ . This results in compensation for the initial velocity spread, and refocusing of all ions for a given  $m/z$  value before they hit the detector.

In comparison to delayed extraction, a reflector is mass independent so the optimal settings apply across the entire mass range. At the same time, it does result in a loss of sensitivity, particularly for larger molecular species. This is associated with a longer flight path, as well as insource or post source molecular fragmentation. This loss of sensitivity is not the case in linear mode as the molecular fragments will arrive at the detector at the same time as the intact species. For smaller molecules on the other hand, the reflector is actually more sensitive, as the time focusing lowers the time spread of ions, resulting in the generation of narrower and thus higher peaks (for a given number of ions).

Theoretically a TOF analyser does not have any limit in mass range (neither low nor high), however the detection capabilities generally decrease as mass range increases. This is largely dependent on the type of detector employed (typically microchannel plate, MCP) and of course the mode of operation (linear, respective reflector). However, other factors such as broadening of the peaks with increased mass, increased isotopic spread, adduct formation and the above mentioned fragmentation sets the practical maximum mass range. At the low range, the practical limitation is generally associated with interference from the matrix generated signal.

#### **3.4.1.4 NanoSIMS**

NanoSIMS (e.g. Cameca NanoSIMS 50 or 50L) is a special case of SIMS, used for nanoscale analysis. It is a scanning ion microprobe that operates in dynamic SIMS mode, while using a continuous primary ion beam, and relies on the use of magnetic sector mass analyser (rather than TOF analyser in conventional SIMS). NanoSIMS is able to obtain significantly higher secondary ion yield than conventional SIMS. It offers high mass resolution, high transmission, and high sensitivity, making it perfectly suitable for precision measurements of majority of the periodic table elements at a subcellular scale (down to 40nm, reviewed in detail in <sup>373,378</sup>).

The use of dual focusing magnetic sector analyser (electrostatic and magnetic, described below), yields a mass resolution of several thousands ( $M/\Delta M$ ). This is sufficient to resolve isobaric interference, particularly for low atomic number

elements, making it suitable for isotopic labelling experiments in biological settings (such as e.g. stable isotopic labelling, described later).

The key feature separating NanoSIMS from conventional SIMS instruments which use TOF mass analysers (TOF-SIMS) lies in the co-axial optics configuration. Here the primary ion beam forming optics and the secondary ion beam extraction optics are co-linear, and can be placed very close to one another, and perpendicularly to the sample being analysed (ca 400 $\mu$ m). This allows for the generation of a small and strong primary ion beam, and hence an increase of lateral resolution (for IMS). At the same time, this does not only reduce the broadening of secondary ion beam caused by angular differences and the energy spread of extracted ions, but also enables higher extraction efficiency of the energetically spread ions (almost all secondary ions generated are collected). This co-axial design however imposes certain constraints. Here the primary and secondary ions have to carry opposite charges (and be of the same energy).

NanoSIMS typically employs a caesium ( $\text{Cs}^+$ ) primary ion beam for negative mode analysis. This beam can be focused down to 50nm, has a high sputtering efficiency, and gives a high yield of elements such as carbon (C), oxygen (O) or sulfur (S). However, an oxygen duoplasmatron that generates both positively ( $\text{O}^+$ ,  $\text{O}^{2+}$ ) and negatively ( $\text{O}^-$ ,  $\text{O}^{2-}$ ) charged species can also be used as a primary ion source. These are then selected for analysis of electronegative elements ( $\text{O}^{2+}$ ) or electronegative elements ( $\text{O}^-$ ). The extent to which these can be focused is however much more limited, as compared to caesium source (down to ca 150nm). Further, the duoplasmatron is less sensitive for analysis of electronegative elements than caesium source. In order to achieve a higher primary ion beam focus radio frequency (RF), an oxygen ( $\text{O}^-$ ) source has been developed. This source can be focused down to 40nm, offering similar sensitivity for the electropositive elements as caesium source for electronegative<sup>373</sup>.

Due to the use of magnetic sector mass analyser, NanoSIMS does not scan masses (as done in TOF), instead several electron multiplier (EM) detectors and faraday cups (FC) are used that yield an increased sensitivity. The currently produced instruments employ

six movable and one stationary EM/FC combination. This usually allows for the detection of up to seven species at the same time, with the mass range of approximately 20 fold, allowing for the detection for multiple isotopes of a single element up to  $m/z$  58 (iron, Fe). This is however often sufficient for use in biological setting. As NanoSIMS relies on the use of high energy primary ion beams, the majority of detected ions are either monoatomic or diatomic. In terms of biological samples, this implies that biomolecules are highly fragmented. Therefore, rather than execute the analysis of individual molecular species, analysis (mainly IMS) based on stable isotopic labelling is performed (described below).

#### 3.4.1.5 Sector field detector

The first high-resolution magnetic sector instrument was introduced in the 1936s by Mattauch and Herzog<sup>379</sup>. However, Thomson and later Dempster had already begun working on such a separation approach in the early 1900s<sup>380,381</sup>. As suggested by the name, magnetic sector instruments use a magnetic sector (sometimes in combination with a static electric sector) to focus the direction and velocity of the ion beam<sup>355</sup>.

In detail, similarly to TOF instruments after ionization, ions are accelerated before they enter the magnetic sector mass analyser. Once in the analyser, they are exposed to a homogenous magnetic field that is perpendicular to their flight path. This will force the ions into a circular motion (the radius of which depends on magnetic field strength), without changing the velocity of individual ions. Again, after leaving the acceleration region, the potential energy of the ions is converted to the kinetic energy (Equation I).

$$E_{KE} = zU = \frac{1}{2}mv^2 \quad (I)$$

In the magnetic sector mass analyser, only ions of mass-to-charge ratio whose centripetal (inwards) and centrifugal (outwards) forces are equal will be able to pass. This is where the centrifugal force ( $\frac{mv^2}{r}$ ) is equal force exerted by the magnetic field on the moving charge ( $zvB$ ) (equation II). After solving the equation I for the velocity ( $v$ ) of the ions, substituting the velocity ( $v$ ) into the equations II, and rearranging this equation, this shows that the  $m/z$  value of an ion analysed in a magnetic sector can be

calculated based on the strength of the magnetic field ( $B$ ), radius of the path produced by the field ( $r$ ) and the acceleration potential ( $U$ ) (equation III). It is clear from the equations III that the  $m/z$  in the magnetic sector does not depend on the velocity ( $v$ ) of the ions. By rearranging equation III, the radius of arc of the ions deflected by the magnetic sector can be obtained (equation IV).

In the magnetic sector mass analyser, only ions of mass-to-charge ratio whose centripetal (inwards) and centrifugal (outwards) forces are equal will be able to pass. This is where the centrifugal force ( $\frac{mv^2}{r}$ ) is equal force exerted by the magnetic field on the moving charge ( $zvB$ ) (equation II). After solving the equation I for the velocity ( $v$ ) of the ions, substituting the velocity ( $v$ ) into the equations II, and rearranging this equation, this shows that the  $m/z$  value of an ion analysed in a magnetic sector can be calculated based on the strength of the magnetic field ( $B$ ), radius of the path produced by the field ( $r$ ) and the acceleration potential ( $U$ ) (equation III). It is clear from the equations III that the  $m/z$  in the magnetic sector does not depend on the velocity ( $v$ ) of the ions. By rearranging equation III, the radius of arc of the ions deflected by the magnetic sector can be obtained (equation IV).

$$\frac{mv^2}{r} = zvB \quad (\text{II})$$

$$\frac{m}{z} = \frac{B^2 r^2}{2U} \quad (\text{III})$$

$$r = \frac{1}{B} \sqrt{\frac{2Um}{z}} \quad (\text{IV})$$

Further, even though the magnetic sector does act as a focusing lens for the ions (equation IV), these will not be focused at the same point if their initial energy (and hence velocity) varies. Therefore the resolution of a magnetic sector analysed is negatively affected by the spread in initial energy of the ions. In order to correct for this, magnetic sectors instruments often also incorporate an electric sector.

Electric sectors (also known as electro static analyser, ESA) consists of two curved plates, which likewise the magnetic sector, apply a force on the ions that is perpendicular to their flight path. This bend the ion beam to a lesser or greater extent depending on the kinetic energy spread of the ions. The ability of the electric sector to focus ions, can again be expressed in terms of centrifugal force and now the force exerted of the moving ions in the electric field ( $zE$ ) (equation V).

$$\frac{mv^2}{r} = zE \quad (\text{V})$$

Again, after solving the equation I for the velocity ( $v$ ) of the ions, substituting it into the equation V, and rearranging this equation, it becomes clear that the focusing of ions by the electric sector (equation VI), is independent of mass or charge, but varies only with the strength of the accelerating potential ( $U$ ) and the electric potential of the electric sector ( $E$ ).

$$r = \frac{2U}{E} \quad (\text{VI})$$

This makes the electric sector a great focusing device, which improves the mass resolution of the magnetic sector (reducing initial energy spread). It cannot however be used independently as a mass analyser. The combined setup can be made in both directions, with either electric sector being first (forward instrument geometry), or the opposite (reverse geometry).

Magnetic sector mass analysers are commonly used in either the magnetic scan mode or voltage scan mode. The choice between these will influence the mass resolving power and mass accuracy of the measurement.

The magnetic scan mode implies that the acceleration potential and the electric sector potential are kept constant, while the magnet is scanned. In this operational mode, a wide range of  $m/z$  values can be covered. Here, the sensitivity of the instrument is independent of the  $m/z$ , however due to the magnetic reluctance, the sensitivity in general will be relatively “suboptimal”. However, it can be improved by either



changing the magnetic field in steps instead of scanning or by using an array detector, for example.

The use of an array detector potentially offers the possibility to use a magnetic sector instrument with a pulsed ion source. However, the mass range of such a setup would be highly limited. Therefore, in general magnetic sectors instruments are used with continuous ion sources.

The voltage scanning mode implies that the magnetic field is kept constant while the acceleration voltage is changed (with the electric sector potential being coupled). In this mode of operation, the  $m/z$  values and the accelerating voltage have a linear relationship. Operating in this mode also typically yields higher mass accuracy. At the same time, however, it has the disadvantage that the sensitivity of the analysis is proportional to the  $m/z$ .

An extension to this operation mode is the peak-matching mode, where both the electric sector and acceleration voltages are varied (they are not coupled). This mode typically yields both the best mass accuracy and optimal resolving power. It is particularly useful when trying to separate two ions which both possess an  $m/z$  that is very close to one another. The scan is however limited to a small  $m/z$  range.

In general, mass resolution and sensitivity are mutually limiting in a magnetic sector instrument. The optimal ion transmission and thereby sensitivity, is typically obtained at the maximum working acceleration potential. This however, limits the obtainable mass range for the analysis. At the same time, the mass resolution in a magnetic sector instrument is determined by the slit width that is present before the detector. Smaller slit width implies a higher mass resolution, however it also implies lower ion transmission.

### 3.4.2 Imaging mass spectrometry (IMS) – molecular histology

Imaging mass spectrometry (IMS) is a broad term used to describe several mass spectrometry techniques that can be used to generate molecular images of analyte distributions across a sample. Unlike other biochemical imaging techniques, such as e.g. immunohistochemistry, IMS enables label-free analysis without any prior knowledge of the potential target species<sup>382</sup>. Still, one can tailor sample preparation in such way to facilitate detection of different classes of target molecular species (e.g. choice of matrix as described above).

The most common IMS techniques are based on either matrix-assisted laser desorption ionization (MALDI), secondary ion mass spectrometry (SIMS) or desorption electrospray ionization (DESI)<sup>382,383</sup>. Recently, a special case of SIMS, nanoscale SIMS (NanoSIMS) based IMS has gained popularity<sup>373,382</sup>. Here, DESI, which was not previously described, is based on focusing an electrospray on the sample surface. This is done at atmospheric pressure. Below, exploration of these techniques will focus primarily on MALDI and SIMS (and NanoSIMS) based IMS.

IMS data acquisition based on both MALDI and SIMS is typically done in so-called microprobe mode. Here, a sample that has been placed on a target surface is scanned in a pre-defined raster pattern (or array) using either a laser (MALDI), or an ion beam (SIMS) (see ionization techniques above). The majority of IMS bio analyses performed with MALDI-TOF and TOF-SIMS are acquired using a discontinuous microprobe. In contrast, microprobes in NanoSIMS are typically operated in a continuous fashion. The images are then constructed pixel-by-pixel by mapping the intensity of an individual ion signal ( $m/z$ ; relative intensity), obtained through acquisition of a spectrum for every x-and y-coordinate.

In principle, IMS could also be performed as ion microscopy, where a wide field of view is desorbed by an unfocused source, followed by the transfer and visualization of the desorbed ions using electromagnetic lenses. Indeed, efforts have been made to enable IMS analysis in microscope mode, both for MALDI, and SIMS. While having the advantage of the spatial resolution independent of the ionization probe, the

microscopy approach suffers several disadvantages, these being primarily the mass accuracy and mass precision due to the restricted choice of detectors (microchannel plates).

Just as any conventional MS technique, the aforementioned IMS techniques have their complementary strengths and limitations, which concern mass accuracy, mass resolution, mass range, chemical specificity and selectivity. Further, in terms of IMS, these also differ in terms of spatial resolution.

Spatial resolution in an IMS experiment based on a discontinuous microprobe is often used interchangeably with the pixel resolution. Here, it is defined as the distance between adjacent pixels for which the intensity distribution data is obtained. Definition of spatial resolution gets complicated when an acquisition relies on oversampling, and the pixel resolution is smaller than the size of the probe.

In principle, for a discontinuous probe, spatial resolution should correspond to the size of the probe, and the distance between two beam impact points, which can be “resolved” (where signal can be acquired) without interference of the adjacent spot. For a continuous probe, the resolution will depend on the frequency of the probe, and the velocity of stage (or beam movement). In either of the cases, the true resolution will depend more or less on the sample preparation, which might in fact influence the analyte distribution (e.g. by diffusion particularly during MALDI matrix application).

MALDI analysis typically affords a lateral resolution of 1-10 $\mu$ m, while SIMS allows for imaging at 50-100nm spatial resolution. Improvement in lateral resolution, generally results in lower sensitivity for both IMS techniques. The choice of ionization technique for biological analysis is often limited not by the spatial resolution but rather the class and size of the analyte. While both MALDI and SIMS can be operated with a TOF detector, which in principle has unlimited mass range, the actual mass range (and hence target analytes that can be detected) are limited by the ionization techniques themselves. SIMS based ionization results in much higher fragmentation than MALDI (see ionization techniques for more detail).

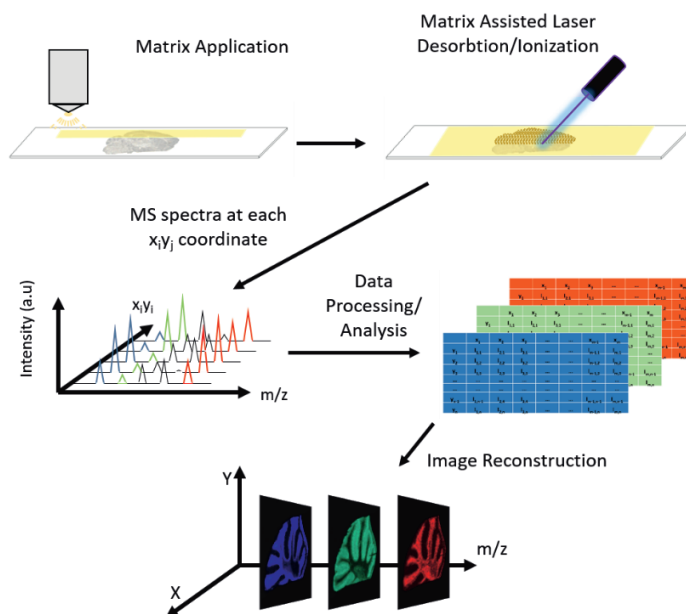


Figure 6. Schematic with main steps of a typical MALDI IMS experiment. Samples mounted on conductive target plate/glass slide are pre-coated with a matrix. The sample surface is then scanned in a systematic fashion with a laser probe, with one mass spectrum being acquired for respective coordinates. Following data processing, analysis single ion images are reconstructed. These map the relative intensity of individual ion signal over the entire analysed sample surface. Adapted from Michno *et al. J Neurochem* 2018, Figure 1<sup>384</sup>.

Both MALDI and SIMS analysis can result in the generation of tremendous amounts of data (NanoSIMS files are generally smaller due to only selected few masses). The size of the files will depend on the spatial resolution of the analysis, the number of pixels, and the sampling rate of the instrument. While just a few years ago, the size of typical data from a TOF based instrument resulted in files “only” a few gigabytes in size, the improvements in probe focusing, acquisition speed, as well as employment of high resolution analyser such as Fourier transform ion cyclotron resonance (FT-ICR), have driven the size of generated datasets to tens, or even hundreds of gigabytes. This poses significant challenges to computing power of acquisition and data analysis computers. Therefore, often a compromise needs to be made with regard to acquisition parameters for an analysis. As this is often suboptimal, new approaches for external data acquisition system and advanced data processing are constantly developed <sup>385</sup>.

Given that the IMS data can comprise hundreds of variables, data analysis of IMS data is typically performed using multivariate analysis (MVA). There are several different multivariate analysis approaches (described later), with common ones including principal component analysis (PCA) or partial least squares discriminant analysis (PLS-DA). These methods represent excellent tools for unbiased data interrogation, which often help reveal anatomical, or disease characteristic regions, based on histology associated chemical changes (mass peaks). Still, although highly useful, the person performing the analysis needs to be able to differentiate the true histological features and chemical changes, from sample preparation artefacts.

#### **3.4.2.1 MALDI imaging MS**

Application of MALDI for spatial profiling, therefore referred to as MALDI imaging MS, was first introduced by Caprioli et al. in 1997<sup>386</sup>. Since then it has been shown to be well-suited for imaging of both large biomolecules such as proteins, peptides, and glycolipids, as well as small ones, including metabolites, neurotransmitters, and in the context of pharmaceutical work, particularly drugs.

However, resembling conventional on target MALDI analysis, mass resolution for larger intact molecules (large proteins) is limited due to the use of a linear detector (rather than reflector mode). On the other hand, matrix clusters typically interfere with the detection of small molecules. Both of these challenges have been addressed to some extent through the development of sample preparation methods, including on tissue tryptic digestion for large proteins, or the use of, for instance, stable isotope modified matrices, together with MS/MS methodologies, and high resolution analysers (e.g. FT-ICR).

As mentioned above, the spatial resolution in MALDI is not only dependent on the laser beam focus but also on sample preparation, including matrix crystal size and lateral diffusion of analyte molecules. While the majority of the matrices used for non-IMS based MALDI can be also be used for IMS (see Table 1), IMS application, these matrices need to be homogeneously deposited on the sample surface. This can be challenging, and often requires an extensive optimization. Some matrices also produce

generally larger crystals than others. Further, given the relatively long IMS analysis, as compared to a simple target analysis, one needs to consider the relative vacuum stability of the matrix in the context of the IMS acquisition time.

MALDI IMS sample preparation generally begins with sample collection. Here, both chemically fixed tissue, such as formalin-fixed paraffin-embedded (FFPA), and frozen tissue is used (preferred). While fixed tissue offers the possibility of simple long-term storage, and therefore access to large amounts of tissue stored in biobanks, its use for MS analysis is limited due to the MS interference caused by the polymeric fixation and embedding agents. Still, there are possibilities to overcome these challenges previously demonstrated, for example through the exclusion of paraffin embedding for lipid IMS (still formalin fixation), dewaxing for metabolite IMS, or complementation of conventional dewaxing, rehydration and antigen retrieval, with tryptic digestion for peptide analysis.

Frozen tissue, being the to-go standard for IMS, is typically prepared by submersion of freshly dissected tissue in liquid nitrogen (or dry ice), an approach referred to as “snap-freezing” or “flash-freezing”. It is performed within 3-minutes of tissue isolation in order to minimize the protein and peptide degradation by proteases. This rapid freezing, which leads to the direct transition of water from its liquid state into an amorphous solid state, prevents cell wall rupture that would otherwise occur due to ice crystal formation during slow freezing. Therefore, this method of freezing offers, in principle, the most efficient cooling of the tissue by maximizing the interaction with the tissue surface area. Still, the relatively high temperature of the freshly isolated surface might lead to vapour formation directly at the surface, resulting in different freezing rates for different tissue regions. Therefore, liquid nitrogen cooled (or dry ice cooled) isopentane is often used for optimal morphological preservation.

Following isolation, and either chemical fixation or freezing, sectioning of the tissue is typically performed using a cryo-microtome (or occasionally microtome of chemically fixed tissue) operating at approximately -20°C. Here, contact with the cryo-protectant, commonly used in immunohistochemistry (such as optimal cutting

temperature medium, OCT), is generally avoided, as it will introduce impurities into the sample. The cryo-sections are then collected onto either a metal target, or more frequently, onto conductive microscope glasses (Indium tin oxide (ITO) coated glasses), by thaw-mounting. Glasses offer the possibility for subsequent staining, and light microscopy analysis.

If proper care is not taken to ensure the “dryness” of the collected frozen sample before its storage, condensation might occur. This will lead to ice formation and thereby freeze damage of the sample (observable in MALDI IMS data). Condensation will also occur once the tissue is taken out from the freezer. Therefore, given that sample preparations and matrix applications for MALDI IMS are typically performed at room temperature, samples are typically dissected when removed from the cold.

Depending on the target of the MALDI IMS analysis, processing of the sample might be necessary prior to matrix application. This typically involves a series of washes in organic solvents and/or aqueous solutions, and results in an improvement of the quality of the signal and removal of interfering components. Given that the majority of the organic solvents can dissolve lipids, these are generally not used prior to lipid imaging. Instead, use of simple aqueous washes, for instance using ammonium acetate, has been reported for the purpose of sample desalting. Up until now, however, the majority of lipid IMS studies are performed without any prior sample clean-up.

In comparison to lipid imaging, analysis of proteins, peptides and drugs with IMS typically requires several washing steps in order to remove lipids and salts that otherwise would cause signal interference. These are pH optimized and often involve washes with gradient alcohol, shown to yield significant improvements in quality of target protein/peptide, respective drug signals.

Finally, the matrix is deposited on the sample. Here, common approaches include either spraying the matrix, or sublimating it. Regardless of the approach applied, matrix that is deposited on the sample has to be highly homogenous. This homogeneity ensures that the detected signal difference corresponds to the accurate molecular content of the sample, and is not an artefact associated with matrix distribution.

Furthermore, the approach used needs to maximize the analyte extraction and incorporation into the crystal, while minimizing analyte delocalization that can occur during these processes as a result of solvation (and diffusion) caused by the used solvent.

Spraying of the matrix onto the samples is most commonly done using automated-sprayers. Commercial nebulizers, such as TM sprayer (HTX, Technologies Carrboro, NC, USA) or SunCollect (Sunchrome, Napa, CA, USA), and even open-access instruments, such as iMatrixSpray are becoming more and more popular<sup>387</sup>. These instruments move across the sample at a constant speed while consistently nebulizing the matrix solution. Adjusting various parameters of the sprayers, including e.g. the flowrate, movement velocity, drying gas flow or spacing between passes, as well as choosing the appropriate matrix solvent composition, can be used to influence the “wetness” of the spray and the crystallization. These adjustments can be particularly useful when trying to perform on-tissue digestion.

These instruments offer a high degree of reproducibility, and when optimized properly also homogeneity of the deposited matrix. Still, while potentially highly robust, matrix spraying using automated nebulizers is limited in terms of how small the individual matrix crystals, can be obtained. Further, in order to ensure the homogeneity in deposited matrix as well as sufficient thickness, numerous passes across the tissue must be performed. This can be time consuming.

One technique developed to overcome these limitations is matrix sublimation<sup>388</sup>. Using this technique, many matrix compounds can be sublimated without decomposing and their vapour is then deposited directly onto the tissue through condensation. This solvent-free matrix deposition method results in an even layer of fine crystals (and hence theoretically superior resolution). It is particularly useful for lipid imaging, however sublimation followed by recrystallization has also been used for high spatial resolution protein imaging<sup>389</sup>.

A neat comparison of two automated sprayers (TM sprayer and SunCollect) as well as sublimation, in terms of throughput, reproducibility, sensitivity, and degree of



spatial detail, and their application for high throughput IMS in clinical context has recently been performed<sup>390</sup>. While sublimation was shown to result in simple overall improvement in IMS data quality, sprayers with the wide variety of adjustable settings offer better opportunity for fine-tuning the analysis towards the target molecules (e.g. by changing the solvent system, adjusting wetness and hence extraction).

Solvent systems for the MALDI matrix solutions need to be adjusted depending on the properties of the matrix used and the analytes of interest. These adjustments will affect the solubility of the matrix, the analyte extraction properties of the matrix-solvent solution, and, importantly, the size of matrix crystals generated and the efficiency with which the matrix will aid in ionization of the analytes. This optimization is crucial for both the spatial resolution and signal intensity. A typical matrix solvent system consists of water and a water-miscible organic solvent (e.g. methanol or ethanol). This solvent system is adjusted with acid(s) or base(s) (e.g. formic acid (FA) or tri-fluoro acetic acid (TFA) and ammonium-bicarbonate (Ambic)) to an optimal pH, which can yield both an improved solubility of the matrix, but also an increased extraction and ionization of the analyte.

In general, dryer solvent systems, for the same sprayer parameters, will result in lesser extraction. Such dry solvent system will be better for resolution, but generally it will also be less suitable for IMS of larger molecules, such as proteins as these typically require more extensive dissolution. Still, the limited dissolution with dry solvent system has been to some extent overcome by the earlier mentioned recrystallization of the relatively dry-deposited matrix, through its solvent based dissolution directly on sample surface.

#### **3.4.2.2 SIMS and NanoSIMS imaging**

Imaging through conventional SIMS (TOF-SIMS) and NanoSIMS is similar to MALDI, with the exception that generally, no matrix compound is used. Still, matrices have been used to enhance the signal intensity for a wide range of analytes in so-called matrix enhanced-SIMS (ME-SIMS)<sup>370-372</sup>.

For the conventional SIMS, minimal processing (such as washes etc.) is needed, and the samples can be theoretically mounted on any kind of surface (typically a glass slide or silica wafer to ensure flatness of the surface). Yet, given the inherited high surface sensitivity of the technique, both in terms of the topology and the surface contaminants (which might cause ion suppression), one needs to ensure superior sample quality and means of its collection and deposition on the target.

A sample for SIMS analysis needs to withstand very high vacuum. Therefore the samples have to either be dry (either with or without fixative), or be present in a frozen hydrated state. These samples are then cut on a microtome/ultramicrotome (or their cryo equivalent for frozen hydrated samples) to a thickness ranging between 12µm and 400nm. Following sectioning, the frozen hydrated samples, can be kept in such a state by performing the analysis in cryo conditions, while keeping the sample at around -120°C. This approach, even though rarely used, is particularly applicable in the analysis of the life-like state of individual cells.

An alternative to the frozen hydrated state is high pressure freezing followed by freeze-fracturing the sample. This offers a high degree of morphological preservation, and ideal spatial preservation of subcellular water, salts and lipids. However, due to the unpredictable cracking pattern, topographical artefacts might be introduced.

For NanoSIMS imaging, additional tissue processing is generally needed. Here, the flatness of the surface is even more important than in the case of conventional TOF-SIMS imaging. Therefore, most often electron microscopy preparation, comprising chemical fixation and embedding (described earlier), is used. These preparations are optimized for the preservation of macromolecules, particularly proteins through their crosslinking. As a result the majority of water-soluble species, in particular physiologically relevant metal ions (e.g.  $Zn^{2+}$ ,  $Cu^{2+}$ ,  $Ca^{2+}$  etc.), are either lost or delocalized due to diffusion. While cryogenic approaches, such as freeze substitution, improve both tissue morphology, and to some extent, preservation of such species, true maintenance of their physiological localization and concentrations is practically

possible only if the samples were to be analysed in cryo conditions (e.g. high pressure freezing or freeze-fracture).

As described earlier, the practical mass range of a NanoSIMS analysis is that of the monoatomic and diatomic species. Therefore, biological studies with NanoSIMS often rely on the use of isotopic labelling, for instance with  $^2\text{H}$ ,  $^{13}\text{C}$ ,  $^{15}\text{N}$ ,  $^{18}\text{O}$ . Even though these can theoretically be well maintained within the sample, a significant decrease in their actual signal can be caused by the introduction of background during the sample preparation procedures (e.g. conventional fixation and embedding media might contain large amounts of  $^{13}\text{C}$  but also common isotopes such as  $^{19}\text{F}$ ). Therefore, appropriate controls need to be used. Still, when proper caution is taken, the NanoSIMS analysis, including multi-isotope imaging mass spectrometer (MIMS), where sample labelling with both  $^{13}\text{C}$  and  $^{15}\text{N}$  (e.g. through SILAC, described below) at the same time is performed, is possible due to the superior mass resolution of the instrument<sup>391</sup>.

Samples for NanoSIMS analysis are generally prepared on an ultramicrotome to a thickness on an order of a few hundreds of nanometres (typically around 400nm). While this thickness ensures sufficient sample thickness for the analysis, it compromises the quality of the transmission electron microscopy (TEM) images that are usually obtained from consecutive sections. Therefore, switching between semi-thin (e.g. 400nm) and ultra-thin (e.g. 70nm) sections is often performed in order to enable co-registration of NanoSIMS data to TEM data.

In general, NanoSIMS samples should be mounted on a conductive surface, due to the high degree of surface charging that takes place during analysis (even with charge neutralization during the analysis). Therefore, silicon wafer, conductive coverslips, and even Indium tin oxide (ITO)-coated glass slides (like in MALDI) are used. The latter's transparency provides the possibility to perform correlative microscopy. Alternatively, transmission electron microscopy (TEM) grids are often used. This technique is particularly useful when TEM ultra-thin sections are collected at the same time. In some cases, coating of the substrate is needed in order to ensure sample adhesion (e.g. glass slides/wafers) or to stabilize the sample (e.g. TEM grids). This

process is typically done with poly-L-lysine, respective formvar or carbon film (other films are also available), that are highly transparent to electrons.

Finally, in order to further compensate for the surface charging, NanoSIMS samples are often conductively coated (typically using Au, C or Pd atoms). This coating is done either by a sputter coater or evaporator depending on the choice of coating. The thickness of such coating layer is generally on the order of a few nanometres (e.g. 10-20nm).

### **3.4.3 Stable isotope labelling with amino acids**

Stable Isotope labelling with amino acids in cell cultures (SILAC), or of mammals (SILAM), are analytical approaches to interrogate reactions, metabolic pathways, physiological and recently even pathophysiological processes in cell and mammillary tissue<sup>392-394</sup>. In comparison to other approaches used to monitor synthesis, turnover, clearance or transport, this approach does not introduce any tags that might interfere with native structure or function of the protein.

SILAC/SILAM instead relies on the introduction of fractionally heavier, non-radioactive isotopes of natural elements (e.g.  $^{13}\text{C}$ ,  $^{15}\text{N}$ ,  $^2\text{H}$ ) into the amino acid structure that is supplemented as the growth media/feeding diet to the cells/animal. These amino acids become incorporated into the newly synthesized proteins, and participate in exactly the same reactions and processes as the endogenous ones. Heavier isotopes such as these are naturally abundant, however only in relatively low amounts ( $^{13}\text{C}$ -1.109%;  $^{15}\text{N}$ -0.364%;  $^2\text{H}$ -0.012%). Still, this natural abundance needs to be accounted for as potential background during the analysis. Assessment of the stable isotope incorporation is typically done through mass spectrometer (MS) based quantitative proteomics.

SILAC experiments generally rely on differentially labelled cell cultures. Here, one batch of cells is grown on the natural (light) amino acids, while the second one is grown on stable isotope labelled (heavy) amino acids. Commonly one introduces only isotope labels to specific amino acids (e.g.  $^{15}\text{N}_2^{13}\text{C}_6$ -lysine and  $^{15}\text{N}_4^{13}\text{C}_6$ -arginine) which, in stark contrast to general nitrogen or carbon labelling, creates distinct mass shifts that

can easily be calculated. Upon mixing, possible purification, digestion (typically with trypsin) and MS analysis, this amino acid specific labelling allows for an easy, and accurate interpretation as well as the quantification of the heavy to light peptide ratio. Such quantification is possible thanks to the fact that the heavy and light peptides will co-elute due to their identical chemical properties. In the case of complete nitrogen or carbon labelling, such analysis is not as straight forward as different amino acids are incorporated at different rates. Still, work around approaches to address the issues associated with general labelling have been developed. Modelling the isotope incorporation and fitting it into the individual isotope envelopes can be done.

Working with individual amino acids also has its drawbacks. In terms of general challenges, possible metabolic conversions of amino acids, such as arginine to proline, might cause inaccuracies in terms of quantification when compared to peptide signal from non-labelled cell culture<sup>395</sup>. Further, heavy stable isotope labelling of both amino acids, lipid precursors, and even drugs has been used to study cellular localization of these molecules or their metabolites on a single cell level using NanoSIMS or in terms of broader tissue structures MALDI-IMS. Insufficient <sup>15</sup>N or <sup>13</sup>C labelling associated with single amino acid labelling in such cases is more likely to take place, as compared to general nitrogen or carbon labelling. Therefore, if not compromising the aim of the experiment, a general nitrogen or carbon might be more suitable for these experiments.

Generally, the stable isotopic labelling experiments rely on the full incorporation of amino acids into protein structures in either cells or mammals. While in cells, one generation is typically sufficient to replace the entire proteome, advanced organisms require labelling for several generations (at least 2 generations for mice). In order to address the limitation associated with such multigenerational labelling, two alternative SILAC approaches have been developed. The use of SILAC as a “spike in” standard, where SILAC standard is produced separately and spiked in for the analysis itself; and a “pulsed” approach, where the labelled amino acids are added to the grown media (cells) or replaced in protein diet (mammals) for a shorter period of time<sup>396,397</sup>.

The “spike-in” approach allows for the preparation of the sample of interest without any restriction potentially imposed by the SILAC. The peptide ratios between the sample (light) and the SILAC standard (heavy) is determined<sup>396</sup>. The “pulsed” approach, on the other hand, allows for monitoring of the *de novo* protein production rather than simply quantifying the relative amounts of heavy to light peptide for the purpose of their quantification<sup>397</sup>.

Finally, the number of isotopes available limits the degree of multiplexing in stable isotope labelling experiments. Recently, the introduction of neutron encoding, that is an increase in possible mass defects based on the addition of extra neutrons, has been developed (NeuCode)<sup>398,399</sup>. This new approach is compatible with existing labelled amino acids used for SILAC, and expands the possible level of multiplexing<sup>398</sup>. The extremely small mass differences however need to be resolved on a high resolution mass spectrometer<sup>398,399</sup>.

#### **3.4.4 Laser microdissection**

Laser microdissection refers to the isolation/dissection of microscopic objects of interest with the help of laser. Using this method, subpopulations of cells or morphological features can be collected directly during the visualization in a microscope. This non-contact sampling approach provides an indispensable tool for downstream genomics and proteomics, allowing for the bimolecular analysis of the extracted object in their physiological context.

During the procedure, a laser is moved along a pre-defined pattern in order to cut out the feature of interest in the specimen, which has previously been mounted on a thin membrane (to aid the transport). Following cutting, transport of the dissected element is typically performed in either of the following fashions: in an upright microscope simply with the help of gravity (as the glass/dish is facing downwards), or in an inverted microscope with the help of laser microdissection pressure catapulting (LMPC). In the LMPC setup, a laser pulse is used to transport the cut specimen. The cut out specimen is collected either directly into a tube (in upright setup), or into an adhesive cup when an inverted microscope is used.

## 3.5 Immuno-based analysis

### 3.5.1 Immunoprecipitation

Immunoprecipitation (IP) is an antibody based affinity purification method<sup>400-403</sup>. The aim of IP is typically to isolate the proteins or peptide of interest for further semi-quantitative or quantitative analysis, using western blot or MS. This approach can, for example, be used to study structure or modifications of a protein/peptide, but also to investigate the interactions of this protein/peptide (as primary IP target) with other proteins/peptides.

When the target antigen of the IP is used to co-precipitate its own binding targets, this is referred to as co-IP. For instance, IP can be used to study the interactions between proteins and DNA (known as chromatin IP (ChIP)) or RNA (known as RNA IP (RIP)). Here the DNA (or RNA) are temporarily cross-linked with the proteins, cells are lysed, the IP target proteins are precipitated, the DNA (or RNA) is removed by digestion usually using proteinase K, purified and sequenced (typically through quantitative polymerase chain reaction (qPCR)).

IP can generally be performed in two ways. Either through pre-immobilization, where the antibody is first immobilized to the support bead before interacting with the target (Figure 4), or by the free antibody approach, where interaction with the target is done prior to interaction with the support bead. While the pre-immobilization approach is most common, the free antibody approach generally works better if the target is present at very low concentrations, if the binding between the antibody and the target is weak, or if the binding kinetics is slow. Once the IP target-antibody-bead complex is generated, it is washed (sometimes cross-linking is preformed beforehand) in order to remove the undesired matrix, and eluted in order to release the affinity purified IP target (e.g. protein or peptide). The performance of an IP depends on multiple factors, these include the choice of beads, choice of antibodies and their concentration, possibly a cross-linking agent, in case of cell lysis also a lysis buffer, as well as the choice of binding, washing and elution buffers. Optimization of the IP is therefore often empirical, and relies on the use of a control to assess the non-specific interactions (if

mass spectrometry as means of detection is used, this process can be much easier controlled).

Two common types of beads include the agarose beads and magnetic beads. These differ primarily in terms of binding capacity and means of separation from the sample. The agarose resin beads are useful for large-scale purification (few mL) as they have to be separated by centrifugation. They are porous, and hence offer a large binding capacity per bead. Magnetic beads have limited binding capacity, as the sites of antibody interactions with the bead are confined only to the surface. These beads are theoretically much smaller than the agarose beads and theoretically display a smaller binding capacity per bead. In practice however, given that the orientation of the antibody is outwards (typically immunoglobulin-binding protein is used), and the magnetic separation is more efficient than centrifugation, the yield can be similar, if not better. Further, the magnetic beads typically offer shorter incubation times, less pre-cleaning of the beads, ease of use (including possible full automation) and multiplexing; making them more reproducible and hence more commonly used approach, especially for small volumes.

Binding of the antibody to the bead can be performed in a multitude of ways. Most commonly, immunoglobulin-binding protein (Ig) coated beads, including protein A (IgA) or G (IgG), are used. These are specific to the heavy chain of the fragment crystallizable (Fc) region of the antibody, allowing for the outwards orientation of the antigen-binding site. Alternatively, streptavidin beads can be used in combination with biotinylated antibodies.

In some cases, antibodies can be chemically bound to the beads by establishing a permanent, covalent binding. This is referred to as direct IP and can be performed for instance by establishing a link with primary amines ( $-NH_2$ ). Given that an antibody displays many surface amines, the antibodies will have a random orientation on the bead in this approach. This random orientation typically does not have any major effect on the antigen binding. The covalently bound antibody-bead complex is very stable and unless a reducing elution is performed, the antibody will not co-elute with the



target antigen. An alternative approach used in the indirect IP to prevent the antibody from eluting with the target, is to covalently bind the antibody to the Ig protein that the bead is coated with. This is done by crosslinking the adjacent amines on the antibody and the Ig protein using cross-linkers such as N-Hydroxysuccinimide esters (NHS). This cross-linking will result in the formation of covalent amide bonds, primarily of the lysine side chains. In both of these cases, the antibody-bead complex can often be reused.

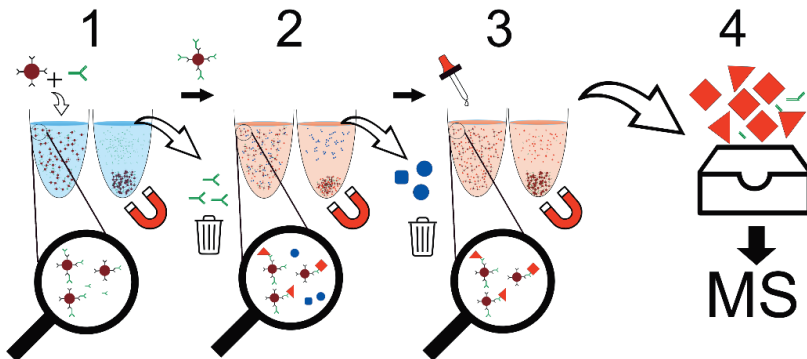


Figure 7. Schematic picture of an IP based on pre-immobilized antibodies and magnetic beads. (1) The immunoglobulin-binding protein (Ig) coated magnetic beads are pre-incubated with epitope specific antibodies. The beads are then pulled down with help of magnet, and the unbound antibodies are washed away. (2) Bead-antibody complex is added to the sample and incubated. Antibodies recognize the target epitopes (red). The bead-antibody-antigen complexes are then pulled down with the help of a magnet, and the rest of the sample constituents are washed away. (3) Elution is performed separating the target antigen (e.g. peptides/proteins) from the beads. (4) Purified target molecules (e.g. peptides with varying amino acid length) are collected and can be analysed using mass spectrometry (MS).

Finally, choice of buffers (lysis, washing, and elution) is crucial to obtain the optimal purification of the target. In the case of lysis buffers, their components often depend on the target antigen, conformation and its location within the cell. Its aim is to maximize the release of the target from the cell and inhibit enzymatic activity that could degrade the target. If the native state of the target is of interest, or if antibody's specificity towards the target depends on its native conformation, the lysis buffer should be non-denaturing. Here typically non-ionic detergents (such as Triton X-100) are used. If denaturation is desired or needed, as is often the case with nuclear proteins,

denaturing buffers containing ionic detergents (such as sodium dodecyl sulfate, SDS) are used. If mechanical homogenization of the sample is used or release of the target is performed with the help of heat, detergents are often omitted, and protease inhibition and agents protecting against oxidative damage are used. Here protease inhibitor cocktails and EDTA are often added.

Given that the stability of the antibody-target antigen complex depends on the environment, samples are often washed in ionic strength buffers with nearly neutral pH, which stabilize these complexes (typically phosphate-buffered saline (PBS), with small amount of detergent). This aids in the removal of non-specifically bound antibody complexes, undesired matrix components, and in some cases, also the lysis buffer itself, if such was used. Efficiency of this process will affect the purity of the elution.

Finally, the choice of elution buffer depends on the type of downstream analysis. If one plans to perform SDS-PAGE separation, elution with the SDS-PAGE buffer is the natural choice. This buffer is very effective at dissociating the antigen from the antibody, however it also results in the denaturation and reduction of the protein, and contamination of the sample with the antibody. It is therefore not easily compatible with other analysis methods, unless removed. A common alternative to SDS-PAGE is the use of low pH, non-denaturation buffers such as 0.1 glycine-HCl. Still, even this buffer can cause denaturation, and also results in elution of the antibody together with the antigen. Therefore, optimization of the elution step often includes a choice of one of many other elution buffers, including others at low pH (e.g. formic acid (FA)), those at high pH (e.g. ammonium hydroxide), or for instance organics.

### **3.5.2 Immunohistochemistry**

Immunohistochemistry (IHC) refers to an antibody-based method for the detection, visualization and localization of specific molecular components (antigens) in their proper cellular/tissue context<sup>402-406</sup>. IHC is often performed both in research, but also in clinical settings. The success of this analysis method depends on good sample quality, sample preparation and proper staining. If these are not properly optimized

and controlled, the staining process might introduce a lot of artefacts, hampering the interpretation of the images.

### **3.5.2.1 Tissue isolation and storage**

When it comes to choosing tissue, the best quality of tissue is usually obtained from biopsies or from animal models. Here, the time of isolation, methods of preservation as well as approaches for long term storage can be easily controlled. On the other hand, autopsies provide tissues that are much more degraded, including both a loss of tissue integrity but also the disappearance of the antigens. When it comes to cells, storage and their preservation can easily be controlled, therefore the biggest challenge lies in the proper means of preserving their integrity during the staining. If the cells are adherent, one should preferably grow the cells directly on the culture plates that are suitable for microscopy. If the cells are in suspension, these need to be carefully adhered to the coverslips.

In order to preserve the morphology and epitopes, both cells and tissue can be either frozen or fixed directly. Freezing can be performed by submerging the sample in liquid nitrogen, or by covering it with the cryo-protective medium (e.g. optimal cutting temperature, OCT) and then freezing. The sectioning is then performed using a cryo-microtome below zero. The actual temperature depends on the tissue, particularly its fat content, but is usually around  $-20^{\circ}\text{C}$ . Post sectioning and prior to staining, tissue sections need to be fixed. This fixation can be done using either aldehydes (e.g. paraformaldehyde (PFA)), or organic solvents (e.g. acetone, ethanol, methanol). Freezing has the great advantage of shorter processing times, and is better for the preservation of sensitive epitopes.

An alternative approach is to directly fix the specimen using chemical fixatives, here a common approach includes formalin fixation paraffin embedding (FFPE), and alternatively PFA is sometimes used (particularly in research setting). Formalin crosslinks the proteins, terminates all cellular processes and immobilizes the cellular components. The major advantage of this approach is the ease of storage and sectioning, both of which can be performed at room temperature. Further, direct

chemical fixation for instance with FFPE offers superior preservation of morphology of the tissue. At the same time, this approach unfortunately adds several preparation steps to the staining procedure.

Broadly, this includes deparaffinization, but often also the reversal of crosslinking and antigen (epitope) retrieval. The latter is might be necessary as the crosslinking with formalin generally masks the epitopes of interest, which in turn obstructs antibody binding. Antigen retrieval is typically done through the treatment of the sample with either proteolytic enzymes (e.g. trypsin or proteinase K) or detergent, or by boiling the sample in a buffer (often citrate buffer, approach referred to as heat-induced epitope retrieval (HIER)), or through a combination of these.

### **3.5.2.2 Antibody based antigen detection**

Immunohistochemistry staining is generally performed using antibodies (either polyclonal or monoclonal), however small antibody fragments, fluorophores, peptides, and affibody molecules can also be used. Polyclonal antibodies, typically derived from serum, represent a mixture of heterogenous antibodies with different, but poorly defined, target epitopes. Because of this mixture, they are very potent, which can be both advantageous, for instance if the antigen is abundant in low concentrations, but also disadvantageous, as they will display relatively high unspecific binding and background.

This stands in contrast to monoclonal antibodies. These, produced in a hybridoma cell line, have well defined target epitopes. Therefore, they are considered much more specific than polyclonal antibodies and typically display less “off-target” binding and background. Still, even their specificity can be limited, especially if they have to detect subtle difference (e.g. single amino acid differences), or if the target antigen is present in very small amounts.

Therefore, regardless of whether polyclonal or monoclonal antibodies are used, IHC requires careful optimization in order to prevent the generation of false positive or false negative results. This includes the titration of the antibodies, choice of appropriate buffers and additives (e.g. detergents to help permeabilization), and optimization of

incubation times. Buffer and additives both help to dilute antibodies and stabilize them, but are also used for rinsing/washing in-between the steps in order to remove unbound or weakly bound unspecific interactions. Further, any kind of IHC experiment requires pre-intubation of the sample with a blocking buffer in order to prevent non-specific binding of the antibody (typically contain few percentages normal serum, and bovine serum albumin (BSA)). No rinsing is done after the blocking.

### **3.5.2.3 Antigen visualization**

Detection of the antibody staining in IHC can be performed either in a direct or indirect fashion. The choice of detection system depends primarily on the expression levels of the target antigen. In a direct detection system the primary antibody is directly conjugated to a reporter (enzyme or fluorophore). In indirect setup, a secondary antibody is raised in a species different than the primary antibody (carrying a reporter), which targets the host species of the primary antibody is used.

The direct system is simpler, both in terms of having fewer steps, as incubation with a secondary antibody is not needed, but also in terms of multiplexing, as combination of many more fluorophores can be used without binding interference (since these are directly conjugated to the antibodies). This setup it more suitable for the detection of highly expressed antigens.

If the antigens are expressed at relatively low levels, the indirect detection system might be more suitable as a signal amplification step is directly incorporated (multiple secondary antibodies can bind a single primary antibody). Further, additional amplification can be done for instance through the incorporation of a biotinylated secondary antibody. Here, either an avidin-biotin-enzyme (Avidin-biotin complex (ABC)), a streptavidin-biotin-enzyme complex (labelled streptavidin-biotin (LSAB)), or an equivalent of such complex conjugated to a fluorophore rather than an enzyme, can be used. When using either ABC or LSAB, however, one needs to take additional precautions and block endogenous biotin present in the tissue (particularly important in frozen tissue).

As mentioned earlier, visualization in IHC is performed either using enzymes or fluorophores. The common enzymes comprise horse radish peroxidase (HRP) and alkaline phosphatase (AP). HRP can precipitate chromogens such as 3,3'-Diaminobenzidine (DAB) and 3-amino-9-ethylcarbazole (AEC), while AP precipitates chromogens such as 5-bromo-4-chloro-3-indolyl phosphate (BCIP) and nitro blue tetrazolium chloride (NBT) into very stable, insoluble, coloured precipitates that can be observed directly in a light microscope. This method of detection is more common for the FFPE tissue.

When it comes to fluorophores there is a wide variety of molecules that can be used for this purpose. These can differ both in excitation and emission wavelength (described above). Fluorophores have the advantage of possible multiplexing, as compared to chromogens. Still, at least when using the secondary antibody conjugated fluorophores, one needs to take into consideration that the secondary antibodies must target different primary antibodies. Further, one needs to consider the emission overlap (discussed above). One large disadvantage of fluorophores as a visualization method is their relative instability, as compared to chromogens. Fluorophores fade with time, and also might be bleached during analysis. Fluorescence visualization is more commonly used for frozen tissue (chemical crosslinking, e.g. PFA can introduce background fluorescence).

Following staining and visualization of the target antigen(s), counterstaining is performed in order to provide additional contrast/information, typically about general sample morphology, primarily by labelling cell nuclei. Common counterstains for light microscopy include for instance haematoxylin and eosin (staining cell nuclei, respective extracellular matrix and cytoplasm) or nuclear fast red (staining nuclear chromatin), and for fluorescence microscopy the 4',6-diamidino-2-phenylindole (DAPI, staining AT region of DNA) or the Hoechst stain (also used to stain DNA). Finally, following counterstaining, the sample is protected for long term storage by mounting it on a coverslip with the help of solvent or water based mounting media. These often include antifade agents to prolong fluorescence.

## 3.6 Multivariate analysis (MVA)

Many chemical analysis techniques, including mass spectrometry and spectroscopy, result in datasets that contain hundreds to thousands of variables. This poses challenges to data evaluation and interpretation since classical univariate statistical analysis approaches are no longer suitable. Therefore, multivariate data analysis (MVA) approaches are used to extract relevant information from large datasets of these chemical analysis.

Two common multivariate projection methods used to analyse MS data are principal component analysis (PCA) and partial least square regression (PLS). These, rather than being based on standard deviation or variance that only operate in a single dimension (assuming independence of variables), rely instead on covariance of variables with one another (which is often the case in these datasets), and projections of the covariance matrices. An alternative approach for data mining in MS is cluster analysis. Here, classification of observations is performed based on the combination of interval variables describing the distance between given observations and the nearest cluster mean.

### 3.6.1 Principal component analysis (PCA)

The principal component analysis (PCA) is one of the most commonly used methods for unsupervised multivariate approach for reducing data dimensionality and creating linearly uncorrelated variables, known as principal components (PC)<sup>407,408</sup>. This is done by extracting the systematic variation in measured variables (in the X-covariance matrix) using eigenvectors. These eigenvectors are non-zero vectors, which under linear transformation only change by a scalar factor (eigenvalues). These are orthogonal to one another, creating a multivariate space based on the linear combination of variable and observation. Their direction describes the largest possible variance. Hence the 1st PC accounts for as much variation in the data as possible, and each successive PC represents the next largest variation that is orthogonal to that represented in the proceeding PC.

Projection of individual observations on these PCs allows one to obtain an overview of how different observations are similar or dissimilar to one another. This overview is typically done by investigating the score plots. Here objects that are close to one another in the plot have similar characteristics. Further, in order to reveal what these characteristics are, one can investigate the loading plots. These represent the relationship between the variables underlying a given PC. In order to aid the interpretation of the PCA, each of the variables should be mean subtracted prior to PCA. This processing will produce a dataset with a mean of zero. Here, the objects that are furthest from the origin are the ones that contribute the most to the PC generated by this model. PCA models are sensitive to scaling.

### **3.6.2 Partial least square (PLS) and orthogonal PLS**

Partial least square regression, or formally known as projections to latent structures (PLS) is a supervised multivariate approach and an extension of multiple regression modelling<sup>408-410</sup>. In contrast to the multiple regression modelling, that relies purely on factors extracted from predictive (X) and observed variables (Y), PLS also performs regression modelling of covariance in these predictive and observed variables (X/Y) and projects these into a new space. The use of both predictive but also observed variables makes PLS different from PCA (which relies purely on modelling of covariance in measured variables, X). Recall that in PCA, the loading vectors are eigenvectors of covariance in X (maximizing the covariance), whereas in PLS they are eigenvectors of covariance in X and Y.

In order to maximize the covariance, PLS divides the sum of squares of X into two parts, the systemic variation and residual. However, the model does not indicate how much of this systemic variability is actually predictive of Y and how much is not (orthogonal variability), i.e. the loading weights express both the predictive and orthogonal variation. Thus, problems can arise when trying to interpret the graphical representation of PLS.

Similarly to the score and the loading plots in PCA, the components in PLS maximize the covariance, in this case including both X and Y. In practice, this makes the



interpretation relatively simple only in the case when  $X$  and  $Y$  overlap, that is when there is a large correlation between  $X$  and  $Y$ . However, when there are large orthogonal components present in  $X$ , i.e. when there is a large variation in  $X$  that is not linearly related to  $Y$ , there will be little overlap with  $Y$ . This lack of overlap will hamper the interpretation of PLS graphical representation, as these plots will be heavily influenced by variation that is not really true for the  $X/Y$  correlation. In short, there is no-direct correspondence between score-loadings in PCA and PLS.

There are multiple extensions to the PLS modelling. One of these is referred to as Orthogonal PLS (OPLS)<sup>411,412</sup>. OPLS, divides the sum of square into three rather than two parts, thereby additionally separating the systematic variation in predictive variables ( $X$ ) into those that are truly correlative (predictive) of the observed variables ( $Y$ ), and those that are uncorrelated (orthogonal) to the observed variables. Through this, OPLS addresses the challenges associated with a simple PLS described above. Overall, this yields a good interpretability where, at least in a single observable variable case ( $Y$ ), the first component in OPLS is equivalent to the first PC in PCA model. Any successive components in OPLS model will reflect the orthogonal variation. This is particularly useful when the observed variability is categorical and discriminant analysis (DA) is used for class-separation. OPLS can be expanded to multiple- $Y$  cases. In that case, there will be more than one predictive OPLS component.

### **3.6.3 Clustering analysis**

Clustering analysis is a general term for iterative processes that are used to partition a data set into two or more mutually exclusive clusters/classes, based on a measure of their similarity/dissimilarity, referred to as “interval variable”<sup>408,413</sup>. There is a wide variety of algorithms that can be used for this purpose, with K-means and hierarchical clustering being common. Further, in context of IMS data a combination of these, referred to as bisecting k-means, is used.

The k-means clustering is a partitional, centroid based clustering approach, which tries to divide the dataset into k-sets simultaneously, based on the similarity/dissimilarity of

the objects. Any given object end up in only one cluster. It does so by finding  $k$  randomly generated cluster centres (that is they may not necessarily be members of the data), and while minimizing the squared distance (“interval variable”) of the object to the clusters, the data is assigned to closest clusters. Upon object assignment, the centroid of a given cluster becomes the new centre. This process is iterative, and continues until convergence. The result is represented in so called Voronoi diagrams.

A large drawback of  $k$ -means clustering is the need to predefine how many  $k$ -clusters the algorithm should find. Furthermore, given that the algorithm optimizes the cluster centres rather than the borders, the objects on the borders might not be optimally defined. The algorithm is also sensitive to the outliers, making these the cluster centres.

The hierarchical clustering analysis (HCA) on the other hand is a connectivity-based algorithm that aims to decompose the data and build a hierarchy of clusters. This decomposition is done under the assumption that objects that are closer to one another in terms of the “interval variable” are more related. The result of HCA is a “parent-child” structure, where the two most similar objects combine together to form a tree-based structure, a dendrogram. In this dendrogram, the objects are placed on the  $x$ -axis, organized in such fashion that the generated clusters don’t mix. The  $y$ -axis on the other hand measures the distance at which the clusters merge together. Any valid measure of distance can be used in this case.

Division into hierarchical clusters can be done either in agglomerative (bottom-up) or divisive (top-down) fashion. In the agglomerative approach, objects are first separated and then merged in a pair-wise fashion forming clusters based on their proximity. This process continues with the assessment of the proximity of newly formed clusters, and moves up in the hierarchy until all objects are merged into one cluster. In the divisive approach, the opposite is true. One cluster is divided into smaller clusters based on the largest distance (smallest similarity between the clusters). This process continues until each cluster is composed of a single object.

Given the limitations associated with both the HCA (required knowledge of distances between all pairs - can be computationally challenging) and the  $k$ -means (required

knowledge of the number of clusters), an approach based on the combination of strong features of both the HCA and k-means has been developed. It is referred to as bisecting k-means (or two step clustering)<sup>413,414</sup>. In this approach, no raw data (as it would in HCA) is used. Instead, all the objects start in a single cluster, which is then separated/bisected into two clusters using the centroid-based approach (k-means). Within each of these clusters, all the object are treated as the same entity. This process is then repeated by splitting one of the formed clusters. At any given point, the cluster's centres, as defined by the k-means algorithm, are discarded. The clusters themselves are, however, retained.

Since role of individual objects in the given clusters is trivial, each subsequent division step decides on either merging subsequent clusters with previous ones, or forming new clusters, purely based on the measure of the distance between clusters and not objects (just like in HCA). In that way, the algorithm builds a random binary tree, similar to the dendrogram in HCA. This aids in the interpretation, simplifies data exploration, and saves computational power (particularly useful in IMS studies where large amounts of data are generated in individual experiments).

## 4 RESULTS AND DISCUSSION

### 4.1 Paper I: Evaluation of MALDI IMS for protein and peptide analysis in AD on single plaque level

Commonly, biochemical characterization of A $\beta$  plaque pathology is typically performed through immunohistochemistry of A $\beta$  deposits, using different anti-A $\beta$  antibodies and histological amyloid probes, such as Congo Red and Thioflavin. While IHC targets specific epitopes, histochemical stains are often used to discriminate between cored and diffuse plaques based on positive staining only of cored deposits. Both methods suffer from limitations, with respect primarily to chemical specificity and throughput, as these do not allow for comprehensive molecular analysis of more than 3-4 target species (such as epitopes) at a time.

Imaging mass spectrometry is a powerful approach for concurrent probing of chemical distribution in complex biological tissue samples<sup>415-417</sup>. In particular, previous proof of principle applications of MALDI imaging MS to AD patients and transgenic APP mouse brain sections demonstrated this technique is well-suited for the detection of A $\beta$  peptide truncation *in situ*<sup>418-420</sup>. Given the proposed brain-region specific variations in A $\beta$  peptides and suggested heterogeneity in A $\beta$  plaques, the aim of the present study was to investigate the applicability of MALDI-IMS to specifically evaluate biochemical microenvironment changes associated with the individual A $\beta$  plaques.

Therefore, we employed MALDI imaging for probing plaque pathology associated peptide and protein distributions in a transgenic APP mice model carrying the Arctic and Swedish mutation of amyloid-beta precursor protein (tgAPP<sub>ArcSwe</sub>). Cryo-sections, collected from fresh frozen mouse brain tissue, were washed and coated with  $\alpha$ -cyano-4-hydroxycinnamic acid (CHCA) matrix using an automated nebulizer sprayer (ImagePrep II) and MALDI IMS was performed at a lateral resolution of 50  $\mu$ m. Following MALDI IMS, multivariate image analysis was used to interrogate the obtained data in order to identify anatomical features as well as the A $\beta$  pathological deposits based on their chemical identity. Spatial Segmentation using bisecting k-means clustering (Figure 8B-D) helped outline cortical and hippocampal regions and

allowed identification of A $\beta$  plaques in these areas (Figure 8E-G). The A $\beta$  deposits and control areas (A $\beta$  plaque free) were annotated as regions of interest (ROIs). An in-house developed R script was used for data binning in order to perform data reduction and account for mass shifts.

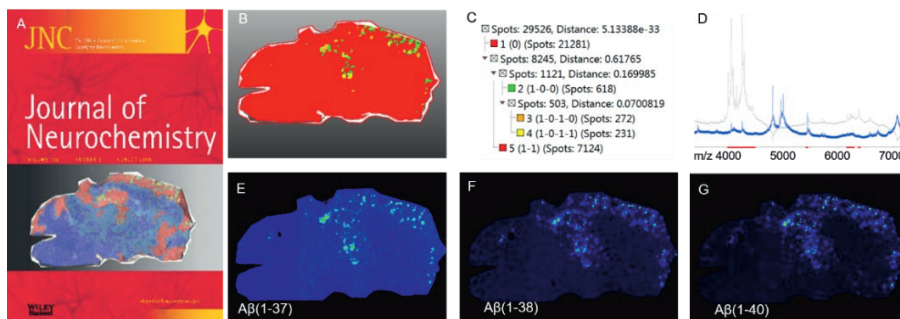


Figure 8. (A) JNC journal cover displaying segmentation of MALDI IMS data from the study. (B-D) Image segmentation and spatial correlation of MALDI IMS data identified individual A $\beta$  plaques, (E-G) and several A $\beta$  peptide truncations associated with these deposits. Adapted from Paper I, Figure 1<sup>421</sup>.

Plaque ROIs from all brain regions were subjected to correlation analysis in order to identify highly co-localized m/z values in each of the sub-regions, the hippocampus, somatosensory cortex and somatomotor associated cortex. The results show an enrichment of A $\beta$ 1-38arc and A $\beta$ 1-40arc in all A $\beta$  deposits across all brain areas. In contrast, A $\beta$ 1-42arc was found to be significantly elevated only in the hippocampus and the somatosensory associated cortex, but not in the somatomotor associated cortex. Further, based on accurate mass assignment and previously reported MALDI imaging data<sup>422</sup>, one peak at m/z 6175, which localized to hippocampal plaques, could be putatively attributed to macrophage migration inhibitory factor protein (MIF).

In order to verify the identity of the A $\beta$  deposits, immunohistochemical analysis of MALDI imaged tissue sections was performed subsequently after matrix removal. IHC was also used to verify the involvement of MIF positive, activated microglia, in the plaque vicinity. The individual A $\beta$  peptide species detected in the plaques were further verified through off-tissue analysis. Here single amyloid-positive (h-FTAA) stained plaques were collected using laser microdissection pressure catapulting (LMPC)

followed by MALDI MS/MS analysis. The LMPC-MALDI MS approach identified several more A $\beta$  species than MALDI-IMS had identified, likely due to an increased concentration of the peptides in the extracts. This confirmed the amount of analyte in tissue, as one of the major factors limiting MALDI-IMS A $\beta$  peptide detection. On the other side, the LMPC based approach (here used only for verification) is limited due to the loss of spatial information of the individual A $\beta$  peptide distributions.

The results presented in this work demonstrate that MALDI IMS is able to detect different A $\beta$  peptide species localizing to A $\beta$  plaques directly *in situ*. This approach allowed for the observation of brain-region specific differences in A $\beta$  peptide distribution. Further, in difference to more commonly used biochemical imaging, IMS allowed for both the preservation of spatial distribution of a wide array of A $\beta$  peptide and most importantly the individual A $\beta$  peptide localizations to individual plaques in different brain areas.

The MALDI IMS analyses performed here are based on the relative signal intensities between different ROIs. Hence, the lack of significant A $\beta$ 1-42 accumulation in somatosensory associated cortex, in contrast to other regions observed here, could be explained by the disperse distribution of the peptide forming soluble intra- and extra-neuronal accumulations that are not specific to plaque. Likewise, regional differences in aggregation and peptide production could underlie these observed results. Indeed, as accumulation of A $\beta$ 1-42 is considered the initial driver of A $\beta$  plaque formation, these findings support the theory that A $\beta$ 1-42 might comprise the initial seed for plaque formation<sup>125</sup>.

Finally, MIF is a pro-inflammatory cytokine expressed in microglia and is considered to play an important role in brain inflammatory processes<sup>423,424</sup>. The characteristic localization of MIF to A $\beta$  plaques confirms a high degree of microglial activation, which is suggested to be an important factor in AD pathology. In combination with previous IHC and LMPC-MS plaque studies, this verifies the presence of a variety of other molecular species, in addition to A $\beta$  itself, in A $\beta$  plaque formation.

## 4.2 Paper II: Use of MALDI and SIMS IMS to study A $\beta$ peptide-lipid interplay in AD

In Paper I we demonstrated that MALDI IMS can be used to study A $\beta$  peptides associated with individual A $\beta$  plaques. However, MALDI IMS has previously been demonstrated to be suitable for the analysis of other biomolecules, such as lipids. Similar to MALDI, TOF-SIMS is another IMS modality that has been demonstrated as suitable for tissue analysis, in particular when operated in a static mode (majority of biological studies), which does not result in molecular tissue distortion. These two IMS ionization techniques can be highly complementary. SIMS offers submicron imaging (<1 $\mu$ m), however is limited by relatively low mass range ( $m/z$  <1500 Da) making it suitable mainly for the analysis of metabolites, drugs and lipids as well as inorganics. MALDI, on the other hand is suitable for the analysis of intact proteins and peptides, including A $\beta$  peptides (as demonstrated in Paper I), however at a much lower lateral resolution (down to 5-10 $\mu$ m).

Therefore, we performed multimodal IMS, using TOF SIMS and MALDI IMS of lipids, and subsequently performed a MALDI IMS analysis of proteins and peptides on the same tissue section. The aim was to receive a comprehensive molecular insight into brain tissue from transgenic AD mice in order to elucidate potential A $\beta$  peptide-lipid interplay specific for A $\beta$  plaque pathology. SIMS imaging of lipids was performed using ION-TOF V ToF-SIMS instrument equipped with a Bi $_3^+$  ion source. MALDI IMS was then performed for a subsequent analysis of lipids (using 1,5-DAN as matrix). Following sublimation of the DAN matrix, a second coating with 2,5-DHAP was performed for subsequent MALDI IMS based-protein analysis. The data collected from modalities were then subjected to multivariate image analysis using both PCA and bisecting k-mean clustering.

Here, both SIMS and MALDI IMS identified general depletion of sulfatides in the cortical regions. No A $\beta$  plaque resembling features were observed in the TOF-SIMS data. In line with previous observations, MALDI IMS enabled the detection of plaque-like features in lipid data. These were further verified as A $\beta$  plaques by subsequent peptide analysis.

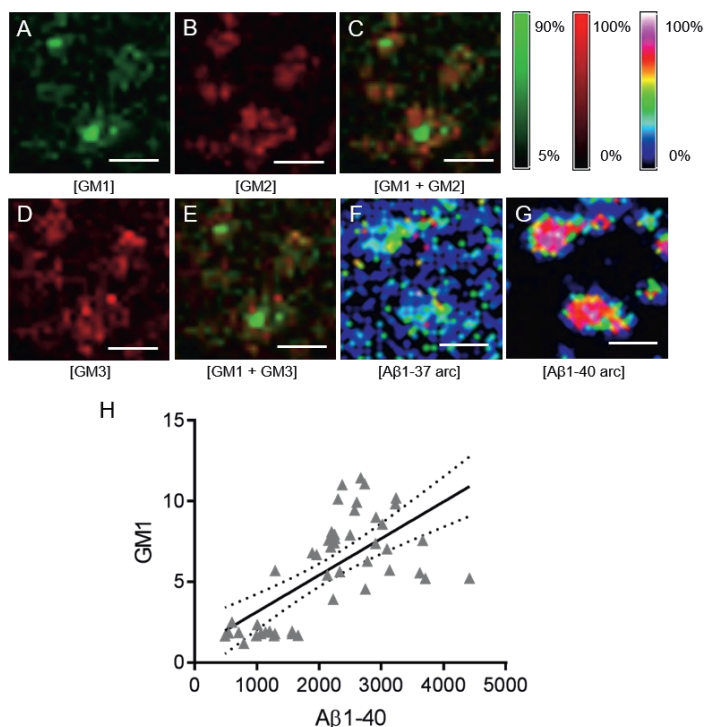


*Figure 9. Heterogeneous ganglioside distribution within a single plaques is associated with distinct Aβ peptide profiles. (A-E) Inspection of individual single ion images revealed core specific localization of GM1, and a complementary localization of the GM2 and GM3 species. (F,G) Further, while some Aβ species, including Aβ1-37, displayed a rather homogenous distribution across individual plaques, a clear gradient of Aβ1-40arc signal from center to the periphery was observed. (H) Correlation analysis between individual lipid and peptides species, revealed a significant relationship between the GM1 and Aβ1-40arc ( $R^2=0.4518$ ,  $p < 0.001$ ), scalebar=100μm. Adapted from Paper II, Figure 5<sup>425</sup>.*

Several ceramides (Cer), gangliosides (GM) and anionic phosphoinositols (PI) were observed to localize to the Aβ plaque. Interestingly, close evaluation of the single ion images revealed distinct localization of GM1 mainly to the center of the deposits (Figure 9A). In contrast, shorter in GM2 and GM3 displayed a complementary spatial distribution pattern, with localization primarily to the periphery of the plaques (Figure 9B-E). Similarly, although not as pronounced, differences in the Aβ peptide pattern were also observed. Here, the Aβ1-40arc appeared to strongly localize to the center of the plaques, while other species displayed a more homogenous signal across the



plaques (Figure 9F,G). Correlation analysis of the GM1 and A $\beta$ 1-40arc confirmed their significant association (Figure 9H).

The data presented here yet again demonstrated the potential of IMS to elucidate potential mechanism underlying the AD pathology. As revealed by MALDI IMS, GM metabolism seems to be associated with core formation in A $\beta$  plaques. Indeed, GM1 has been implicated in the AD pathology, through formation of GM1-A $\beta$  complexes, which both promote aggregation (demonstrated in particular for the A $\beta$ 1-40), but might also function as a neuroprotective mechanism. Therefore, findings observed here support the idea that the role of GM-A $\beta$  interactions are critical for AD.

Both TOF-SIMS, and MALDI IMS proved useful for studying various molecular species in AD. Even though the ion probe used for analysis with TOF-SIMS (here operated in high current bunched mode (HBC)) was much smaller, allowing for pixel resolution of 5 $\mu$ m compared to 15 $\mu$ m with MALDI, TOF-SIMS did not allow for the visualization of individual amyloid deposits. This lack of signal likely has to do with the sensitivity of the instrument, the amount of extracted material, and, perhaps most importantly, the fact that the matrix used for MALDI analysis likely helps with ionization of the lipid species detected.

### 4.3 Paper III: Compatibility of MALDI IMS with fluorescent IHC

While offering an immense potential for molecular histology, to interface MALDI IMS with (immune-) fluorescent staining is challenging as the laser ablation process in MALDI analysis can induce tissue distortions. These distortions are caused by mechanical stress and thermal denaturation resulting from the laser pulses. Still, histological staining based on chromogens, in particular haematoxylin and eosin (H&E) staining, is typically performed following an MALDI IMS data acquisition. These stains do not target specific biomolecules but rather stain a broad class of biomolecules. In comparison to H&E staining, highly specific epitope-directed immunohistochemistry analysis is rarely performed in pathology. Similarly, only a few studies demonstrated MALDI IMS with subsequent IHC analysis<sup>421,426,427</sup> While inconclusive, visual inspection of images from these studies suggest that laser ablations in MALDI IMS might impact subsequent staining, in particular that which is based on fluorescence detection.

Presence of such visual tissue distortion highlights the need for determining the impact of MALDI IMS analysis on subsequent fluorescent detection. Since laser ablation during MALDI is indeed detrimental for tissue morphology, we asked whether it was possible to optimize IMS analysis such that it would not impair subsequent fluorescent-based IHC analysis.

In order to assess the compatibility of MALDI IMS with subsequent fluorescent IHC, we evaluated three commonly used matrix compounds, 1,5-DAN, 2,5-DHB and CHCA. While all of these are suitable for the analysis of lipids, they possess different physiochemical properties, which affect their interaction with the laser. Indeed, in alignment with previous observations<sup>428,429</sup>, 1,5-DAN appeared to result in best spectral quality at a given laser energy (fluence). Given that laser fluence, and possibly the number of shots per pixel, would influence tissue distortion, we proceeded with 1,5-DAN for subsequent assessment of tissue integrity.

Similar to previously reported results, we observed an increase in 1,5-DAN matrix clusters with increased laser fluence. This increase in clusters was also present when the number of laser shots was increased. For both, the effect was more prominent in the negative ion mode. We therefore assessed the effect of gradual changes in both laser fluence and the number of shots at a given pixel on the general integrity of the tissue. This was done through fluorescent staining using both antibodies (toward glial fibrillary acidic protein (GFAP),  $\beta$ III-tubulin) as well as a fluorophore (DNA specific 4,6-diamidino-2-phenylindole (DAPI)) (Figure 10).

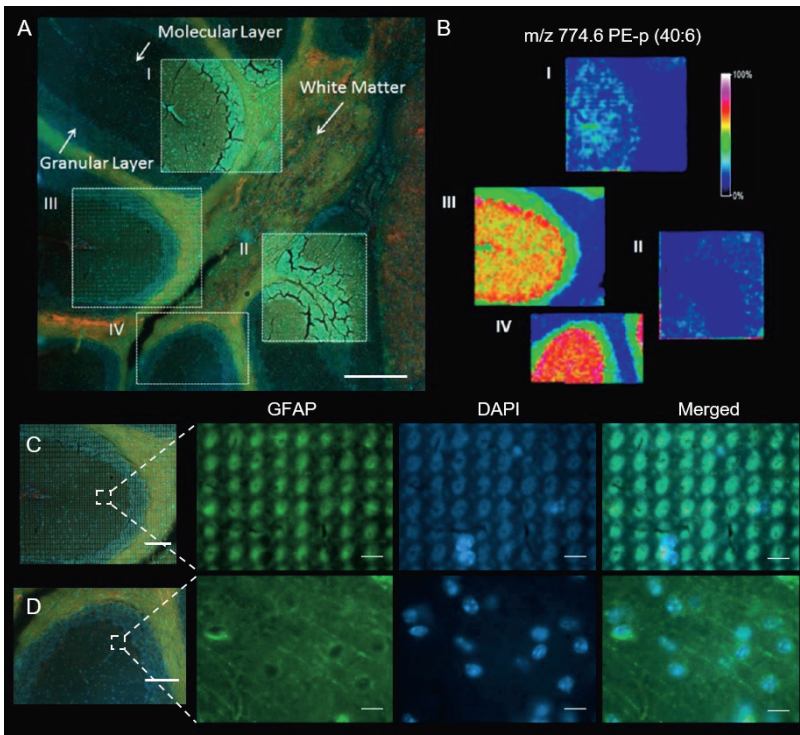


Figure 10. (A,B) MALDI IMS lipid analysis ( $m/z$  774.6) and subsequent IHC (GFAP-green,  $\beta$ III-tubulin-red, DAPI-blue) based fluorescent staining, as demonstrated through the acquisition of four regions using different settings (I) 100 shots at 50% laser energy (II) 5 shots at 50%, (III) 100 shots at threshold-energy, (IV) 5 shots at threshold-energy. (C,D) Zooms of small region in the regions III and IV, demonstrate histology preservation of the tissue when acquisition of the data is done with minimal number of shots (5 shots) at threshold-energy. Scalebars: (A)  $300\mu\text{m}$ , (C)  $100\mu\text{m}$  and zoom  $10\mu\text{m}$ . Adapted from Paper III, Figure 2 and 3<sup>430</sup>.

Indeed, maintaining threshold laser energy and a minimal number of shots yielded the best quality of single ion images (Figure 10 A,B). At the same time, this resulted in the preservation of the tissue, which otherwise appeared more or less deteriorated, ranging from individual laser ablation spots (little laser impact) to general tissue cracking (Figure 10 C,D). In contrast, we observed no tissue distortions in the H&E stain, even when using more “harsh” acquisition parameters. Finally, we demonstrated the possibility to use a fluorescent amyloid probe in combination with the “gentle” 1,5-DAN acquisition parameters for combined MALDI-IMS and subsequent fluorescent staining of A $\beta$  plaques.

The results obtained in this study demonstrate that histological staining, including that done with fluorescence-based detection, can be performed following MALDI IMS analysis. The differences observed on tissue morphology, as visualized through the use of chromogens (H&E staining) as compared to fluorescence, demonstrate the need to use fluorescence detection as the method of choice to truly assess morphological integrity of a tissue following a MALDI IMS experiment.

The 1,5-DAN has relatively low ionization energy and therefore proved to be highly suitable for subsequent analysis. Since only few shots per pixel were used when analysing the sample with 1,5-DAN, an increase in the general speed of acquisition could also be observed. While the use of other matrices for combined MALDI IMS – fluorescent IHC studies might be possible, this might require elaborate optimization (including e.g. thicker matrix layer deposition). Further, this might be especially challenging if attempted in combination with protein IMS rather than lipid IMS. Here, extraction of tissue proteins requires extensive sample washes, which might already impact the tissue. Further, protein desorption during the MALDI IMS, might also require higher laser fluence due to their size. Still, the use of MALDI-IMS and Fluorescent IMS, even when used only for lipids, offers tremendous possibilities for probing pathology of neurodegenerative diseases.

#### 4.4 Paper IV: Combination of MALDI IMS and structural LCO staining to study A $\beta$ aggregation state associated neuronal lipids

Structurally heterogeneous amyloid beta (A $\beta$ ) plaque pathology is considered one of the major pathological features of Alzheimer's disease<sup>431,432</sup>. This has been suggested to be associated with differential deposition of truncated A $\beta$  peptides. Structural analysis of individual polymorphic A $\beta$  plaques requires either multiplexing of aggregation state specific antibodies (and fluorescence detection), or the use of structure specific fluorescent amyloid probes (e.g. luminescent conjugated oligothiophenes, LCOs). In order to identify what chemical species underlie the amyloid polymorphism it is of great interest to interface MALDI IMS with subsequent fluorescent imaging both using IHC and chemical amyloid staining (LCO). This interface would allow us to perform structure specific analysis of A $\beta$  plaques and enable accurate correlation between IMS data and the subsequent histological assessment.

MALDI-IMS analysis of proteins/peptides (as performed in Paper I) requires analysis conditions that are harsh for the analysed tissue and do not allow subsequent fluorescent imaging. In contrast, lipid imaging using 1,5-diaminonaphthalene (1,5-DAN) as the matrix as demonstrated in Paper III is a much gentler approach. MALDI-IMS lipid analysis with follow up histological and structural amyloid staining using LCO amyloid probes. These LCO probes offer the possibility to investigate the different aggregation state of the same amyloidogenic protein. Here, concomitant staining with q-FTAA visualizes mature A $\beta$  fibrils and h-FTAA, which furthermore allows for the recognition of the protofibrillar and prefibrillar A $\beta$  aggregation intermediates<sup>311,312</sup>.

We therefore wondered whether performing multimodal data analysis using MALDI-IMS imaging of lipid, with subsequent structural LCO staining, could yield additional information about lipid involvement in structural diversity in A $\beta$  plaque pathology of AD. For this purpose, tgAPP<sub>Swe</sub> mice, rather than the tgAPP<sub>ArcSwe</sub> mice were chosen for analysis. These mice display a systematic structural diversity among plaques, with

both cored and diffuse present in full-blown plaque pathology reached at 18 months  
433,434

Following MALDI based-lipid imaging, the analysed sections were double stained with q-FTAA and h-FTAA (Figure 11A-F). Spectral imaging was performed using LSM 710 NLO laser-scanning microscope equipped with a 34-channel QUASAR detector (Zeiss), using 405nm laser for qFTAA and 480nm laser for hFTAA excitation (Figure 11G). Individual plaques could then be classified based on their hyperspectral emission profiles (Figure 11E, H-K). IMS data was subjected to multivariate image analysis using spatial segmentation and PCA (Figure 10L-N). IHC staining of the consecutive section was performed in order to verify the identity of the inclusions as A $\beta$  positive. This staining was done using antibody-based IHC, and laser microdissection pressure catapulting (LMPC) flowed by A $\beta$  immunoprecipitation and MS analysis (IP-MS).

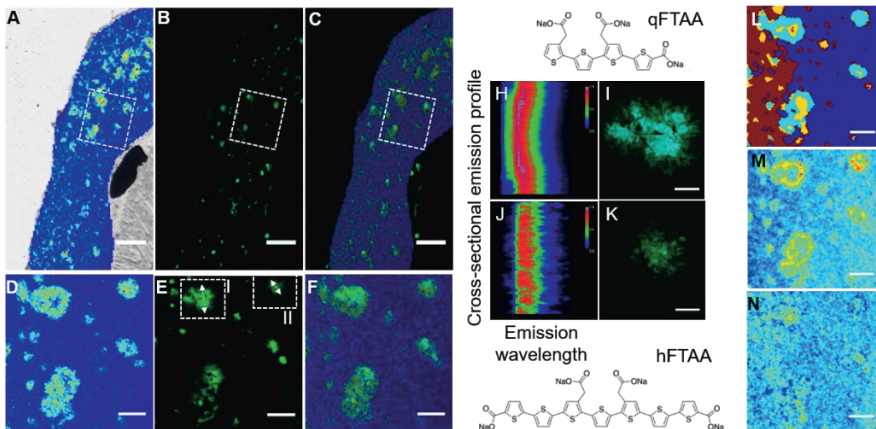


Figure 11. (A-C, zoom: D-F) Histology compatible MALDI IMS of lipids with subsequent LCO double staining allows a high degree of co-localization between imaging modalities. (H-K) The q-FTAA and h-FTAA double staining with subsequent heatmap-based hyperspectral analysis of cross-sectional emission profiles from individual deposits allowed for the identification of cored (blue shifted, top) and diffuse plaques. (L-N) Multivariate analysis through spatial segmentation and PCA revealed lipid distribution patterns associated with amyloid structural polymorphism (diffuse respective dense cored structures). Adapted from Paper IV, Figure 1<sup>329</sup>.

Investigation of hyperspectral imaging data and lipid IMS data revealed that distinct fluorescence emission and mass spectral features were present across individual A $\beta$  plaques. Here, a spectral shift towards shorter wavelengths, corresponding to q-FTAA staining, appeared to be present in the dense core. A general h-FTAA staining was associated with more diffuse structures. In terms of lipids, three distinct lipid localization patterns were present.

First, a general plaque accumulation of gangliosides (GM2/GM3) and ceramides (Cer), as well as a respective depletion of sulfatides (ST), was observed in all deposits irrespective of plaque morphology. This observation was also complemented by morphology-independent localization of arachidonic acid (AA) conjugated phosphatidic acids (PA) and lyso-PA.

In contrast, a morphology-dependent localization pattern of ceramide matching cerebroside (HexCer) and phospho-ceramides (CerP and PE-Cer) displayed significant localization solely to the center of cored A $\beta$  plaques. Moreover, a specific localization to the periphery of cored plaques and diffuse deposits was observed not only for arachidonic acid (AA) but also for docosahexaenoic acid (DHA) containing anionic phosphoinositols (PI), as well as lyso-PI (LPI). Finally, the LMPC-IP-MS, suggested that presence of the cores in the plaques was associated with an increased A $\beta$ 1-40/1-42 ratio.

Previous studies suggest the involvement of differentially localized phospho-ceramides as well as omega-3 (DHA) and omega-6 (AA) conjugated fatty acids in cellular mechanism. Here, both PE-Cer and Cer1P have been proposed to suppress ceramide-induced apoptosis<sup>435-438</sup>. On the other hand, DHA and AA are essential precursors in eicosanoid synthesis underlying inflammatory response mechanisms<sup>439-441</sup>. Interestingly, while DHA has been suggested to have an anti-inflammatory role and prevent cognitive decline at prodrome of AD<sup>439</sup>, AA appears to play a crucial role in A $\beta$  pathogenesis<sup>295,442</sup>. Therefore, while the observed accumulation of phospho-ceramides could indicate a cellular defense mechanism that prevents apoptosis at the site of A $\beta$  core formation, localization of AA and possibly DHA containing

phospholipids to the diffuse plaques and periphery of cored A $\beta$  deposits, likely reflects their involvement in the immune response at the site of plaque formation. This localization appears to also be linked to A $\beta$  peptide truncations (A $\beta$ 1-40 in cored-, respective A $\beta$ 1-42 in diffuse plaque areas).

Taken together, high resolution MALDI-IMS when combined with complementary methods, such as structural amyloid differentiation based on LCOs, offers the opportunity to both elucidate chemical differences in plaque populations and enables correlation of chemical distribution patterns to morphological features detected through hyperspectral analysis. The multimodal chemical imaging data presented in this work suggest differential roles of various lipid species associated with polymorphic A $\beta$  aggregation. These results emphasize the need to study morphological heterogeneity among A $\beta$  plaques, as further studies might shed light upon the mechanisms underlying the diverse aggregation of A $\beta$  peptides into structurally distinct deposits.



## 4.5 Paper V: MALDI IMS and structural LCO staining delineate A $\beta$ peptide truncations associated with plaque polymorphism

Morphologically heterogeneous amyloid beta (A $\beta$ ) plaque pathology have been suggested to differ not only in terms of structure, but also in terms of chemical composition<sup>431,432</sup>. In particular, A $\beta$ 1-42, commonly believed to seed the plaque pathology, has been suggested to be the main constituent of protofibrils<sup>443</sup>, and underlie the diffuse deposits<sup>57,58</sup>. In contrast, more aggregated cored deposits have been suggested to display more A $\beta$ 1-40 antibody staining<sup>56,434,444-446</sup>. Further, recent study, were antibody detected, LMPC isolated and Lys-C digested cored deposits in PS2APP mice were analysed did also show such A $\beta$ 1-40 positivity<sup>447</sup>. In agreement with previous studies, the MALDI IMS analysis performed in Paper I revealed brain region specific differences in A $\beta$  peptide composition in tgAPP<sub>ArcSwe</sub> mice. Further, LMPC-IP-MS, respective IMS analysis in Paper III and Paper IV, of both tgAPP<sub>ArcSwe</sub> and tgAPP<sub>Swe</sub> mice suggested both inter- and intra-plaque heterogeneity in terms of both A $\beta$  peptide and lipid composition.

The A $\beta$  plaque pathology is present not only in Alzheimer's patients (sporadic (sAD) and familial (fAD)), but has also been found for instance in cognitively unaffected amyloid positive patients (CU-AP). A $\beta$  plaques present in CU-AP brains are mostly diffuse in nature, whereas in sAD brains the A $\beta$  plaques are mostly mature/cored. Therefore, we wondered whether the A $\beta$  core identification with subsequent MS analysis, as used in Paper III, could also be used to reveal A $\beta$ -peptides truly associated with the core formation in sAD, as well as to elucidate potential similarities and differences between diffuse plaques in sAD and CU-AP.

To assess polymorphism associated amyloid peptide signatures, we investigated *post-mortem* brain tissue (temporal cortex) from 8 sAD patients and 4 CU-AP patients. For this, the q-FTAA/h-FTAA staining approach described in Paper IV was used for hyperspectral imaging guided plaque annotation and subsequent isolation with LMPC and IP-MS based A $\beta$  detection. In order to verify the plaque type and specific A $\beta$  peptide distributions observed in LCO/LMPC-IP-MS experiments, MALDI IMS was

performed on a consecutive tissue section to avoid interference with the hyperspectral fluorescent imaging.

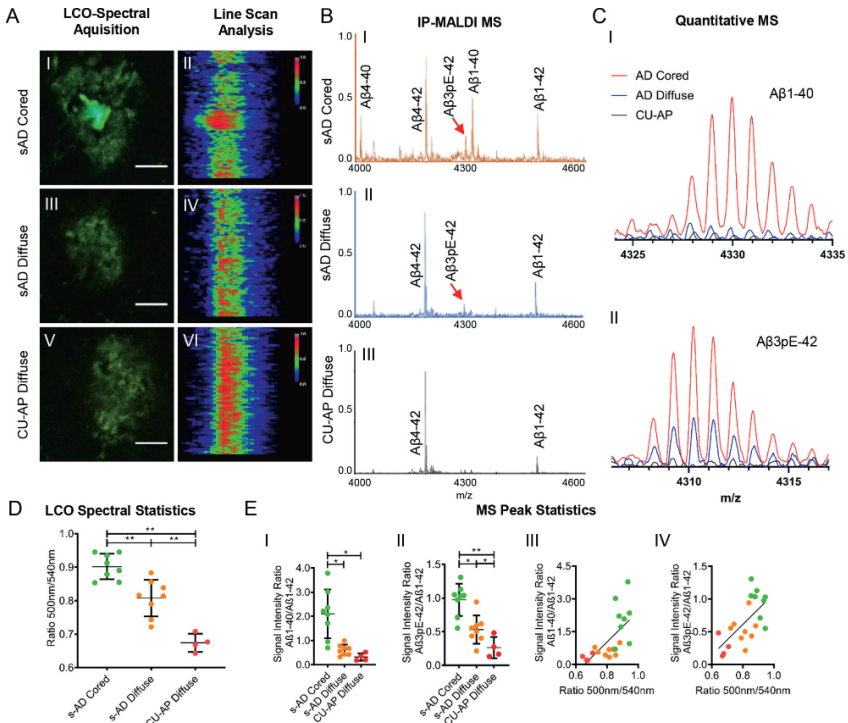


Figure 12. (A,D) Double staining with q-FTAA and h-FTAA with subsequent heatmap based spectral delineation of diffuse plaques in CU-AP, and cored and diffuse plaques in sAD. The 500/540nm emission ratio, corresponding to qFTAA and hFTAA emission maxima, revealed structural heterogeneity between morphologically similar diffuse plaques in CU-AP and sAD. (B,C,E) Mass spectrometric analysis of extracts from spectrally delineated and LMPC isolated plaque subpopulations, demonstrate enrichment of Aβ1-40 is specifically in cored plaques in sAD. Further, the presence of pyroglutamate-modified Aβ species appears to be associated with sAD patients. Scalebar: 25μm. Adapted from Paper V, Figure 1<sup>448</sup>.

Based on the described hyperspectral paradigm, we identified spectral differences between cored and diffuse plaques in sAD (blue shift across the core), and also between diffuse plaques in sAD and those present in CU-AP cases (Figure 12A,D). In combination with LMPC-IP-MS data, and subsequent MALDI IMS spatial verification, this showed that the presence of the core was indeed associated with the deposition of Aβ1-40 peptide (Figure 12B,C,E). The generally more blue-shifted

homogenous emission of diffuse plaques in sAD, compared to diffuse plaques in CU-AP, was shown to be associated with an increased amount of N-terminally pyroglutamated A $\beta$ 3pE-42 (Figure 12B,C,E). Interestingly, the A $\beta$ 4-42 peptide appeared to be the most prominent peptide in all types of plaques (both sAD and CU-AP). Further, closer investigation of the general spatial distribution pattern of N-terminally truncated A $\beta$  peptides showed that they did indeed follow the same core/respective periphery localization as the A $\beta$ 1-40, respective A $\beta$ 1-42. In addition, the results show that vascular deposits (CAA) in human sAD consisted mainly of A $\beta$ 1-40 and A $\beta$ 4-40 peptides.

To gain a more mechanistic insight into evolving plaque pathology, the human tissue analysis were complemented with LCO-IP analysis 12-, and 18-months old tgAPP<sub>Swe</sub> mice. In tgAPP<sub>Swe</sub> mice, A $\beta$ 1-40 was the most prominent peptide, whose deposition mechanism appeared to be age-dependent. Cored plaques in 12-month-old mice displayed lower A $\beta$ 1-40/A $\beta$ 1-42, compared to the 18-month-old mice. This trend was even more prominent when investigating the CAA pathology in these mice.

Together, these results provide further support for the theory that A $\beta$  deposit maturation is reflected in an increased content of less hydrophobic C-terminal peptides, such as A $\beta$ 1-40. Spectrally, this increase is represented by the blue shift corresponding to q-FTAA staining, and presence of more mature, dense fibrillary structures, apparent particularly in cored plaques and CAA. In line with these observations, a higher risk of CAA associated hemorrhage is observed in fAD subjects with mutations leading to an increase in total A $\beta$ , rather than those mutations which lead to a relative increase in A $\beta$ 1-42/A $\beta$ 1-40 ratio<sup>56,60,174</sup>. Therefore, our results strengthen previous suggestions that a higher rigidity of A $\beta$ 40 fibrils might underlie the CAA occurrence<sup>56,59,60</sup>. Further, as presented here, differences in individual peptides, such as A $\beta$ 3pE-42, might underlie morphologically similar plaques, but with actually structurally different fibrils. Here, such case is demonstrated between diffuse plaques in sAD and CU-AP.

Therefore, our data demonstrates that hyperspectral imaging guided - MS based workflow is a powerful alternative to conventional IHC assessment of A $\beta$  pathology

in AD. When combined with LMPC-IP-MS experiments, the LCO approach allows for the analysis of pooled and purified plaque extracts, which yield a higher signal and possibility for MS/MS verification. On the other hand, when combined with IMS, hyperspectral imaging allows for the spatial analysis of multiple A $\beta$  peptides, and the identification of distinct localization patterns, such as similar localizations of N-terminally truncated forms of the major C-terminal truncations (i.e. A $\beta$ <sub>x-42</sub> appear to have one localization pattern, and A $\beta$ <sub>x-40</sub>, another) at the individual plaque level. Further, analysis of intact A $\beta$  species through IP-MS and IMS overcome the limitations of proteomic approaches such as incomplete A $\beta$  digestion, which likely influences relative levels and diversity of A $\beta$  peptides observed.

## 4.6 Paper VI: Use MALDI IMS to study A $\beta$ processing and deposition across regions and ages

A $\beta$  plaque precipitation is believed to start long before the onset of clinical symptoms. The chain of events that lead to A $\beta$  peptide aggregation into plaques, however, remains unclear. On top of that, the presence of both diffuse and cored deposits further complicates the matter. Still, A $\beta$  plaque maturation has long been proposed as the main mechanism underlying the transition of diffuse A $\beta$  plaque pathology into cored plaques. Based on the results presented in Paper V, this appears to be associated with precipitation of A $\beta$ 1-40. There are many other truncated A $\beta$  peptides present in the plaques, and their distribution across anatomical regions can differ. Therefore, we wondered whether we could employ MALDI IMS to probe the evolution of A $\beta$  plaque pathology in AD over time.

For this purpose, we investigated tissue sections from 6-, 9-, 12-, 18-, and 23-month-old tgAPP<sub>Swe</sub> mice using MALDI IMS. TgAPP<sub>Swe</sub> mice display the first signs of plaque pathology typically around 12-months, and exhibit extensive A $\beta$  plaque pathology by 18-months. Therefore, this cohort represented both animals where A $\beta$  plaque pathology was not yet developed, as well as those where the full-blown pathology had been present for some time. Following the MALDI IMS analysis, a simple h-FTAA staining was performed in order to allow for a visual inspection of any amyloid deposits. For the division of A $\beta$  plaques into cored and diffuse subpopulations, we employed spatial segmentation. This technique allowed for characterization purely based on the chemical signature as revealed by IMS.

No plaques, or for that matter any A $\beta$  peptide signal, were detected in 6-, and 9-month-old animals. Further, A $\beta$  plaques present in 12-month-old mice were observed only in the somatomotor cortex. Older mice, on the other hand, displayed full-blown pathology. Single plaque analysis, based on the A $\beta$  plaque ROIs identified through spatial segmentation, revealed a trend similar to that reported in Paper V where cored plaques in 18- and 23-month-old mice had a significantly higher A $\beta$ 1-40/A $\beta$ 1-42 peptide ratio. Interestingly, the ratio appeared to be consistent across all three analysed regions, the somatomotor cortex, hippocampus, and somatosensory cortex, for both the

pseudo-clusters corresponding to either diffuse plaques or cored plaques. The A $\beta$ 1-40/A $\beta$ 1-42 ratio in the 12-month old animals was intermediate to that of diffuse and cored plaques in older mice.

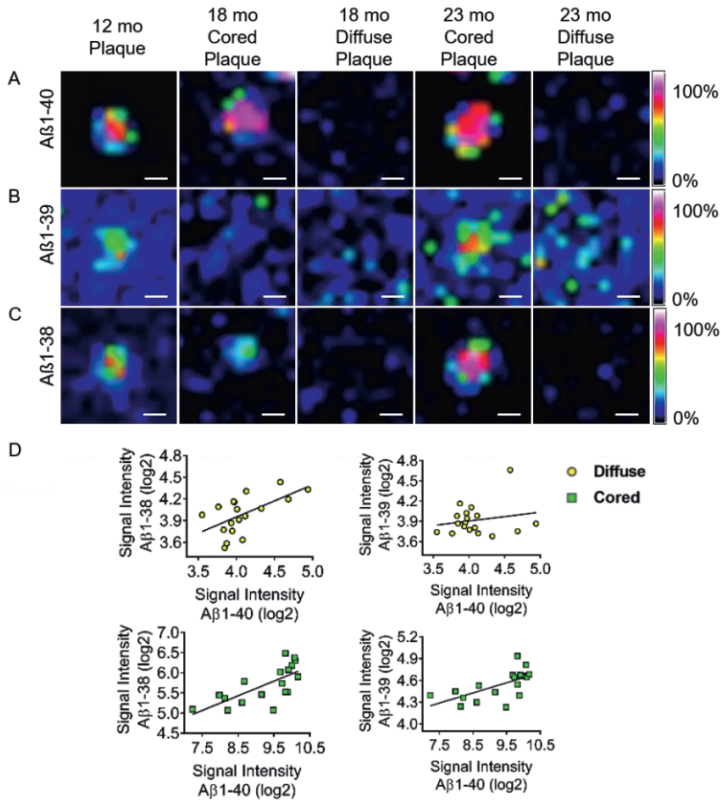


*Figure 13. (A) MALDI IMS of individual plaques revealed strong localization of A $\beta$ 1-40 peptide in cored deposits. (B,C) Further, A $\beta$ 1-38 and A $\beta$ 1-39 displayed similar localization patterns as A $\beta$ 1-40 peptide. Correlation analysis revealed strong correlation between A $\beta$ 1-38 and A $\beta$ 1-40 in both diffuse and cored plaques. This suggests co-precipitation or co-processing of the A $\beta$ 1-38 and A $\beta$ 1-40 peptides in tgSwe mice. Adapted from Paper VI, Figure 6.*

IMS analysis identified three other A $\beta$  peptides in the plaques. These included C-terminally truncated A $\beta$ 1-37, A $\beta$ 1-38, and A $\beta$ 1-39. The localization of A $\beta$ 1-37 was present in small amounts, with only some plaques displaying the signal. Further, the A $\beta$ 1-37 did not differ between the diffuse and cored plaques. The signals of A $\beta$ 1-38 and A $\beta$ 1-39 were stronger in the cored plaques compared to the diffuse plaques (Figure 13 A-C). Correlation analysis revealed a weak correlation of A $\beta$ 1-38 and A $\beta$ 1-40 in

diffuse plaques (Figure 13D, top). On the other hand, both A $\beta$ 1-38 and A $\beta$ 1-39 correlated with the A $\beta$ 1-40 signal in cored plaques (Figure 13D, bottom).

The data presented here is in agreement with previous IHC based results on tgAPP<sub>Swe</sub> where the first plaques were observed in the neocortex of 12-month-old mice. This reaffirmation demonstrates that MALDI IMS can be used for early A $\beta$  plaque detection. Further, IMS analysis offers the benefit of chemical classification of plaques based on their multi peptide pattern, and relative signal ratio, which is not easily achievable with IHC. Surprisingly, only two pseudo clusters, corresponding to diffuse and cored plaques in 18-, and 23-month-old mice, were observed, which indicates that plaque types (cored respective diffuse) remain similar across ages and areas. Still, IMS based relative quantification allowed for the identification of an intermediate A $\beta$ 1-40/A $\beta$ 1-42 ratio in plaques in 12-month-old mice, compared to diffuse and cored plaques in older mice. One could speculate this to be a result of a “sink effect”<sup>299,312</sup>. In the presence of limited pathology, A $\beta$ 1-42 seeded structures quickly drive deposition of other peptides into new plaques. In older mice where an extensive pathology is present, new A $\beta$ 1-42 seeds are formed more frequently, leading to a more heterogeneous A $\beta$  plaque subpopulation.

Besides the clear difference in A $\beta$ 1-40/A $\beta$ 1-42 ratio across plaque types, MALDI IMS data also reveals potential sequential processing patterns responsible for the generation of shorter C-terminally truncated peptides. In particular, A $\beta$ 1-38, previously shown to be generated independently of A $\beta$ 1-42<sup>98,449</sup>, appears to strongly correlate with the precipitation of the dominant A $\beta$ 1-40.

In conclusion, data presented here demonstrates that MALDI IMS can be used for time series experiments centered on the A $\beta$  plaque pathology, similar to IHC studies. It does however outperform conventional IHC as it offers the advantage of simultaneous relative quantification of multiple A $\beta$  peptides at a single plaque level. Still, like other *post-mortem* in situ analyses, MALDI IMS provides only static information and does not to resolve the true temporal timeline of A $\beta$  peptide specific accumulation, aggregation and deposition in the formation and growth process of single A $\beta$  plaques.

## 4.7 Paper VII: Development of iSILK for spatiotemporal analysis of A $\beta$ plaque spread, formation and development

Evolution of A $\beta$  plaque pathology is not well understood. Furthermore, the study of A $\beta$  plaque evolution through conventional IHC based time series experiments, or even MALDI IMS, as presented in Paper VI, has its limitations. These analyses allow for the identification of changes in A $\beta$  peptide composition within single plaques across ages. Further, they enable comparison of A $\beta$  in different regions. With these in situ imaging approaches there is, however, no way to actually tell which A $\beta$  peptides were deposited first, and which ones were generated and deposited at a later time point as these are only static measurements. Neither is it possible to truly delineate the primary site of plaque deposition, both in terms of anatomical regions, but also in terms of how a plaque physically grows in size. The advent of metabolic labelling with stable isotopes together with mass spectrometry analysis greatly increases the resolution of dynamic molecular interactions events *in vivo*.

Stable isotope labelling kinetics (SILK) has been shown to be a powerful tool to measure protein turnover dynamics in cells, tissue and bodily fluids. Recently, it has also been demonstrated to be useful for probing A $\beta$  peptide turnover in cerebrospinal fluid (CSF) from AD patients<sup>450,451</sup>. IMS based analysis of metabolically labeled tissue has also been demonstrated<sup>452-454</sup>.

We were therefore curious as to whether metabolic labeling with stable isotopes combined with IMS could be used to visualize true A $\beta$  aggregation dynamics in morphologically heterogeneous plaques across different brain regions.

To help answer this question, we developed a novel multimodal approach to image stable isotope labelling kinetics (iSILK) to visualize A $\beta$  aggregation dynamics *in vivo*. For this, we isotopically labeled (<sup>15</sup>N) recently developed knock in mice with familial mutations in Amyloid Precursor Protein (APP<sup>NL-G-F</sup>)<sup>208</sup> using different labeling schemes: one labelling starting prior to and one after the reported plaque onset (Figure 14A). Half of the brain of the labeled mice was frozen, while the other half was subjected to chemical processing for EM. Analysis of the heavy nitrogen's



incorporation into the A $\beta$  sequence peptides was performed on the frozen tissue using MALDI imaging (Figure 14B). Sections adjacent to those analysed through MALDI IMS were double stained with q-FTAA and h-FTAA, and delineated in terms of amyloid aggregation state following hyperspectral image acquisition (Figure 14C). EM prepared tissue obtained from the other hemisphere was analysed through annular bright-field STEM analysis using GAIA3, a FIB-SEM workstation. Subsequent super high-resolution analysis and quantification of  $^{15}\text{N}$  within single plaques was performed using NanoSIMS (Figure 14D,E).

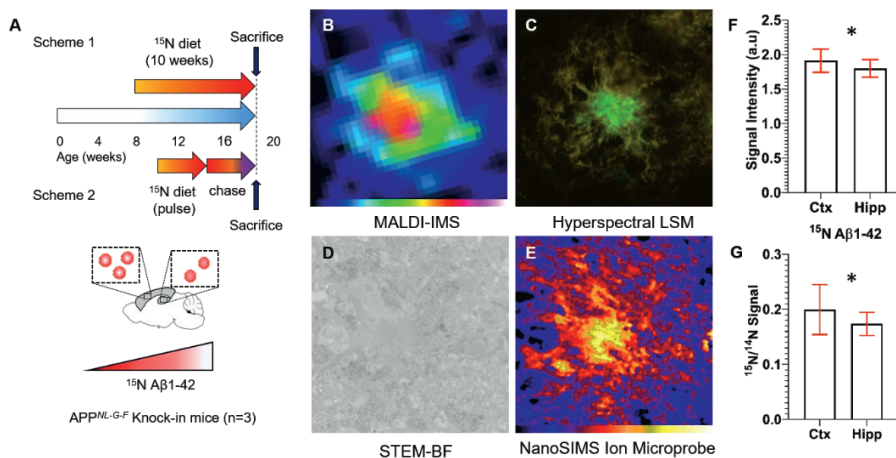


*Figure 14. (A) Two feeding schemes were done in order to perform the novel multimodal imaging of stable isotope labelling kinetics (iSILK). In this approach (B) MALDI-IMS, (C) hyperspectral LSM analysis of LCO double stained tissue, (D) STEM ultrastructural analysis, and (E) NanoSIMS analysis were performed to study the A $\beta$  plaque formation, development and spread in knock-in APP<sup>NL-G-F</sup> mice. (F) Based on the  $^{15}\text{N}$  in A $\beta$ 1-42 peptides, MALDI IMS identified the cortex as primary site of A $\beta$  aggregation and deposition. (G) This was further verified through NanoSIMS analysis. Adapted from Paper VII, Figure 1 and 2.*

MALDI IMS analysis of the tissue from the APP<sup>NL-G-F</sup> metabolically labeled prior to demonstrating plaque onset revealed the presence of  $^{15}\text{N}$ -A $\beta$ 1-42 in plaques. The STEM, with subsequent NanoSIMS analysis, verified this plaque specific  $^{15}\text{N}$  signal enrichment (based on the  $^{12}\text{C}^{15}\text{N}$ -signal). Comparison of the plaques in the cortex and hippocampus of the APP<sup>NL-G-F</sup> using MALDI-IMS further revealed the cortex as the primary site of aggregation and deposition of the A $\beta$  peptides based on  $^{15}\text{N}$

incorporation (Figure 14F). This discovery was verified by the relative quantification of the  $^{15}\text{N}/^{14}\text{N}$  ratio in cortical, respective hippocampal, plaques using NanoSIMS (Figure 14G). In addition to  $^{15}\text{N}$ -A $\beta$ 1-42,  $^{15}\text{N}$ -A $\beta$ 1-38 was also observed in some of the plaques and was found to localize primarily to the core of the deposits. Inspection of individual  $^{15}\text{N}$ -A $\beta$ 1-42 with a different degree of  $^{15}\text{N}$  incorporation suggested the deposition of “older A $\beta$ ” peptides in the center of the plaques. The denser nature of the plaque center was confirmed by linear unmixing of hyperspectral data from q-FTAA/h-FTAA double staining.

An analysis of the additional feeding scheme, where  $^{15}\text{N}$  label was introduced after the initial plaque onset at 10 weeks, strengthened this observation. This data showed the presence of completely unlabeled  $^{14}\text{N}$ -A $\beta$ 1-42 predominantly in cortical plaques, primarily at the center of these deposits. This data further demonstrates that A $\beta$ 1-38 is synthesized and deposited at a later time point as no unlabeled  $^{14}\text{N}$ -A $\beta$ 1-38 was detected.

Overall, the data demonstrated verifies the primary role of A $\beta$ 1-42 peptide as seeding for A $\beta$  plaque formation in the APP<sup>NLGF</sup> mouse model. The employed iSILK approach delineates spatial plaque growth mechanism, not previously reported for either APP<sup>NL-G-F</sup> or any other mouse model. On a large scale, these results demonstrate the iSILK chemical imaging paradigm as highly suitable for general studies of A $\beta$  plaque formation dynamics over time. The iSILK method allows for the identification of the primary regions of A $\beta$  plaque deposition. Further, through close inspection of  $^{15}\text{N}$  label incorporation, iSILK also offers the possibility to delineate mechanisms responsible for A $\beta$  plaque growth, including both the order of generation and deposition of different peptides, but also the peptides’ involvement in structural heterogeneity associated with plaque growth.

## 5 CONCLUSION AND FUTURE PERSPECTIVES

Over 100 years have passed since Dr. Alois Alzheimer's initial characterization and diagnosis of his patient, Auguste Deter, with Alzheimer's disease. The initially described hallmarks of the disease, the intracellular neurofibrillary tangles (NFT) composed of hyperphosphorylated microtubule-associated protein Tau, and the extracellular plaques composed of amyloid- $\beta$  ( $A\beta$ ) peptides, remain central to the definite *post-mortem* diagnosis of AD. While both tau (total tau and phosphorylated tau) and  $A\beta$  are monitored in cerebrospinal fluid (CSF) as biomarkers of the disease, the relevance of  $A\beta$  pathology as such is currently under debate as  $A\beta$  plaques (as identified with e.g. Congo Red, CR) do not correlate with cognitive decline <sup>64,66,67</sup>.

However,  $A\beta$  plaque pathology is morphologically (e.g. diffuse and cored plaques) and structurally (polymorphism of underlying fibrils) highly heterogeneous. This heterogeneity in amyloid pathology is observed, both in between the different forms of fAD with different AD causing mutations, as well as within sAD pathology itself, as highlighted by the presence of  $A\beta$  plaques with diffuse and cored morphology. Moreover, (primarily diffuse)  $A\beta$  plaques are also present in cognitively unaffected-amyloid positive (CU-AP) patients. Along diversified plaque morphology, distinct pools of  $A\beta$  peptide truncations have been identified both in CSF but also in brain homogenates among AD subtypes and CU-AP. Furthermore, distinct  $A\beta$  peptide truncations have been suggested to underlie structural polymorphism among  $A\beta$  fibrils. Thus,  $A\beta$  plaque pathology as such is likely much more heterogeneous than simply categorizing the plaques as either diffuse (CR negative) or cored (CR positive) plaques. Instead,  $A\beta$  plaque pathology might be reflective of much more complex changes in the chemical microenvironment.

Common approaches to study  $A\beta$  plaque pathology and its diversity involve IHC with a variety of antibodies targeting the different specific  $A\beta$  peptides. This approach suffers from limitations associated with both specificity and throughput.

The studies presented in this thesis demonstrate the suitability of mass spectrometry-based chemical imaging, specifically MALDI IMS, in combination with spectroscopic approaches, such as LCO based hyperspectral fluorescence microscopy, to study the structural and chemical traits of amyloid polymorphism in A $\beta$  plaque pathology in AD. The suitability of these techniques is demonstrated in studies of both mouse models of AD as well as human *post-mortem* AD brain tissue.

A limitation of the work on *post-mortem* brain tissue is that interpretation of the results presented here cannot be directly used for diagnostic purposes due to the *post-mortem* nature of the sample. Furthermore, the tissue is obtained at a point of time when AD pathology is full-blown and degenerative, and not during the early stages of AD. Similarly, mouse models of AD display accelerated amyloid pathology without well-defined cognitive deficits limiting the translational potential of the data to biochemical aspects of the disease pathology.

However, there are still some similarities between mice models and human subjects, particularly in terms of cerebral A $\beta$  chemistry. It's widely demonstrated that large amounts of biochemical information, particularly mechanistic insight, can be obtained from animal studies performed in a controlled environment. Therefore, the high resolution multimodal approaches developed offer a great potential for the identification of novel biomarkers and, thus, targets for future treatment.

Importantly, the presented novel insights into A $\beta$  polymorphism highlight the need to revisit the A $\beta$  plaque pathology, as it is demonstrated to be highly heterogeneous both between different plaque subtypes (e.g. diffuse and cored), but also within a single A $\beta$  deposit (a single plaque). This in terms of both A $\beta$  peptides, but also lipids. Further, as demonstrated by the LCO hyperspectral imaging, this heterogeneity what is associated with the distinct aggregation states of A $\beta$  peptides.

Further work is needed to truly deepen the understanding of the A $\beta$  plaque pathology in AD. Besides the analysis of a larger cohort of patients, the expansion of the analytical approaches towards other classes of biomolecules, for instance broader proteome, glycans or different lipid classes, is necessary to truly deepen the

understanding of local microenvironment changes associated with progressing A $\beta$  plaque pathology. Here, the IMS based analysis, especially in combination with offline LMPC-based approaches, might prove itself indispensable in order to study these on a single of A $\beta$  plaque level. However, the incorporation of novel technological developments, such as ozone-induced dissociation (to study isomeric lipid molecules) or MALDI-2 (aiding ionization of neutral species through post ionization), might be needed to truly characterize the complexity of the bimolecular processes underlying these deposits<sup>366-368</sup>.

On the other hand, the approaches presented in this thesis could potentially be expanded to other protein aggregates demonstrated to exhibit structural polymorphism (e.g.  $\alpha$ -synuclein, or maybe even tau). Given the distinct characteristics of these proteins, including their molecular size (tau), application of these approaches might require further method optimization.

Finally, use of here developed the approaches for analysis of various AD causing mutations, might be crucial in aiding the delineation of the role distinct A $\beta$  peptide truncations play in A $\beta$  fibrillary and plaque polymorphism. Indeed, while the different genetic mutations have been shown to alter the A $\beta$  peptide production, the general  $\gamma$ -secretase processing, and the relative hydrophobicity of the peptides, little is known about the actual A $\beta$  peptide truncations generated, their role in amyloid structural polymorphism, or their effect on the brain's microenvironment.

# ACKNOWLEDGEMENT

Given my well-developed skill of multitasking, I was very surprised to find myself having to write this part at the very last moment. Therefore, to spare myself any embarrassment, my deepest apologies if I forget to mention someone in this section.

The last four years have been an amazing journey. It wouldn't have been the same without many different people at work and at the lab, but also in my daily life. Whether you know it or not, you have all contributed to my education in some invaluable way or another. I could go on but, in the interest of ink, I will try to keep this short.

First and foremost, I would like to thank my primary supervisor, Jörg Hanrieder. When you and I met for the first time, I had just landed after a very long flight. I was very jetlagged and, to be honest, I probably didn't comprehend the majority of our conversation at that point (and you probably know that). Still, you gave me a chance to work with you and to be a part of the development of a completely new research group. Since day one, it has been a great pleasure and privilege to work with you.

You have been a great teacher, mentor, and supervisor, tailoring your pedagogical approaches to my character. You provided me with interesting research opportunities and intellectual stimulus. Yet while giving me guidance, you also gave me freedom. At the right moments, you challenged me. And when I occasionally would get a bit too self-confident, you would remind me, in your own way, that there is still a lot to learn. While some wouldn't appreciate it, I enjoyed those occasions when you would let me wander, looking for solutions. It forced me to think on my own.

You not only taught me science, but also how to be a modern researcher. You have shown me how to see the bigger picture, how to find focus when I get a bit too far into the abyss, and how to deal with the non-strictly scientific challenges of a scientist. The list could go on but, since I already got a bit carried away in the methods section, I will try to be concise here. Thank you, Jörg, for all of this and more, and thank you for your patience with me throughout these years. I feel lucky to have had you as my supervisor.

I would like to express my sincere gratitude to my co-supervisors...

To Henrik Zetterberg, for all your constructive criticism, valuable input and always answering my “last moment” questions. Professionally, your work and dedication to science are an inspiration. Personally, your energetic positivism, regardless of the day or how busy you are, fills me with enthusiasm to approach any task or challenge I face.

To Kaj Blennow, for your guidance and allowing me to take advantage of your tremendous knowledge and experience. Your direct no-nonsense approach has taught me how to see a good study design, and to find the right focus and objectives my own projects.

Thank you, Gunnar Brinkmalm and Johan Gobom, for your answers and explanations to my questions, your help with analysis and instrumentation, and for letting me “pop-in” a few samples here and there on a short notice. Thank you also for all the discussions, scientific or not, for the unfinished thoughts (or ideas) yet to be continued... and occasionally for those unproductive ones that often made my day.

To Henrik Ryberg; for all the scientific and social activities. For the very educational sessions by the MS at the Clinical chemistry, short coffee break conversations, and wonderful company during conferences.

To Alexandra Abramsson; for the thought provoking conversations, and for letting me use your bench during my frequent visits to the Clinical chemistry unit.

To Lotta Agholme and Petra Bergström; for all the work we did together.

To Erik Portelius Ann Brinkmalm, Kina Höglund, Annika Öhrfelt, Bruno Becker, Jessica Holmen-Larsson; for always being available to answer my questions.

To Celia Hök Fröhlander and Steffan Persson; for your help with all my late afternoon, frequent “special package requests.”

To the “older” PhD-room crew, Hlin Kvartsberg, Simon Sjödin, Josef Panee, and Karl Hansson; for the wonderful introduction to the Mölndal practical routines (which I still need occasional reminders about), help with finding stuff, and always being there to answer my many administrative questions.

To the “younger” PhD students, Claudia Cicognola, Karolina Minta, Elena Camporesi, Eleni Gkanatsiou, Fani Pujol, Juan Lantero Rodriguez, Johanna Nilsson, Faisal Hayat Nazir, Maya Arvidsson Rådestig; for great company and lunch conversations.

To Karolina (again), for making sure my Polish does not deteriorate too quickly.  
To Katarina Tamazin, for wonderful conversations and laughter.

To my current and previous coworkers:

To Patrick Wehrli, for bringing some sanity when the world seemed to have turned upside down.

To Katie Stringer, for great work together, and all the fun times.

To Dimitri Brinet, for fun memories, and great advice which has stuck with me.

To Ibrahim Kaya, for all the great work we did together.

To Yasmine Iacone, for the learning we did together over those few months.

To Jasmine Chebli and Tugce Satir; for always making me feel so welcome when coming to Sahlgrenska, for fun discussions early on a Monday morning (never...) or late on a weekend...

I would like to express deep gratitude to all of our collaborators:

To Prof. Carsten Hopf, for the opportunity to visit your lab, and Thomas Enzlein for all the help and for showing me around Mannheim.

To Prof. Frances Edwards, for the stimulating scientific discussions and the great ongoing work.

To Dr. Tammarny Lashley, for entrusting me with your amazing samples.

To Prof. Per Hammarström, Prof. Peter KP Nilsson, and Dr. Sofie Nyström; for all the great work and for showing me around during my visit.

To Prof. Anders Meibom, for the opportunity to visit your lab, and to Dr. Stephane Escrig, for your help with analysis, everything you taught me during my visit, and for all the great conversations.

To Dr. Stina Syvänen and Dr. Dag Sehlin; for all the great work, fantastic samples, and wonderful conversations on multiple occasions.



To Prof. Peter Sjövall, Dr. Louise Carlred and Dr. Jonas Hannestad; for great work together.

To Dr. Giulia Zanni, for all the wonderful work, samples and all the discussions.

Thank you to all the current and former CCI Staff for all the collaborative work and help over the years.

To Julia Fernandez-Rodriguez, for all your understanding and flexibility around our work.

To Carolina Tängemo, Maria Smedh, and Joanna Pylvänäinen; for all your help and the great time together when imaging was no longer in focus.

To Anna Pielach and Massimo Micaroni; for all your help with urgent processing and all your teaching along the way.

To Rafael Camacho; for all the help with hypothetical “what if” experiments and your help with ongoing work.

I would like to thank my dear friend Rakesh Banote, for all the scientific discussions during coffee breaks, all the patience you have with my occasional over excitement, and for those memorable lunches and dinners had, and those we will certainly have in the future.

I would like to thank Silvio Meier, my dear “bro”, for all the discussions, runs, wonderful trips and the fantastic times together due to our mutual understanding of one another. Also, thank you for teaching me to ski, even if I look silly.

I would like to thank Laurent Guerard, a collaborator and friend for all the work we did together, for all the fun we had, regardless of whether we were in Finland or Sweden, and for always answering my coding questions.

I would like to thank Rolf Ekman, for introducing me to the “brain smart” concept and the work with actual brain chemistry. For your fantastic attitude, positive mindset, guidance, the thought-stimulating discussions, not in the least during our occasional trips down to Halmstad.

I thank all my friends from outside of work:

To my best college buddies Kai and Paco, who still think I am unemployed and traveling the world, rather than completing my PhD. For our great trips!

To Omar for our long discussions, tens of km long “London sightseeing” walking breaks, your undefeated attitude, and still believing I am curing the world.

To Oscar, Filip, Chisco and Daniel, for making sure that work does not get in the way of health and fitness.

To Britta and Ole, Kadri and Martin, Koit and Elina, Andreea and Johannes, for listening to me ramble on about what surely appears to be nonsense over many dinners and lunches. I appreciate your patience, smiles and nodding in supposed agreement to my most recent theory.

To Adrian, you are the best friend I could ever wish for.

To Calli, for your calming effect (on your sister) and for being the perfect accomplice.

To my wonderful family, my fantastic parents Monika and Piotr, without whom I would have never even dreamt of writing this thesis. For their love and understanding, constant support, motivation, and the occasional push when my momentum was slowing down. You have provided me with the childhood many can only wish they had, the most exciting education I could ever imagine and tremendous opportunities that make me believe that dreams are only the beginning.

To my brothers, Bartek and Jakub, for always keeping me on my toes and making sure I don't take myself too seriously. Bartek, I thank you both for the unlimited rounds of board games and correcting me whenever possible. Jakub, I thank you for your unlimited energy and extreme love.

To my grandparents, aunts and uncles who helped raise me, and to my and cousins, Dziękuję za wszystkie uściski i pocałunki, bajki na dobranoc (bez przeskakiwania stron), wspólne śpiewanie i rymowanie, pierogi jagodowe oraz ogólnie za wszystko.

To Cerisa, thank you for always being supportive, making sure I don't get too lazy, that I stay focused and develop as a person and researcher every day. We are a great team, but you are the fantastic part of it!

## REFERENCES

- 1 Burns, A. & Iliffe, S. Alzheimer's disease. *BMJ* **338**, doi:10.1136/bmj.b158 (2009).
- 2 Blennow, K., de Leon, M. J. & Zetterberg, H. Alzheimer's disease. *The Lancet* **368**, 387-403, doi:10.1016/S0140-6736(06)69113-7 (2006).
- 3 2016 Alzheimer's disease facts and figures. *Alzheimer's & dementia : the journal of the Alzheimer's Association* **12**, 459-509 (2016).
- 4 Vina, J. & Lloret, A. Why women have more Alzheimer's disease than men: gender and mitochondrial toxicity of amyloid-beta peptide. *Journal of Alzheimer's disease : JAD* **20 Suppl 2**, S527-533, doi:10.3233/jad-2010-100501 (2010).
- 5 Bredesen, D. E., Rao, R. V. & Mehlen, P. Cell death in the nervous system. *Nature* **443**, 796-802, doi:10.1038/nature05293 (2006).
- 6 Hartl, F. U. & Hayer-Hartl, M. Converging concepts of protein folding in vitro and in vivo. *Nature structural & molecular biology* **16**, 574-581, doi:10.1038/nsmb.1591 (2009).
- 7 Ross, C. A. & Poirier, M. A. Protein aggregation and neurodegenerative disease. *Nature medicine* **10 Suppl**, S10-17, doi:10.1038/nm1066 (2004).
- 8 Serpell, L. C., Sunde, M. & Blake, C. C. The molecular basis of amyloidosis. *Cellular and molecular life sciences : CMLS* **53**, 871-887 (1997).
- 9 Glenner, G. G. Amyloid Deposits and Amyloidosis. *New England Journal of Medicine* **302**, 1283-1292, doi:10.1056/nejm198006053022305 (1980).
- 10 Westermark, P. *et al.* A primer of amyloid nomenclature. *Amyloid : the international journal of experimental and clinical investigation : the official journal of the International Society of Amyloidosis* **14**, 179-183, doi:10.1080/13506120701460923 (2007).
- 11 Münch, G. Alzheimer the man. *EMBO Reports* **4**, 930-930, doi:10.1038/sj.embor.embor950 (2003).
- 12 Alzheimer, A., Stelzmann, R. A., Schnitzlein, H. N. & Murtagh, F. R. An English translation of Alzheimer's 1907 paper, "Über eine eigenartige Erkrankung der Hirnrinde". *Clinical anatomy (New York, N.Y.)* **8**, 429-431, doi:10.1002/ca.980080612 (1995).
- 13 Kraepelin, E. *Psychiatrie.: Ein Lehrbuch für Studierende und Ärzte.* (J. A. Barth, 1913).
- 14 Koedam, E. L. *et al.* Early-versus late-onset Alzheimer's disease: more than age alone. *Journal of Alzheimer's disease : JAD* **19**, 1401-1408, doi:10.3233/jad-2010-1337 (2010).
- 15 Barker, W. W. *et al.* Relative frequencies of Alzheimer disease, Lewy body, vascular and frontotemporal dementia, and hippocampal sclerosis in the State of Florida Brain Bank. *Alzheimer disease and associated disorders* **16**, 203-212 (2002).
- 16 Hodges, J. R. Alzheimer's centennial legacy: origins, landmarks and the current status of knowledge concerning cognitive aspects. *Brain : a journal of neurology* **129**, 2811-2822, doi:10.1093/brain/awl275 (2006).

- 17 Blennow, K. & Wallin, A. Clinical heterogeneity of probable Alzheimer's  
disease. *J Geriatr Psychiatry Neurol* **5**, 106-113 (1992).
- 18 Mirra, S. S. *et al.* The Consortium to Establish a Registry for Alzheimer's  
Disease (CERAD). Part II. Standardization of the neuropathologic  
assessment of Alzheimer's disease. *Neurology* **41**, 479-486 (1991).
- 19 Morris, J. C. *et al.* The Consortium to Establish a Registry for Alzheimer's  
Disease (CERAD). Part I. Clinical and neuropsychological assessment of  
Alzheimer's disease. *Neurology* **39**, 1159-1165 (1989).
- 20 Folstein, M. F., Folstein, S. E. & McHugh, P. R. "Mini-mental state". *Journal  
of Psychiatric Research* **12**, 189-198, doi:[http://dx.doi.org/10.1016/0022-  
3956\(75\)90026-6](http://dx.doi.org/10.1016/0022-3956(75)90026-6) (1975).
- 21 Hughes, C. P., Berg, L., Danziger, W. L., Coben, L. A. & Martin, R. L. A  
new clinical scale for the staging of dementia. *The British journal of  
psychiatry : the journal of mental science* **140**, 566-572 (1982).
- 22 BLESSED, G., TOMLINSON, B. E. & ROTH, M. The Association Between  
Quantitative Measures of Dementia and of Senile Change in the Cerebral  
Grey Matter of Elderly Subjects. *The British Journal of Psychiatry* **114**, 797-  
811, doi:10.1192/bjp.114.512.797 (1968).
- 23 McKhann, G. *et al.* Clinical diagnosis of Alzheimer's disease: report of the  
NINCDS-ADRDA Work Group under the auspices of Department of Health  
and Human Services Task Force on Alzheimer's Disease. *Neurology* **34**, 939-  
944 (1984).
- 24 *DSM-IV-TR.* (American Psychiatric Association, 2000).
- 25 Blennow, K., Zetterberg, H. & Fagan, A. M. Fluid biomarkers in Alzheimer  
disease. *Cold Spring Harbor perspectives in medicine* **2**, a006221,  
doi:10.1101/cshperspect.a006221 (2012).
- 26 Tapiola, T. *et al.* Cerebrospinal fluid {beta}-amyloid 42 and tau proteins as  
biomarkers of Alzheimer-type pathologic changes in the brain. *Archives of  
neurology* **66**, 382-389, doi:10.1001/archneurol.2008.596 (2009).
- 27 Snider, B. J. *et al.* Cerebrospinal fluid biomarkers and rate of cognitive  
decline in very mild dementia of the Alzheimer type. *Archives of neurology*  
**66**, 638-645, doi:10.1001/archneurol.2009.55 (2009).
- 28 Samgard, K. *et al.* Cerebrospinal fluid total tau as a marker of Alzheimer's  
disease intensity. *International journal of geriatric psychiatry* **25**, 403-410,  
doi:10.1002/gps.2353 (2010).
- 29 Blom, E. S. *et al.* Rapid progression from mild cognitive impairment to  
Alzheimer's disease in subjects with elevated levels of tau in cerebrospinal  
fluid and the APOE epsilon4/epsilon4 genotype. *Dementia and geriatric  
cognitive disorders* **27**, 458-464, doi:10.1159/000216841 (2009).
- 30 Buerger, K. *et al.* CSF phosphorylated tau protein correlates with neocortical  
neurofibrillary pathology in Alzheimer's disease. *Brain : a journal of  
neurology* **129**, 3035-3041, doi:10.1093/brain/awl269 (2006).
- 31 Strozzyk, D., Blennow, K., White, L. R. & Launer, L. J. CSF Aβ<sub>42</sub> levels  
correlate with amyloid-neuropathology in a population-based autopsy study.  
*Neurology* **60**, 652-656 (2003).

- 32 Hampel, H. *et al.* Blood-based biomarkers for Alzheimer disease: mapping the road to the clinic. *Nat Rev Neurol* **14**, 639-652, doi:10.1038/s41582-018-0079-7 (2018).
- 33 Scahill, R. I., Schott, J. M., Stevens, J. M., Rossor, M. N. & Fox, N. C. Mapping the evolution of regional atrophy in Alzheimer's disease: unbiased analysis of fluid-registered serial MRI. *Proceedings of the National Academy of Sciences of the United States of America* **99**, 4703-4707, doi:10.1073/pnas.052587399 (2002).
- 34 Killiany, R. J. *et al.* MRI measures of entorhinal cortex vs hippocampus in preclinical AD. *Neurology* **58**, 1188-1196 (2002).
- 35 Dickerson, B. C. *et al.* MRI-derived entorhinal and hippocampal atrophy in incipient and very mild Alzheimer's disease. *Neurobiology of aging* **22**, 747-754 (2001).
- 36 Lajoie, I. *et al.* Application of calibrated fMRI in Alzheimer's disease. *NeuroImage. Clinical* **15**, 348-358, doi:10.1016/j.nicl.2017.05.009 (2017).
- 37 Nordberg, A., Rinne, J. O., Kadir, A. & Langstrom, B. The use of PET in Alzheimer disease. *Nat Rev Neurol* **6**, 78-87 (2010).
- 38 Jagust, W. *et al.* SPECT perfusion imaging in the diagnosis of Alzheimer's disease: a clinical-pathologic study. *Neurology* **56**, 950-956 (2001).
- 39 Holman, B. L., Johnson, K. A., Gerada, B., Carvalho, P. A. & Satlin, A. The scintigraphic appearance of Alzheimer's disease: a prospective study using technetium-99m-HMPAO SPECT. *Journal of nuclear medicine : official publication, Society of Nuclear Medicine* **33**, 181-185 (1992).
- 40 Johnson, K. A., Fox, N. C., Sperling, R. A. & Klunk, W. E. Brain Imaging in Alzheimer Disease. *Cold Spring Harbor perspectives in medicine* **2**, a006213, doi:10.1101/cshperspect.a006213 (2012).
- 41 Herholz, K., Carter, S. F. & Jones, M. Positron emission tomography imaging in dementia. *The British journal of radiology* **80 Spec No 2**, S160-167, doi:10.1259/bjr/97295129 (2007).
- 42 Klunk, W. E. *et al.* Imaging brain amyloid in Alzheimer's disease with Pittsburgh Compound-B. *Annals of neurology* **55**, 306-319, doi:10.1002/ana.20009 (2004).
- 43 Adamczuk, K. *et al.* Amyloid imaging in cognitively normal older adults: comparison between (18)F-flutemetamol and (11)C-Pittsburgh compound B. *European journal of nuclear medicine and molecular imaging* **43**, 142-151, doi:10.1007/s00259-015-3156-9 (2016).
- 44 Nelissen, N. *et al.* Phase I study of the Pittsburgh compound B derivative 18F-flutemetamol in healthy volunteers and patients with probable Alzheimer disease. *Journal of nuclear medicine : official publication, Society of Nuclear Medicine* **50**, 1251-1259, doi:10.2967/jnumed.109.063305 (2009).
- 45 Serrano-Pozo, A., Frosch, M. P., Masliah, E. & Hyman, B. T. Neuropathological alterations in Alzheimer disease. *Cold Spring Harbor perspectives in medicine* **1**, a006189, doi:10.1101/cshperspect.a006189 (2011).
- 46 Grundke-Iqbal, I. *et al.* Abnormal phosphorylation of the microtubule-associated protein tau (tau) in Alzheimer cytoskeletal pathology. *Proc Natl Acad Sci U S A* **83**, 4913-4917 (1986).

- 47 Glenner, G. G. & Wong, C. W. Alzheimer's disease: initial report of the  
purification and characterization of a novel cerebrovascular amyloid protein.  
*Biochemical and biophysical research communications* **120**, 885-890 (1984).
- 48 Hardy, J. & Allsop, D. Amyloid deposition as the central event in the  
aetiology of Alzheimer's disease. *Trends Pharmacol Sci* **12**, 383-388 (1991).
- 49 Selkoe, D. J. The molecular pathology of Alzheimer's disease. *Neuron* **6**, 487-  
498 (1991).
- 50 Howie, A. J. & Brewer, D. B. Optical properties of amyloid stained by Congo  
red: history and mechanisms. *Micron (Oxford, England : 1993)* **40**, 285-301,  
doi:10.1016/j.micron.2008.10.002 (2009).
- 51 Dickson, T. C. & Vickers, J. C. The morphological phenotype of beta-  
amyloid plaques and associated neuritic changes in Alzheimer's disease.  
*Neuroscience* **105**, 99-107 (2001).
- 52 Urbanc, B. *et al.* Neurotoxic effects of thioflavin S-positive amyloid deposits  
in transgenic mice and Alzheimer's disease. *Proceedings of the National  
Academy of Sciences of the United States of America* **99**, 13990-13995,  
doi:10.1073/pnas.222433299 (2002).
- 53 Vehmas, A. K., Kawas, C. H., Stewart, W. F. & Troncoso, J. C. Immune  
reactive cells in senile plaques and cognitive decline in Alzheimer's disease.  
*Neurobiology of aging* **24**, 321-331 (2003).
- 54 Dickson, D. W. *et al.* Identification of normal and pathological aging in  
prospectively studied nondemented elderly humans. *Neurobiol Aging* **13**,  
179-189 (1992).
- 55 Bitan, G. *et al.* Amyloid beta -protein (Abeta) assembly: Abeta 40 and Abeta  
42 oligomerize through distinct pathways. *Proceedings of the National  
Academy of Sciences of the United States of America* **100**, 330-335,  
doi:10.1073/pnas.222681699 (2003).
- 56 McGowan, E. *et al.* Abeta42 is essential for parenchymal and vascular  
amyloid deposition in mice. *Neuron* **47**, 191-199,  
doi:10.1016/j.neuron.2005.06.030 (2005).
- 57 Iwatsubo, T. *et al.* Visualization of A beta 42(43) and A beta 40 in senile  
plaques with end-specific A beta monoclonals: evidence that an initially  
deposited species is A beta 42(43). *Neuron* **13**, 45-53 (1994).
- 58 Iwatsubo, T., Saido, T. C., Mann, D. M., Lee, V. M. & Trojanowski, J. Q.  
Full-length amyloid-beta (1-42(43)) and amino-terminally modified and  
truncated amyloid-beta 42(43) deposit in diffuse plaques. *Am J Pathol* **149**,  
1823-1830 (1996).
- 59 Kim, J. *et al.* Aβ40 Inhibits Amyloid Deposition In Vivo. *The Journal of  
Neuroscience* **27**, 627-633, doi:10.1523/jneurosci.4849-06.2007 (2007).
- 60 Kumar-Singh, S. *et al.* Dense-core plaques in Tg2576 and PSAPP mouse  
models of Alzheimer's disease are centered on vessel walls. *Am J Pathol* **167**,  
527-543, doi:10.1016/s0002-9440(10)62995-1 (2005).
- 61 Roher, A. E. *et al.* beta-Amyloid-(1-42) is a major component of  
cerebrovascular amyloid deposits: implications for the pathology of  
Alzheimer disease. *Proceedings of the National Academy of Sciences of the  
United States of America* **90**, 10836-10840 (1993).

- 62 LaFerla, F. M., Green, K. N. & Oddo, S. Intracellular amyloid-[beta] in  
Alzheimer's disease. *Nat Rev Neurosci* **8**, 499-509 (2007).
- 63 Friedrich, R. P. *et al.* Mechanism of amyloid plaque formation suggests an  
intracellular basis of Abeta pathogenicity. *Proceedings of the National  
Academy of Sciences of the United States of America* **107**, 1942-1947,  
doi:10.1073/pnas.0904532106 (2010).
- 64 Brettschneider, J., Tredici, K. D., Lee, V. M. Y. & Trojanowski, J. Q.  
Spreading of pathology in neurodegenerative diseases: a focus on human  
studies. *Nat Rev Neurosci* **16**, 109-120, doi:10.1038/nrn3887 (2015).
- 65 Braak, H. & Braak, E. Neuropathological staging of Alzheimer-related  
changes. *Acta neuropathologica* **82**, 239-259 (1991).
- 66 Jucker, M. & Walker, L. C. Self-propagation of pathogenic protein aggregates  
in neurodegenerative diseases. *Nature* **501**, 45-51, doi:10.1038/nature12481  
(2013).
- 67 Thal, D. R., Rub, U., Orantes, M. & Braak, H. Phases of A beta-deposition in  
the human brain and its relevance for the development of AD. *Neurology* **58**,  
1791-1800 (2002).
- 68 Chow, V. W., Mattson, M. P., Wong, P. C. & Gleichmann, M. An Overview  
of APP Processing Enzymes and Products. *Neuromolecular medicine* **12**, 1-  
12, doi:10.1007/s12017-009-8104-z (2010).
- 69 Kummer, M. P. & Heneka, M. T. Truncated and modified amyloid-beta  
species. *Alzheimer's Research & Therapy* **6**, 28-28, doi:10.1186/alzrt258  
(2014).
- 70 Reinhard, C., Hebert, S. S. & De Strooper, B. The amyloid-beta precursor  
protein: integrating structure with biological function. *Embo j* **24**, 3996-4006,  
doi:10.1038/sj.emboj.7600860 (2005).
- 71 Yoshikai, S., Sasaki, H., Doh-ura, K., Furuya, H. & Sakaki, Y. Genomic  
organization of the human amyloid beta-protein precursor gene. *Gene* **87**,  
257-263, doi:10.1016/0378-1119(90)90310-n (1990).
- 72 Kang, J. *et al.* The precursor of Alzheimer's disease amyloid A4 protein  
resembles a cell-surface receptor. *Nature* **325**, 733-736,  
doi:10.1038/325733a0 (1987).
- 73 Shariati, S. A. & De Strooper, B. Redundancy and divergence in the amyloid  
precursor protein family. *FEBS Lett* **587**, 2036-2045,  
doi:10.1016/j.febslet.2013.05.026 (2013).
- 74 van der Kant, R. & Goldstein, L. S. Cellular functions of the amyloid  
precursor protein from development to dementia. *Dev Cell* **32**, 502-515,  
doi:10.1016/j.devcel.2015.01.022 (2015).
- 75 Choy, R. W.-Y., Cheng, Z. & Schekman, R. Amyloid precursor protein (APP)  
traffics from the cell surface via endosomes for amyloid  $\beta$  (A $\beta$ ) production in  
the  $\rightarrow$ -Golgi network. *Proceedings of the National Academy  
of Sciences* **109**, E2077-E2082, doi:10.1073/pnas.1208635109 (2012).
- 76 Thinakaran, G. & Koo, E. H. Amyloid precursor protein trafficking,  
processing, and function. *J Biol Chem* **283**, 29615-29619,  
doi:10.1074/jbc.R800019200 (2008).



- 77 Haass, C., Kaether, C., Thinakaran, G. & Sisodia, S. Trafficking and proteolytic processing of APP. *Cold Spring Harb Perspect Med* **2**, a006270, doi:10.1101/cshperspect.a006270 (2012).
- 78 O'Brien, R. J. & Wong, P. C. Amyloid precursor protein processing and Alzheimer's disease. *Annu Rev Neurosci* **34**, 185-204, doi:10.1146/annurev-neuro-061010-113613 (2011).
- 79 Chow, V. W., Mattson, M. P., Wong, P. C. & Gleichmann, M. An overview of APP processing enzymes and products. *Neuromolecular Med* **12**, 1-12, doi:10.1007/s12017-009-8104-z (2010).
- 80 Allinson, T. M., Parkin, E. T., Turner, A. J. & Hooper, N. M. ADAMs family members as amyloid precursor protein alpha-secretases. *J Neurosci Res* **74**, 342-352, doi:10.1002/jnr.10737 (2003).
- 81 Zhu, G. *et al.* Protein kinase C epsilon suppresses Abeta production and promotes activation of alpha-secretase. *Biochem Biophys Res Commun* **285**, 997-1006, doi:10.1006/bbrc.2001.5273 (2001).
- 82 Kim, T., Hinton, D. J. & Choi, D.-S. Protein kinase C-regulated a $\beta$  production and clearance. *International journal of Alzheimer's disease* **2011**, 857368-857368, doi:10.4061/2011/857368 (2011).
- 83 Vassar, R. & Citron, M. Abeta-generating enzymes: recent advances in beta- and gamma-secretase research. *Neuron* **27**, 419-422 (2000).
- 84 Vassar, R., Kovacs, D. M., Yan, R. & Wong, P. C. The beta-secretase enzyme BACE in health and Alzheimer's disease: regulation, cell biology, function, and therapeutic potential. *The Journal of neuroscience : the official journal of the Society for Neuroscience* **29**, 12787-12794, doi:10.1523/JNEUROSCI.3657-09.2009 (2009).
- 85 Cole, S. L. & Vassar, R. The Alzheimer's disease beta-secretase enzyme, BACE1. *Molecular neurodegeneration* **2**, 22-22, doi:10.1186/1750-1326-2-22 (2007).
- 86 Farzan, M., Schnitzler, C. E., Vasilieva, N., Leung, D. & Choe, H. BACE2, a  $\beta$ -secretase homolog, cleaves at the  $\beta$  site and within the amyloid- $\beta$  region of the amyloid- $\beta$  precursor protein. *Proceedings of the National Academy of Sciences* **97**, 9712-9717, doi:10.1073/pnas.160115697 (2000).
- 87 Solans, A., Estivill, X. & de La Luna, S. A new aspartyl protease on 21q22.3, BACE2, is highly similar to Alzheimer's amyloid precursor protein beta-secretase. *Cytogenet Cell Genet* **89**, 177-184, doi:10.1159/000015608 (2000).
- 88 Zhang, X. & Song, W. The role of APP and BACE1 trafficking in APP processing and amyloid- $\beta$  generation. *Alzheimer's Research & Therapy* **5**, 46, doi:10.1186/alzrt211 (2013).
- 89 Hook, V. *et al.* Inhibition of cathepsin B reduces beta-amyloid production in regulated secretory vesicles of neuronal chromaffin cells: evidence for cathepsin B as a candidate beta-secretase of Alzheimer's disease. *Biol Chem* **386**, 931-940, doi:10.1515/bc.2005.108 (2005).
- 90 Cataldo, A. M., Thayer, C. Y., Bird, E. D., Wheelock, T. R. & Nixon, R. A. Lysosomal proteinase antigens are prominently localized within senile plaques of Alzheimer's disease: evidence for a neuronal origin. *Brain research* **513**, 181-192, doi:10.1016/0006-8993(90)90456-1 (1990).



- 91 Hook, G., Yu, J., Toneff, T., Kindy, M. & Hook, V. Brain pyroglutamate amyloid-beta is produced by cathepsin B and is reduced by the cysteine protease inhibitor E64d, representing a potential Alzheimer's disease therapeutic. *Journal of Alzheimer's disease : JAD* **41**, 129-149, doi:10.3233/jad-131370 (2014).
- 92 Schilling, S., Hoffmann, T., Manhart, S., Hoffmann, M. & Demuth, H. U. Glutaminyl cyclases unfold glutamyl cyclase activity under mild acid conditions. *FEBS Lett* **563**, 191-196, doi:10.1016/s0014-5793(04)00300-x (2004).
- 93 Bai, X. C. *et al.* An atomic structure of human gamma-secretase. *Nature* **525**, 212-217, doi:10.1038/nature14892 (2015).
- 94 Lu, P. *et al.* Three-dimensional structure of human gamma-secretase. *Nature* **512**, 166-170, doi:10.1038/nature13567 (2014).
- 95 Nunan, J. & Small, D. H. Regulation of APP cleavage by alpha-, beta- and gamma-secretases. *FEBS Lett* **483**, 6-10, doi:10.1016/s0014-5793(00)02076-7 (2000).
- 96 Beher, D., Wrigley, J. D., Owens, A. P. & Shearman, M. S. Generation of C-terminally truncated amyloid-beta peptides is dependent on gamma-secretase activity. *J Neurochem* **82**, 563-575, doi:10.1046/j.1471-4159.2002.00985.x (2002).
- 97 Fukumori, A. *et al.* Presenilin-dependent gamma-secretase on plasma membrane and endosomes is functionally distinct. *Biochemistry* **45**, 4907-4914, doi:10.1021/bi052412w (2006).
- 98 Page, R. M. *et al.* Generation of Abeta38 and Abeta42 is independently and differentially affected by familial Alzheimer disease-associated presenilin mutations and gamma-secretase modulation. *J Biol Chem* **283**, 677-683, doi:10.1074/jbc.M708754200 (2008).
- 99 Kong, G. K. W. *et al.* Structural Studies of the Alzheimer's Amyloid Precursor Protein Copper-binding Domain Reveal How it Binds Copper Ions. *Journal of Molecular Biology* **367**, 148-161, doi:<https://doi.org/10.1016/j.jmb.2006.12.041> (2007).
- 100 Multhaup, G. *et al.* The amyloid precursor protein of Alzheimer's disease in the reduction of copper(II) to copper(I). *Science* **271**, 1406-1409, doi:10.1126/science.271.5254.1406 (1996).
- 101 Bush, A. I. *et al.* A novel zinc(II) binding site modulates the function of the beta A4 amyloid protein precursor of Alzheimer's disease. *J Biol Chem* **268**, 16109-16112 (1993).
- 102 Duce, J. A. *et al.* Iron-export ferroxidase activity of beta-amyloid precursor protein is inhibited by zinc in Alzheimer's disease. *Cell* **142**, 857-867, doi:10.1016/j.cell.2010.08.014 (2010).
- 103 Andrew, R. J., Kellett, K. A. B., Thinakaran, G. & Hooper, N. M. A Greek Tragedy: The Growing Complexity of Alzheimer Amyloid Precursor Protein Proteolysis. *The Journal of biological chemistry* **291**, 19235-19244, doi:10.1074/jbc.R116.746032 (2016).
- 104 Zhang, Z. *et al.* Delta-secretase cleaves amyloid precursor protein and regulates the pathogenesis in Alzheimer's disease. *Nat Commun* **6**, 8762, doi:10.1038/ncomms9762 (2015).

- 105 Baranger, K. *et al.* MT5-MMP is a new pro-amyloidogenic proteinase that  
promotes amyloid pathology and cognitive decline in a transgenic mouse  
model of Alzheimer's disease. *Cell Mol Life Sci* **73**, 217-236,  
doi:10.1007/s00018-015-1992-1 (2016).
- 106 Bien, J. *et al.* The metalloprotease meprin beta generates amino terminal-  
truncated amyloid beta peptide species. *J Biol Chem* **287**, 33304-33313,  
doi:10.1074/jbc.M112.395608 (2012).
- 107 Zetterberg, H., Blennow, K. & Hansson, E. Amyloid beta and APP as  
biomarkers for Alzheimer's disease. *Experimental gerontology* **45**, 23-29,  
doi:10.1016/j.exger.2009.08.002 (2010).
- 108 He, W. & Barrow, C. J. The A beta 3-pyroglutamyl and 11-pyroglutamyl  
peptides found in senile plaque have greater beta-sheet forming and  
aggregation propensities in vitro than full-length A beta. *Biochemistry* **38**,  
10871-10877, doi:10.1021/bi990563r (1999).
- 109 Harigaya, Y. *et al.* Amyloid beta protein starting pyroglutamate at position 3  
is a major component of the amyloid deposits in the Alzheimer's disease  
brain. *Biochem Biophys Res Commun* **276**, 422-427,  
doi:10.1006/bbrc.2000.3490 (2000).
- 110 Saido, T. & Leissring, M. A. Proteolytic Degradation of Amyloid  $\beta$ -Protein.  
*Cold Spring Harbor perspectives in medicine* **2**, a006379,  
doi:10.1101/cshperspect.a006379 (2012).
- 111 Funato, H. *et al.* Quantitation of amyloid beta-protein (A beta) in the cortex  
during aging and in Alzheimer's disease. *Am J Pathol* **152**, 1633-1640 (1998).
- 112 Abramowski, D. *et al.* Dynamics of Abeta turnover and deposition in different  
beta-amyloid precursor protein transgenic mouse models following gamma-  
secretase inhibition. *The Journal of pharmacology and experimental  
therapeutics* **327**, 411-424, doi:10.1124/jpet.108.140327 (2008).
- 113 Bateman, R. J. *et al.* Human amyloid-beta synthesis and clearance rates as  
measured in cerebrospinal fluid in vivo. *Nature medicine* **12**, 856-861,  
doi:10.1038/nm1438 (2006).
- 114 Selkoe, D. J. Clearing the brain's amyloid cobwebs. *Neuron* **32**, 177-180  
(2001).
- 115 Tanzi, R. E., Moir, R. D. & Wagner, S. L. Clearance of Alzheimer's Abeta  
peptide: the many roads to perdition. *Neuron* **43**, 605-608,  
doi:10.1016/j.neuron.2004.08.024 (2004).
- 116 Mawuenyega, K. G. Decreased clearance of CNS beta-amyloid in  
Alzheimer's disease. *Science* **330**, doi:10.1126/science.1197623 (2010).
- 117 Caccamo, A., Oddo, S., Sugarman, M. C., Akbari, Y. & LaFerla, F. M. Age-  
and region-dependent alterations in Abeta-degrading enzymes: implications  
for Abeta-induced disorders. *Neurobiology of aging* **26**, 645-654,  
doi:10.1016/j.neurobiolaging.2004.06.013 (2005).
- 118 Saito, T., Takaki, Y., Iwata, N., Trojanowski, J. & Saido, T. C. Alzheimer's  
disease, neuropeptides, neuropeptidase, and amyloid-beta peptide  
metabolism. *Science of aging knowledge environment : SAGE KE* **2003**, Pe1  
(2003).
- 119 Hersh, L. B. & Rodgers, D. W. Neprilysin and amyloid beta peptide  
degradation. *Current Alzheimer research* **5**, 225-231 (2008).

- 120 Hersh, L. B. The insulysin (insulin degrading enzyme) enigma. *Cellular and molecular life sciences : CMLS* **63**, 2432-2434, doi:10.1007/s00018-006-6238-9 (2006).
- 121 Puzzo, D. *et al.* Picomolar amyloid-beta positively modulates synaptic plasticity and memory in hippocampus. *The Journal of neuroscience : the official journal of the Society for Neuroscience* **28**, 14537-14545, doi:10.1523/jneurosci.2692-08.2008 (2008).
- 122 Pearson, H. A. & Peers, C. Physiological roles for amyloid  $\beta$  peptides. *The Journal of Physiology* **575**, 5-10, doi:10.1113/jphysiol.2006.111203 (2006).
- 123 Morley, J. E. *et al.* A physiological role for amyloid-beta protein:enhancement of learning and memory. *Journal of Alzheimer's disease : JAD* **19**, 441-449, doi:10.3233/jad-2009-1230 (2010).
- 124 Murphy, M. P. & LeVine, H. Alzheimer's disease and the beta-amyloid peptide. *Journal of Alzheimer's disease : JAD* **19**, doi:10.3233/jad-2010-1231 (2010).
- 125 Jarrett, J. T., Berger, E. P. & Lansbury, P. T., Jr. The carboxy terminus of the beta amyloid protein is critical for the seeding of amyloid formation: implications for the pathogenesis of Alzheimer's disease. *Biochemistry* **32**, 4693-4697 (1993).
- 126 Tjernberg, L. O. *et al.* A molecular model of Alzheimer amyloid beta-peptide fibril formation. *The Journal of biological chemistry* **274**, 12619-12625 (1999).
- 127 Rambaran, R. N. & Serpell, L. C. Amyloid fibrils: Abnormal protein assembly. *Prion* **2**, 112-117 (2008).
- 128 Serpell, L. C. Alzheimer's amyloid fibrils: structure and assembly. *Biochimica et biophysica acta* **1502**, 16-30 (2000).
- 129 Socher, E., Sticht, H. & Horn, A. H. C. The Conformational Stability of Nonfibrillar Amyloid- $\beta$  Peptide Oligomers Critically Depends on the C-Terminal Peptide Length. *ACS Chemical Neuroscience* **5**, 161-167, doi:10.1021/cn400208r (2014).
- 130 Gazit, E. Mechanisms of amyloid fibril self-assembly and inhibition. Model short peptides as a key research tool. *The FEBS journal* **272**, 5971-5978, doi:10.1111/j.1742-4658.2005.05022.x (2005).
- 131 Cukalevski, R. *et al.* Role of Aromatic Side Chains in Amyloid  $\beta$ -Protein Aggregation. *ACS Chemical Neuroscience* **3**, 1008-1016, doi:10.1021/cn300073s (2012).
- 132 Berhanu, W. M. & Hansmann, U. H. E. Structure and Dynamics of Amyloid- $\beta$  Segmental Polymorphisms. *PLoS ONE* **7**, e41479, doi:10.1371/journal.pone.0041479 (2012).
- 133 Larini, L. & Shea, J.-E. Role of  $\beta$ -Hairpin Formation in Aggregation: The Self-Assembly of the Amyloid- $\beta$ (25-35) Peptide. *Biophysical Journal* **103**, 576-586, doi:<http://dx.doi.org/10.1016/j.bpj.2012.06.027> (2012).
- 134 Hoyer, W., Gronwall, C., Jonsson, A., Stahl, S. & Hard, T. Stabilization of a beta-hairpin in monomeric Alzheimer's amyloid-beta peptide inhibits amyloid formation. *Proceedings of the National Academy of Sciences of the United States of America* **105**, 5099-5104, doi:10.1073/pnas.0711731105 (2008).

- 135 Schmidt, M. *et al.* Comparison of Alzheimer Abeta(1-40) and Abeta(1-42)  
amyloid fibrils reveals similar protofilament structures. *Proceedings of the  
National Academy of Sciences of the United States of America* **106**, 19813-  
19818, doi:10.1073/pnas.0905007106 (2009).
- 136 Zou, Y., Li, Y., Hao, W., Hu, X. & Ma, G. Parallel  $\beta$ -Sheet Fibril and  
Antiparallel  $\beta$ -Sheet Oligomer: New Insights into Amyloid Formation of Hen  
Egg White Lysozyme under Heat and Acidic Condition from FTIR  
Spectroscopy. *The Journal of Physical Chemistry B* **117**, 4003-4013,  
doi:10.1021/jp4003559 (2013).
- 137 Glabe, C. G. Structural Classification of Toxic Amyloid Oligomers. *The  
Journal of biological chemistry* **283**, 29639-29643,  
doi:10.1074/jbc.R800016200 (2008).
- 138 Lambert, M. P. *et al.* Diffusible, nonfibrillar ligands derived from Abeta1-42  
are potent central nervous system neurotoxins. *Proceedings of the National  
Academy of Sciences of the United States of America* **95**, 6448-6453 (1998).
- 139 Gellermann, G. P. *et al.* Abeta-globulomers are formed independently of the  
fibril pathway. *Neurobiology of disease* **30**, 212-220,  
doi:10.1016/j.nbd.2008.01.010 (2008).
- 140 Song, W., Wang, Y., Colletier, J. P., Yang, H. & Xu, Y. Varied Probability  
of Staying Collapsed/Extended at the Conformational Equilibrium of  
Monomeric Abeta40 and Abeta42. *Scientific reports* **5**, 11024,  
doi:10.1038/srep11024 (2015).
- 141 Walsh, D. M. *et al.* Amyloid beta-protein fibrillogenesis. Structure and  
biological activity of protofibrillar intermediates. *The Journal of biological  
chemistry* **274**, 25945-25952 (1999).
- 142 Dong, M. *et al.* Structural and Material Properties of Amyloid Abeta40/42  
Fibrils. *Chemphyschem : a European journal of chemical physics and  
physical chemistry* **17**, 2558-2566, doi:10.1002/cphc.201600256 (2016).
- 143 Shankar, G. M. & Walsh, D. M. Alzheimer's disease: synaptic dysfunction  
and Abeta. *Molecular neurodegeneration* **4**, 48, doi:10.1186/1750-1326-4-48  
(2009).
- 144 Portelius, E. *et al.* Brain Amyloid-Beta Fragment Signatures in Pathological  
Ageing and Alzheimer's Disease by Hybrid Immunoprecipitation Mass  
Spectrometry. *Neurodegenerative Diseases* **15**, 50-57 (2015).
- 145 Moore, B. D. *et al.* Overlapping profiles of Abeta peptides in the Alzheimer's  
disease and pathological aging brains. *Alzheimers Res Ther* **4**, 18,  
doi:10.1186/alzrt121 (2012).
- 146 Wang, J., Dickson, D. W., Trojanowski, J. Q. & Lee, V. M. Y. The Levels of  
Soluble versus Insoluble Brain A $\beta$  Distinguish Alzheimer's Disease from  
Normal and Pathologic Aging. *Experimental Neurology* **158**, 328-337,  
doi:<http://dx.doi.org/10.1006/exnr.1999.7085> (1999).
- 147 Glenner, G. G. & Wong, C. W. Alzheimer's disease: Initial report of the  
purification and characterization of a novel cerebrovascular amyloid protein.  
*Biochemical and Biophysical Research Communications* **120**, 885-890,  
doi:[https://doi.org/10.1016/S0006-291X\(84\)80190-4](https://doi.org/10.1016/S0006-291X(84)80190-4) (1984).
- 148 Masters, C. L. *et al.* Amyloid plaque core protein in Alzheimer disease and  
Down syndrome. *Proceedings of the National Academy of Sciences of the*

- United States of America* **82**, 4245-4249, doi:10.1073/pnas.82.12.4245 (1985).
- 149 Hardy, J. & Higgins, G. Alzheimer's disease: the amyloid cascade hypothesis. *Science* **256**, 184-185, doi:10.1126/science.1566067 (1992).
- 150 Selkoe, D. J. Amyloid protein and Alzheimer's disease. *Scientific American* **265**, 68-71, 74-66, 78 (1991).
- 151 Beyreuther, K. & Masters, C. L. Amyloid precursor protein (APP) and beta A4 amyloid in the etiology of Alzheimer's disease: precursor-product relationships in the derangement of neuronal function. *Brain Pathol* **1**, 241-251 (1991).
- 152 Goate, A. *et al.* Segregation of a missense mutation in the amyloid precursor protein gene with familial Alzheimer's disease. *Nature* **349**, 704-706, doi:10.1038/349704a0 (1991).
- 153 Sherrington, R. *et al.* Cloning of a gene bearing missense mutations in early-onset familial Alzheimer's disease. *Nature* **375**, 754-760, doi:10.1038/375754a0 (1995).
- 154 Levy, E. *et al.* Mutation of the Alzheimer's disease amyloid gene in hereditary cerebral hemorrhage, Dutch type. *Science* **248**, 1124-1126 (1990).
- 155 Levy-Lahad, E. *et al.* Candidate gene for the chromosome 1 familial Alzheimer's disease locus. *Science* **269**, 973-977, doi:10.1126/science.7638622 (1995).
- 156 Hardy, J., Goate, A., Owen, M. & Rossor, M. Presenile dementia associated with mosaic trisomy 21 in a patient with a Down syndrome child. *Lancet (London, England)* **2**, 743, doi:10.1016/s0140-6736(89)90805-2 (1989).
- 157 Popovitch, E. R. *et al.* Alzheimer neuropathology in non-Down's syndrome mentally retarded adults. *Acta neuropathologica* **80**, 362-367 (1990).
- 158 Glenner, G. G. & Wong, C. W. Alzheimer's disease and Down's syndrome: sharing of a unique cerebrovascular amyloid fibril protein. *Biochem Biophys Res Commun* **122**, 1131-1135, doi:10.1016/0006-291x(84)91209-9 (1984).
- 159 Karran, E. & De Strooper, B. The amyloid cascade hypothesis: are we poised for success or failure? *J Neurochem* **139 Suppl 2**, 237-252, doi:10.1111/jnc.13632 (2016).
- 160 Selkoe, D. J. & Hardy, J. The amyloid hypothesis of Alzheimer's disease at 25 years. *EMBO molecular medicine* **8**, 595-608, doi:10.15252/emmm.201606210 (2016).
- 161 Corder, E. H. *et al.* Gene dose of apolipoprotein E type 4 allele and the risk of Alzheimer's disease in late onset families. *Science* **261**, 921-923, doi:10.1126/science.8346443 (1993).
- 162 Liu, C.-C., Kanekiyo, T., Xu, H. & Bu, G. Apolipoprotein E and Alzheimer disease: risk, mechanisms and therapy. *Nat Rev Neurol* **9**, 106-118 (2013).
- 163 Karran, E., Mercken, M. & De Strooper, B. The amyloid cascade hypothesis for Alzheimer's disease: an appraisal for the development of therapeutics. *Nat Rev Drug Discov* **10**, 698-712, doi:10.1038/nrd3505 (2011).
- 164 Ricciarelli, R. & Fedele, E. The Amyloid Cascade Hypothesis in Alzheimer's Disease: It's Time to Change Our Mind. *Curr Neuropharmacol* **15**, 926-935, doi:10.2174/1570159X15666170116143743 (2017).

- 165 Delaere, P. *et al.* Large amounts of neocortical beta A4 deposits without  
neuritic plaques nor tangles in a psychometrically assessed, non-demented  
person. *Neuroscience letters* **116**, 87-93, doi:10.1016/0304-3940(90)90391-l  
(1990).
- 166 Karran, E., Mercken, M. & Strooper, B. D. The amyloid cascade hypothesis  
for Alzheimer's disease: an appraisal for the development of  
therapeutics. *Nature Reviews Drug Discovery* **10**, 698, doi:10.1038/nrd3505  
(2011).
- 167 Mehta, D., Jackson, R., Paul, G., Shi, J. & Sabbagh, M. Why do trials for  
Alzheimer's disease drugs keep failing? A discontinued drug perspective for  
2010-2015. *Expert Opin Investig Drugs* **26**, 735-739,  
doi:10.1080/13543784.2017.1323868 (2017).
- 168 Esparza, T. J. *et al.* Amyloid- $\beta$  oligomerization in Alzheimer dementia versus  
high-pathology controls. *Annals of neurology* **73**, 104-119,  
doi:10.1002/ana.23748 (2013).
- 169 McLean, C. A. *et al.* Soluble pool of Abeta amyloid as a determinant of  
severity of neurodegeneration in Alzheimer's disease. *Annals of neurology*  
**46**, 860-866 (1999).
- 170 Naj, A. C., Schellenberg, G. D. & Consortium, f. t. A. s. D. G. Genomic  
variants, genes, and pathways of Alzheimer's disease: An overview.  
*American Journal of Medical Genetics Part B: Neuropsychiatric Genetics*  
**174**, 5-26, doi:10.1002/ajmg.b.32499 (2017).
- 171 Mullan, M. *et al.* A pathogenic mutation for probable Alzheimer's disease in  
the APP gene at the N-terminus of beta-amyloid. *Nature genetics* **1**, 345-347,  
doi:10.1038/ng0892-345 (1992).
- 172 Cai, X. D., Golde, T. E. & Younkin, S. G. Release of excess amyloid beta  
protein from a mutant amyloid beta protein precursor. *Science* **259**, 514-516  
(1993).
- 173 Citron, M. *et al.* Mutation of the beta-amyloid precursor protein in familial  
Alzheimer's disease increases beta-protein production. *Nature* **360**, 672-674,  
doi:10.1038/360672a0 (1992).
- 174 Kumar-Singh, S. Cerebral amyloid angiopathy: pathogenetic mechanisms  
and link to dense amyloid plaques. *Genes, brain, and behavior* **7 Suppl 1**, 67-  
82, doi:10.1111/j.1601-183X.2007.00380.x (2008).
- 175 Nilsberth, C. *et al.* The 'Arctic' APP mutation (E693G) causes Alzheimer's  
disease by enhanced Abeta protofibril formation. *Nature neuroscience* **4**, 887-  
893, doi:10.1038/nn0901-887 (2001).
- 176 Kamino, K. *et al.* Linkage and mutational analysis of familial Alzheimer  
disease kindreds for the APP gene region. *Am J Hum Genet* **51**, 998-1014  
(1992).
- 177 Eckman, C. B. *et al.* A new pathogenic mutation in the APP gene (I716V)  
increases the relative proportion of A beta 42(43). *Human molecular genetics*  
**6**, 2087-2089, doi:10.1093/hmg/6.12.2087 (1997).
- 178 De Jonghe, C. *et al.* Pathogenic APP mutations near the gamma-secretase  
cleavage site differentially affect Abeta secretion and APP C-terminal  
fragment stability. *Human molecular genetics* **10**, 1665-1671,  
doi:10.1093/hmg/10.16.1665 (2001).



- 179 Zoltowska, K. M., Maesako, M. & Berezovska, O. Interrelationship between  
Changes in the Amyloid  $\beta$  42/40 Ratio and Presenilin 1 Conformation.  
*Molecular medicine (Cambridge, Mass.)* **22**, 329-337,  
doi:10.2119/molmed.2016.00127 (2016).
- 180 Kelleher, R. J. & Shen, J. Presenilin-1 mutations and Alzheimer's disease.  
*Proceedings of the National Academy of Sciences* **114**, 629-631,  
doi:10.1073/pnas.1619574114 (2017).
- 181 Duff, K. *et al.* Increased amyloid-beta42(43) in brains of mice expressing  
mutant presenilin 1. *Nature* **383**, 710-713, doi:10.1038/383710a0 (1996).
- 182 Herl, L. *et al.* Mutations in amyloid precursor protein affect its interactions  
with presenilin/gamma-secretase. *Mol Cell Neurosci* **41**, 166-174,  
doi:10.1016/j.mcn.2009.02.008 (2009).
- 183 LaFerla, F. M. & Green, K. N. Animal models of Alzheimer disease. *Cold  
Spring Harbor perspectives in medicine* **2**, a006320,  
doi:10.1101/cshperspect.a006320 (2012).
- 184 Chin, J. in *Alzheimer's Disease and Frontotemporal Dementia: Methods and  
Protocols* (ed Erik D. Roberson) 169-189 (Humana Press, 2011).
- 185 Jankowsky, J. L. & Zheng, H. Practical considerations for choosing a mouse  
model of Alzheimer's disease. *Molecular neurodegeneration* **12**, 89,  
doi:10.1186/s13024-017-0231-7 (2017).
- 186 Jankowsky, J. L. *et al.* Rodent A beta modulates the solubility and distribution  
of amyloid deposits in transgenic mice. *J Biol Chem* **282**, 22707-22720,  
doi:10.1074/jbc.M611050200 (2007).
- 187 Pittman, A. M., Fung, H. C. & de Silva, R. Untangling the tau gene  
association with neurodegenerative disorders. *Human molecular genetics* **15  
Spec No 2**, R188-195, doi:10.1093/hmg/ddl190 (2006).
- 188 Allen, M. *et al.* Association of MAPT haplotypes with Alzheimer's disease  
risk and MAPT brain gene expression levels. *Alzheimer's Research &  
Therapy* **6**, 39, doi:10.1186/alzrt268 (2014).
- 189 Grundke-Iqbal, I. *et al.* Microtubule-associated protein tau. A component of  
Alzheimer paired helical filaments. *J Biol Chem* **261**, 6084-6089 (1986).
- 190 Arriagada, P. V., Growdon, J. H., Hedley-Whyte, E. T. & Hyman, B. T.  
Neurofibrillary tangles but not senile plaques parallel duration and severity  
of Alzheimer's disease. *Neurology* **42**, 631-639 (1992).
- 191 Bancher, C. *et al.* Accumulation of abnormally phosphorylated tau precedes  
the formation of neurofibrillary tangles in Alzheimer's disease. *Brain  
research* **477**, 90-99, doi:10.1016/0006-8993(89)91396-6 (1989).
- 192 Gotz, J. *et al.* A decade of tau transgenic animal models and beyond. *Brain  
Pathol* **17**, 91-103, doi:10.1111/j.1750-3639.2007.00051.x (2007).
- 193 Lewis, J. *et al.* Enhanced neurofibrillary degeneration in transgenic mice  
expressing mutant tau and APP. *Science* **293**, 1487-1491,  
doi:10.1126/science.1058189 (2001).
- 194 Wilcock, D. M. *et al.* Progression of amyloid pathology to Alzheimer's  
disease pathology in an amyloid precursor protein transgenic mouse model  
by removal of nitric oxide synthase 2. *J Neurosci* **28**, 1537-1545,  
doi:10.1523/jneurosci.5066-07.2008 (2008).

- 195 Oddo, S., Billings, L., Kesslak, J. P., Cribbs, D. H. & LaFerla, F. M. Abeta immunotherapy leads to clearance of early, but not late, hyperphosphorylated tau aggregates via the proteasome. *Neuron* **43**, 321-332, doi:10.1016/j.neuron.2004.07.003 (2004).
- 196 Oddo, S. *et al.* Triple-transgenic model of Alzheimer's disease with plaques and tangles: intracellular Abeta and synaptic dysfunction. *Neuron* **39**, 409-421 (2003).
- 197 Zheng, H. *et al.* Mice deficient for the amyloid precursor protein gene. *Ann N Y Acad Sci* **777**, 421-426, doi:10.1111/j.1749-6632.1996.tb34456.x (1996).
- 198 Takei, Y., Teng, J., Harada, A. & Hirokawa, N. Defects in axonal elongation and neuronal migration in mice with disrupted tau and map1b genes. *The Journal of cell biology* **150**, 989-1000, doi:10.1083/jcb.150.5.989 (2000).
- 199 Shipton, O. A. *et al.* Tau protein is required for amyloid {beta}-induced impairment of hippocampal long-term potentiation. *J Neurosci* **31**, 1688-1692, doi:10.1523/jneurosci.2610-10.2011 (2011).
- 200 Roberson, E. D. *et al.* Reducing endogenous tau ameliorates amyloid beta-induced deficits in an Alzheimer's disease mouse model. *Science* **316**, 750-754, doi:10.1126/science.1141736 (2007).
- 201 Shen, J. *et al.* Skeletal and CNS defects in Presenilin-1-deficient mice. *Cell* **89**, 629-639, doi:10.1016/s0092-8674(00)80244-5 (1997).
- 202 Herreman, A. *et al.* Presenilin 2 deficiency causes a mild pulmonary phenotype and no changes in amyloid precursor protein processing but enhances the embryonic lethal phenotype of presenilin 1 deficiency. *Proceedings of the National Academy of Sciences of the United States of America* **96**, 11872-11877, doi:10.1073/pnas.96.21.11872 (1999).
- 203 Luo, Y. *et al.* Mice deficient in BACE1, the Alzheimer's beta-secretase, have normal phenotype and abolished beta-amyloid generation. *Nature neuroscience* **4**, 231-232, doi:10.1038/85059 (2001).
- 204 Hartmann, D. *et al.* The disintegrin/metalloprotease ADAM 10 is essential for Notch signalling but not for alpha-secretase activity in fibroblasts. *Human molecular genetics* **11**, 2615-2624, doi:10.1093/hmg/11.21.2615 (2002).
- 205 Drummond, E. & Wisniewski, T. Alzheimer's disease: experimental models and reality. *Acta neuropathologica* **133**, 155-175, doi:10.1007/s00401-016-1662-x (2017).
- 206 Ransohoff, R. M. All (animal) models (of neurodegeneration) are wrong. Are they also useful? *The Journal of experimental medicine* **215**, 2955-2958, doi:10.1084/jem.20182042 (2018).
- 207 Nilsson, P., Saito, T. & Saido, T. C. New mouse model of Alzheimer's. *ACS chemical neuroscience* **5**, 499-502, doi:10.1021/cn500105p (2014).
- 208 Saito, T. *et al.* Single App knock-in mouse models of Alzheimer's disease. *Nature neuroscience* **17**, 661-663, doi:10.1038/nn.3697 (2014).
- 209 Blennow, K., de Leon, M. J. & Zetterberg, H. Alzheimer's disease. *Lancet (London, England)* **368**, 387-403, doi:10.1016/s0140-6736(06)69113-7 (2006).
- 210 Mahley, R. W. & Rall, S. C., Jr. Apolipoprotein E: far more than a lipid transport protein. *Annu Rev Genomics Hum Genet* **1**, 507-537, doi:10.1146/annurev.genom.1.1.507 (2000).



- 211 Rall, S. C., Jr., Weisgraber, K. H. & Mahley, R. W. Human apolipoprotein E.  
The complete amino acid sequence. *J Biol Chem* **257**, 4171-4178 (1982).
- 212 Weisgraber, K. H., Innerarity, T. L. & Mahley, R. W. Abnormal lipoprotein  
receptor-binding activity of the human E apoprotein due to cysteine-arginine  
interchange at a single site. *J Biol Chem* **257**, 2518-2521 (1982).
- 213 Zhong, N. & Weisgraber, K. H. Understanding the association of  
apolipoprotein E4 with Alzheimer disease: clues from its structure. *J Biol  
Chem* **284**, 6027-6031, doi:10.1074/jbc.R800009200 (2009).
- 214 Farrer, L. A. *et al.* Effects of age, sex, and ethnicity on the association  
between apolipoprotein E genotype and Alzheimer disease. A meta-analysis.  
APOE and Alzheimer Disease Meta Analysis Consortium. *Jama* **278**, 1349-  
1356 (1997).
- 215 Altmann, A., Tian, L., Henderson, V. W. & Greicius, M. D. Sex modifies the  
APOE-related risk of developing Alzheimer disease. *Annals of neurology* **75**,  
563-573, doi:10.1002/ana.24135 (2014).
- 216 Bu, G. Apolipoprotein E and its receptors in Alzheimer's disease: pathways,  
pathogenesis and therapy. *Nat Rev Neurosci* **10**, 333-344,  
doi:10.1038/nrn2620 (2009).
- 217 Namba, Y., Tomonaga, M., Kawasaki, H., Otomo, E. & Ikeda, K.  
Apolipoprotein E immunoreactivity in cerebral amyloid deposits and  
neurofibrillary tangles in Alzheimer's disease and kuru plaque amyloid in  
Creutzfeldt-Jakob disease. *Brain research* **541**, 163-166, doi:10.1016/0006-  
8993(91)91092-f (1991).
- 218 Ellis, R. J. *et al.* Cerebral amyloid angiopathy in the brains of patients with  
Alzheimer's disease: the CERAD experience, Part XV. *Neurology* **46**, 1592-  
1596, doi:10.1212/wnl.46.6.1592 (1996).
- 219 Ohm, T. G. *et al.* Apolipoprotein E polymorphism influences not only  
cerebral senile plaque load but also Alzheimer-type neurofibrillary tangle  
formation. *Neuroscience* **66**, 583-587, doi:[https://doi.org/10.1016/0306-  
4522\(94\)00596-W](https://doi.org/10.1016/0306-4522(94)00596-W) (1995).
- 220 Castellano, J. M. *et al.* Human apoE isoforms differentially regulate brain  
amyloid-beta peptide clearance. *Sci Transl Med* **3**, 89ra57,  
doi:10.1126/scitranslmed.3002156 (2011).
- 221 Reiman, E. M. *et al.* Fibrillar amyloid-beta burden in cognitively normal  
people at 3 levels of genetic risk for Alzheimer's disease. *Proceedings of the  
National Academy of Sciences of the United States of America* **106**, 6820-  
6825, doi:10.1073/pnas.0900345106 (2009).
- 222 LaDu, M. J. *et al.* Isoform-specific binding of apolipoprotein E to beta-  
amyloid. *J Biol Chem* **269**, 23403-23406 (1994).
- 223 Kim, J., Basak, J. M. & Holtzman, D. M. The role of apolipoprotein E in  
Alzheimer's disease. *Neuron* **63**, 287-303, doi:10.1016/j.neuron.2009.06.026  
(2009).
- 224 DeMattos, R. B. *et al.* ApoE and clusterin cooperatively suppress Abeta levels  
and deposition: evidence that ApoE regulates extracellular Abeta metabolism  
in vivo. *Neuron* **41**, 193-202 (2004).

- 225 Ulland, T. K. & Colonna, M. TREM2 — a key player in microglial biology  
and Alzheimer disease. *Nature Reviews Neurology* **14**, 667-675,  
doi:10.1038/s41582-018-0072-1 (2018).
- 226 Allcock, R. J., Barrow, A. D., Forbes, S., Beck, S. & Trowsdale, J. The human  
TREM gene cluster at 6p21.1 encodes both activating and inhibitory single  
IgV domain receptors and includes NKp44. *Eur J Immunol* **33**, 567-577,  
doi:10.1002/immu.200310033 (2003).
- 227 Guerreiro, R. *et al.* TREM2 Variants in Alzheimer's Disease. *New England  
Journal of Medicine* **368**, 117-127, doi:10.1056/NEJMoa1211851 (2012).
- 228 Jonsson, T. *et al.* Variant of TREM2 associated with the risk of Alzheimer's  
disease. *The New England journal of medicine* **368**, 107-116,  
doi:10.1056/NEJMoa1211103 (2013).
- 229 Chen, X. *et al.* Assessment of TREM2 rs75932628 association with  
amyotrophic lateral sclerosis in a Chinese population. *J Neurol Sci* **355**, 193-  
195, doi:10.1016/j.jns.2015.05.010 (2015).
- 230 Guerreiro, R. J. *et al.* Using exome sequencing to reveal mutations in TREM2  
presenting as a frontotemporal dementia-like syndrome without bone  
involvement. *JAMA Neurol* **70**, 78-84, doi:10.1001/jamaneurol.2013.579  
(2013).
- 231 Zheng, H. *et al.* Opposing roles of the triggering receptor expressed on  
myeloid cells 2 and triggering receptor expressed on myeloid cells-like  
transcript 2 in microglia activation. *Neurobiol Aging* **42**, 132-141,  
doi:10.1016/j.neurobiolaging.2016.03.004 (2016).
- 232 Bailey, C. C., DeVaux, L. B. & Farzan, M. The Triggering Receptor  
Expressed on Myeloid Cells 2 Binds Apolipoprotein E. *J Biol Chem* **290**,  
26033-26042, doi:10.1074/jbc.M115.677286 (2015).
- 233 Yeh, F. L., Wang, Y., Tom, I., Gonzalez, L. C. & Sheng, M. TREM2 Binds  
to Apolipoproteins, Including APOE and CLU/APOJ, and Thereby  
Facilitates Uptake of Amyloid-Beta by Microglia. *Neuron* **91**, 328-340,  
doi:10.1016/j.neuron.2016.06.015 (2016).
- 234 Daws, M. R. *et al.* Pattern recognition by TREM-2: binding of anionic  
ligands. *J Immunol* **171**, 594-599, doi:10.4049/jimmunol.171.2.594 (2003).
- 235 Atagi, Y. *et al.* Apolipoprotein E Is a Ligand for Triggering Receptor  
Expressed on Myeloid Cells 2 (TREM2). *J Biol Chem* **290**, 26043-26050,  
doi:10.1074/jbc.M115.679043 (2015).
- 236 Zhao, Y. *et al.* TREM2 Is a Receptor for beta-Amyloid that Mediates  
Microglial Function. *Neuron* **97**, 1023-1031.e1027,  
doi:10.1016/j.neuron.2018.01.031 (2018).
- 237 Mazaheri, F. *et al.* TREM2 deficiency impairs chemotaxis and microglial  
responses to neuronal injury. *EMBO reports* **18**, 1186-1198,  
doi:10.15252/embr.201743922 (2017).
- 238 Poliani, P. L. *et al.* TREM2 sustains microglial expansion during aging and  
response to demyelination. *J Clin Invest* **125**, 2161-2170,  
doi:10.1172/jci77983 (2015).
- 239 Wang, Y. *et al.* TREM2 lipid sensing sustains the microglial response in an  
Alzheimer's disease model. *Cell* **160**, 1061-1071,  
doi:10.1016/j.cell.2015.01.049 (2015).

- 240 Wang, Y. *et al.* TREM2-mediated early microglial response limits diffusion  
and toxicity of amyloid plaques. *J. Exp. Med.* **213**, 667-675,  
doi:10.1084/jem.20151948 (2016).
- 241 Wunderlich, P. *et al.* Sequential proteolytic processing of the triggering  
receptor expressed on myeloid cells-2 (TREM2) protein by ectodomain  
shedding and gamma-secretase-dependent intramembranous cleavage. *J Biol*  
*Chem* **288**, 33027-33036, doi:10.1074/jbc.M113.517540 (2013).
- 242 Liu, D. *et al.* Soluble TREM2 changes during the clinical course of  
Alzheimer's disease: A meta-analysis. *Neuroscience letters* **686**, 10-16,  
doi:10.1016/j.neulet.2018.08.038 (2018).
- 243 Colonna, M. & Wang, Y. TREM2 variants: new keys to decipher Alzheimer  
disease pathogenesis. *Nat Rev Neurosci* **17**, 201-207, doi:10.1038/nrn.2016.7  
(2016).
- 244 Nebel, R. A. *et al.* Understanding the impact of sex and gender in Alzheimer's  
disease: A call to action. *Alzheimer's & dementia : the journal of the*  
*Alzheimer's Association* **14**, 1171-1183, doi:10.1016/j.jalz.2018.04.008  
(2018).
- 245 Kukull, W. A. *et al.* Dementia and Alzheimer disease incidence: a prospective  
cohort study. *Arch Neurol* **59**, 1737-1746, doi:10.1001/archneur.59.11.1737  
(2002).
- 246 Guo, X. *et al.* Blood pressure components and changes in relation to white  
matter lesions: a 32-year prospective population study. *Hypertension* **54**, 57-  
62, doi:10.1161/hypertensionaha.109.129700 (2009).
- 247 Solomon, A., Kivipelto, M., Wolozin, B., Zhou, J. & Whitmer, R. A. Midlife  
serum cholesterol and increased risk of Alzheimer's and vascular dementia  
three decades later. *Dementia and geriatric cognitive disorders* **28**, 75-80,  
doi:10.1159/000231980 (2009).
- 248 Li, J. *et al.* Vascular risk factors promote conversion from mild cognitive  
impairment to Alzheimer disease. *Neurology* **76**, 1485-1491,  
doi:10.1212/WNL.0b013e318217e7a4 (2011).
- 249 Jellinger, K. A. Head injury and dementia. *Curr Opin Neurol* **17**, 719-723  
(2004).
- 250 Mayeux, R. & Stern, Y. Epidemiology of Alzheimer disease. *Cold Spring*  
*Harb Perspect Med* **2**, doi:10.1101/cshperspect.a006239 (2012).
- 251 Foley, P. Lipids in Alzheimer's disease: A century-old story. *Biochimica et*  
*biophysica acta* **1801**, 750-753, doi:10.1016/j.bbaliip.2010.05.004 (2010).
- 252 Di Paolo, G. & Kim, T.-W. Linking Lipids to Alzheimer's Disease:  
Cholesterol and Beyond. *Nat. Rev. Neurosci.* **12**, 284-296,  
doi:10.1038/nrn3012 (2011).
- 253 Hartmann, T., Kuchenbecker, J. & Grimm, M. O. Alzheimer's disease: the  
lipid connection. *J Neurochem* **103 Suppl 1**, 159-170, doi:10.1111/j.1471-  
4159.2007.04715.x (2007).
- 254 Dietschy, J. M. & Turley, S. D. Cholesterol metabolism in the brain. *Curr*  
*Opin Lipidol* **12**, 105-112 (2001).
- 255 Chan, R. B. *et al.* Comparative Lipidomic Analysis of Mouse and Human  
Brain with Alzheimer Disease. *Journal of Biological Chemistry* **287**, 2678-  
2688, doi:10.1074/jbc.M111.274142 (2012).

- 256 Puglielli, L. *et al.* Acyl-coenzyme A: cholesterol acyltransferase modulates  
the generation of the amyloid beta-peptide. *Nature cell biology* **3**, 905-912,  
doi:10.1038/ncb1001-905 (2001).
- 257 Bhattacharyya, R. & Kovacs, D. M. ACAT inhibition and amyloid beta  
reduction. *Biochimica et biophysica acta* **1801**, 960-965,  
doi:10.1016/j.bbaliip.2010.04.003 (2010).
- 258 Chang, T. Y., Chang, C. C., Ohgami, N. & Yamauchi, Y. Cholesterol sensing,  
trafficking, and esterification. *Annu Rev Cell Dev Biol* **22**, 129-157,  
doi:10.1146/annurev.cellbio.22.010305.104656 (2006).
- 259 Tall, A. R. Cholesterol efflux pathways and other potential mechanisms  
involved in the athero-protective effect of high density lipoproteins. *J Intern  
Med* **263**, 256-273, doi:10.1111/j.1365-2796.2007.01898.x (2008).
- 260 Vetrivel, K. S. & Thinakaran, G. Membrane rafts in Alzheimer's disease beta-  
amyloid production. *Biochimica et biophysica acta* **1801**, 860-867,  
doi:10.1016/j.bbaliip.2010.03.007 (2010).
- 261 Kalvodova, L. *et al.* Lipids as modulators of proteolytic activity of BACE:  
involvement of cholesterol, glycosphingolipids, and anionic phospholipids in  
vitro. *J Biol Chem* **280**, 36815-36823, doi:10.1074/jbc.M504484200 (2005).
- 262 Osawa, S. *et al.* Phosphoinositides suppress gamma-secretase in both the  
detergent-soluble and -insoluble states. *J Biol Chem* **283**, 19283-19292,  
doi:10.1074/jbc.M705954200 (2008).
- 263 Osenkowski, P., Ye, W., Wang, R., Wolfe, M. S. & Selkoe, D. J. Direct and  
potent regulation of gamma-secretase by its lipid microenvironment. *J Biol  
Chem* **283**, 22529-22540, doi:10.1074/jbc.M801925200 (2008).
- 264 Di Paolo, G. & Kim, T. W. Linking lipids to Alzheimer's disease: cholesterol  
and beyond. *Nat Rev Neurosci* **12**, 284-296, doi:10.1038/nrn3012 (2011).
- 265 He, X., Huang, Y., Li, B., Gong, C. X. & Schuchman, E. H. Deregulation of  
sphingolipid metabolism in Alzheimer's disease. *Neurobiol Aging* **31**, 398-  
408, doi:10.1016/j.neurobiolaging.2008.05.010 (2010).
- 266 Puglielli, L., Ellis, B. C., Saunders, A. J. & Kovacs, D. M. Ceramide stabilizes  
beta-site amyloid precursor protein-cleaving enzyme 1 and promotes amyloid  
beta-peptide biogenesis. *J Biol Chem* **278**, 19777-19783,  
doi:10.1074/jbc.M300466200 (2003).
- 267 Grimm, M. O. *et al.* Regulation of cholesterol and sphingomyelin metabolism  
by amyloid-beta and presenilin. *Nature cell biology* **7**, 1118-1123,  
doi:10.1038/ncb1313 (2005).
- 268 Sawamura, N. *et al.* Modulation of amyloid precursor protein cleavage by  
cellular sphingolipids. *J Biol Chem* **279**, 11984-11991,  
doi:10.1074/jbc.M309832200 (2004).
- 269 Yanagisawa, K. Role of gangliosides in Alzheimer's disease. *Biochimica et  
biophysica acta* **1768**, 1943-1951, doi:10.1016/j.bbamem.2007.01.018  
(2007).
- 270 Ariga, T., McDonald, M. P. & Yu, R. K. Role of ganglioside metabolism in  
the pathogenesis of Alzheimer's disease--a review. *Journal of lipid research*  
**49**, 1157-1175, doi:10.1194/jlr.R800007-JLR200 (2008).

- 271 Matsuzaki, K., Kato, K. & Yanagisawa, K. Abeta polymerization through  
interaction with membrane gangliosides. *Biochimica et biophysica acta* **1801**,  
868-877, doi:10.1016/j.bbailip.2010.01.008 (2010).
- 272 Kracun, I., Kalanj, S., Talan-Hranilovic, J. & Cosovic, C. Cortical distribution  
of gangliosides in Alzheimer's disease. *Neurochemistry International* **20**,  
433-438, doi:[https://doi.org/10.1016/0197-0186\(92\)90058-Y](https://doi.org/10.1016/0197-0186(92)90058-Y) (1992).
- 273 Ariga, T. *et al.* Characterization of high-affinity binding between  
gangliosides and amyloid beta-protein. *Arch Biochem Biophys* **388**, 225-230,  
doi:10.1006/abbi.2001.2304 (2001).
- 274 McLaurin, J., Franklin, T., Fraser, P. E. & Chakrabartty, A. Structural  
transitions associated with the interaction of Alzheimer beta-amyloid  
peptides with gangliosides. *J Biol Chem* **273**, 4506-4515 (1998).
- 275 Yanagisawa, K., Odaka, A., Suzuki, N. & Ihara, Y. GM1 ganglioside-bound  
amyloid beta-protein (A beta): a possible form of preamyloid in Alzheimer's  
disease. *Nature medicine* **1**, 1062-1066 (1995).
- 276 Kakio, A., Nishimoto, S. I., Yanagisawa, K., Kozutsumi, Y. & Matsuzaki, K.  
Cholesterol-dependent formation of GM1 ganglioside-bound amyloid beta-  
protein, an endogenous seed for Alzheimer amyloid. *J Biol Chem* **276**, 24985-  
24990, doi:10.1074/jbc.M100252200 (2001).
- 277 Fernandez-Perez, E. J., Sepulveda, F. J., Peoples, R. & Aguayo, L. G. Role  
of membrane GM1 on early neuronal membrane actions of Abeta during  
onset of Alzheimer's disease. *Biochim Biophys Acta Mol Basis Dis* **1863**,  
3105-3116, doi:10.1016/j.bbadis.2017.08.013 (2017).
- 278 Matsuoka, Y. *et al.* Novel therapeutic approach for the treatment of  
Alzheimer's disease by peripheral administration of agents with an affinity to  
beta-amyloid. *J Neurosci* **23**, 29-33 (2003).
- 279 Yamaguchi, T. *et al.* Expression of B4GALNT1, an essential  
glycosyltransferase for the synthesis of complex gangliosides, suppresses  
BACE1 degradation and modulates APP processing. *Scientific reports* **6**,  
34505-34505, doi:10.1038/srep34505 (2016).
- 280 Oikawa, N. *et al.* Gangliosides determine the amyloid pathology of  
Alzheimer's disease. *Neuroreport* **20**, 1043-1046,  
doi:10.1097/WNR.0b013e32832e4b9d (2009).
- 281 Bernardo, A. *et al.* Elimination of GD3 synthase improves memory and  
reduces amyloid-beta plaque load in transgenic mice. *Neurobiol Aging* **30**,  
1777-1791, doi:10.1016/j.neurobiolaging.2007.12.022 (2009).
- 282 Petanceska, S. S. & Gandy, S. The phosphatidylinositol 3-kinase inhibitor  
wortmannin alters the metabolism of the Alzheimer's amyloid precursor  
protein. *J Neurochem* **73**, 2316-2320, doi:10.1046/j.1471-  
4159.1999.0732316.x (1999).
- 283 Haugabook, S. J. *et al.* Reduction of Abeta accumulation in the Tg2576  
animal model of Alzheimer's disease after oral administration of the  
phosphatidylinositol kinase inhibitor wortmannin. *Faseb j* **15**, 16-18,  
doi:10.1096/fj.00-0528fje (2001).
- 284 Landman, N. *et al.* Presenilin mutations linked to familial Alzheimer's disease  
cause an imbalance in phosphatidylinositol 4,5-bisphosphate metabolism.

- Proceedings of the National Academy of Sciences of the United States of America* **103**, 19524-19529, doi:10.1073/pnas.0604954103 (2006).
- 285 Yoo, A. S. *et al.* Presenilin-mediated modulation of capacitative calcium entry. *Neuron* **27**, 561-572 (2000).
- 286 Oliveira, T. G. & Di Paolo, G. Phospholipase D in brain function and Alzheimer's disease. *Biochimica et biophysica acta* **1801**, 799-805, doi:10.1016/j.bbaliip.2010.04.004 (2010).
- 287 Cai, D. *et al.* Phospholipase D1 corrects impaired betaAPP trafficking and neurite outgrowth in familial Alzheimer's disease-linked presenilin-1 mutant neurons. *Proceedings of the National Academy of Sciences of the United States of America* **103**, 1936-1940, doi:10.1073/pnas.0510710103 (2006).
- 288 Cai, D. *et al.* Presenilin-1 uses phospholipase D1 as a negative regulator of beta-amyloid formation. *Proceedings of the National Academy of Sciences of the United States of America* **103**, 1941-1946, doi:10.1073/pnas.0510708103 (2006).
- 289 Stephenson, D. T., Lemere, C. A., Selkoe, D. J. & Clemens, J. A. Cytosolic phospholipase A2 (cPLA2) immunoreactivity is elevated in Alzheimer's disease brain. *Neurobiology of disease* **3**, 51-63, doi:10.1006/nbdi.1996.0005 (1996).
- 290 Sundaram, J. R. *et al.* Cdk5/p25-induced cytosolic PLA2-mediated lysophosphatidylcholine production regulates neuroinflammation and triggers neurodegeneration. *J Neurosci* **32**, 1020-1034, doi:10.1523/jneurosci.5177-11.2012 (2012).
- 291 Malaplate-Armand, C. *et al.* Soluble oligomers of amyloid-beta peptide induce neuronal apoptosis by activating a cPLA2-dependent sphingomyelinase-ceramide pathway. *Neurobiology of disease* **23**, 178-189, doi:10.1016/j.nbd.2006.02.010 (2006).
- 292 Prasad, M. R., Lovell, M. A., Yatin, M., Dhillon, H. & Markesbery, W. R. Regional membrane phospholipid alterations in Alzheimer's disease. *Neurochemical research* **23**, 81-88 (1998).
- 293 Cole, G. M., Ma, Q. L. & Frautschy, S. A. Omega-3 fatty acids and dementia. *Prostaglandins Leukot Essent Fatty Acids* **81**, 213-221, doi:10.1016/j.plefa.2009.05.015 (2009).
- 294 Xu, D. *et al.* Increased arachidonic acid-containing phosphatidylcholine is associated with reactive microglia and astrocytes in the spinal cord after peripheral nerve injury. *Scientific reports* **6**, 26427, doi:10.1038/srep26427 (2016).
- 295 Sanchez-Mejia, R. O. & Mucke, L. Phospholipase A2 and arachidonic acid in Alzheimer's disease. *Biochimica et biophysica acta* **1801**, 784-790, doi:10.1016/j.bbaliip.2010.05.013 (2010).
- 296 Schneider, C., Porter, N. A. & Brash, A. R. Routes to 4-hydroxynonenal: fundamental issues in the mechanisms of lipid peroxidation. *J Biol Chem* **283**, 15539-15543, doi:10.1074/jbc.R800001200 (2008).
- 297 Bush, A. I. & Tanzi, R. E. Therapeutics for Alzheimer's disease based on the metal hypothesis. *Neurotherapeutics* **5**, 421-432, doi:10.1016/j.nurt.2008.05.001 (2008).



- 298 Masliah, E., Terry, R. D., Mallory, M., Alford, M. & Hansen, L. A. Diffuse  
plaques do not accentuate synapse loss in Alzheimer's disease. *The American  
journal of pathology* **137**, 1293-1297 (1990).
- 299 Lord, A. *et al.* Observations in APP bitransgenic mice suggest that diffuse  
and compact plaques form via independent processes in Alzheimer's disease.  
*Am J Pathol* **178**, 2286-2298, doi:10.1016/j.ajpath.2011.01.052 (2011).
- 300 Toyama, B. H. & Weissman, J. S. Amyloid structure: conformational  
diversity and consequences. *Annual review of biochemistry* **80**, 557-585,  
doi:10.1146/annurev-biochem-090908-120656 (2011).
- 301 Fändrich, M. *et al.* Amyloid fibril polymorphism: a challenge for molecular  
imaging and therapy. *J Intern Med* **283**, 218-237, doi:10.1111/joim.12732  
(2018).
- 302 Hammarström, P. Photonic amyloids. *Nature Photonics* **13**, 442-444,  
doi:10.1038/s41566-019-0471-x (2019).
- 303 Rasmussen, J. *et al.* Amyloid polymorphisms constitute distinct clouds of  
conformational variants in different etiological subtypes of Alzheimer's  
disease. *Proceedings of the National Academy of Sciences of the United States  
of America* **114**, 13018-13023, doi:10.1073/pnas.1713215114 (2017).
- 304 Tywoniuk, B. *et al.* Amyloid Fibril Design: Limiting Structural  
Polymorphism in Alzheimer's A $\beta$  Protofilaments. *J Phys Chem B* **122**, 11535-  
11545, doi:10.1021/acs.jpcc.8b07423 (2018).
- 305 Lu, J. X. *et al.* Molecular structure of beta-amyloid fibrils in Alzheimer's  
disease brain tissue. *Cell* **154**, 1257-1268, doi:10.1016/j.cell.2013.08.035  
(2013).
- 306 Gremer, L. *et al.* Fibril structure of amyloid-beta(1-42) by cryo-electron  
microscopy. *Science* **358**, 116-119, doi:10.1126/science.aao2825 (2017).
- 307 Qiang, W., Yau, W. M., Lu, J. X., Collinge, J. & Tycko, R. Structural  
variation in amyloid-beta fibrils from Alzheimer's disease clinical subtypes.  
*Nature* **541**, 217-221, doi:10.1038/nature20814 (2017).
- 308 Paduch, M. *et al.* Generating conformation-specific synthetic antibodies to  
trap proteins in selected functional states. *Methods* **60**, 3-14,  
doi:10.1016/j.jymeth.2012.12.010 (2013).
- 309 Perchiacca, J. M., Ladiwala, A. R. A., Bhattacharya, M. & Tessier, P. M.  
Structure-based design of conformation- and sequence-specific antibodies  
against amyloid  $\beta$ . *Proceedings of the National Academy of Sciences of the  
United States of America* **109**, 84-89, doi:10.1073/pnas.1111232108 (2012).
- 310 Leclerc, M. Optical and Electrochemical Transducers Based on  
Functionalized Conjugated Polymers. *Sensors Update* **8**, 21-38,  
doi:10.1002/1616-8984(200011)8:1<21::AID-SEUP21>3.0.CO;2-B (2000).
- 311 Klingstedt, T. *et al.* Luminescent conjugated oligothiophenes for sensitive  
fluorescent assignment of protein inclusion bodies. *Chembiochem* **14**, 607-  
616, doi:10.1002/cbic.201200731 (2013).
- 312 Nystrom, S. *et al.* Evidence for age-dependent in vivo conformational  
rearrangement within A $\beta$  amyloid deposits. *ACS Chem Biol* **8**, 1128-1133,  
doi:10.1021/cb4000376 (2013).

- 313 Magnusson, K. *et al.* Multimodal fluorescence microscopy of prion strain  
specific PrP deposits stained by thiophene-based amyloid ligands. *Prion* **8**,  
319-329, doi:10.4161/pri.29239 (2014).
- 314 Portelius, E. *et al.* Mass spectrometric characterization of brain amyloid beta  
isoform signatures in familial and sporadic Alzheimer's disease. *Acta*  
*neuropathologica* **120**, 185-193, doi:10.1007/s00401-010-0690-1 (2010).
- 315 Portelius, E. *et al.* Brain amyloid-beta fragment signatures in pathological  
ageing and Alzheimer's disease by hybrid immunoprecipitation mass  
spectrometry. *Neurodegener Dis* **15**, 50-57, doi:10.1159/000369465 (2015).
- 316 Portelius, E. *et al.* Characterization of amyloid beta peptides in cerebrospinal  
fluid by an automated immunoprecipitation procedure followed by mass  
spectrometry. *Journal of proteome research* **6**, 4433-4439,  
doi:10.1021/pr0703627 (2007).
- 317 Hornak, J. P. *Encyclopedia of imaging science and technology.* (J. Wiley,  
2002).
- 318 Airy, G. B. *On the Diffraction of an Object-glass with Circular Aperture:  
From the Transactions of the Cambridge Philosophical Society, Vol. V.*  
(Printed at the Pitt Press by John Smith, 1835).
- 319 Rayleigh. XXXI. Investigations in optics, with special reference to the  
spectroscope. *The London, Edinburgh, and Dublin Philosophical Magazine*  
*and Journal of Science* **8**, 261-274, doi:10.1080/14786447908639684 (1879).
- 320 Guenther, R. D. *Modern Optics.* (Wiley, 1990).
- 321 Minsky, M. Memoir on inventing the confocal scanning microscope.  
*Scanning* **10**, 128-138, doi:10.1002/sca.4950100403 (1988).
- 322 Pawley, J. *Handbook of Biological Confocal Microscopy.* (Springer US,  
2013).
- 323 Klingstedt, T. *et al.* Synthesis of a library of oligothiophenes and their  
utilization as fluorescent ligands for spectral assignment of protein  
aggregates. *Org Biomol Chem* **9**, 8356-8370, doi:10.1039/c1ob05637a  
(2011).
- 324 Klingstedt, T. *et al.* The structural basis for optimal performance of  
oligothiophene-based fluorescent amyloid ligands: conformational flexibility  
is essential for spectral assignment of a diversity of protein aggregates.  
*Chemistry* **19**, 10179-10192, doi:10.1002/chem.201301463 (2013).
- 325 Simon, R. A. *et al.* Pentameric thiophene-based ligands that spectrally  
discriminate amyloid- $\beta$  and tau aggregates display distinct solvatochromism  
and viscosity-induced spectral shifts. *Chemistry (Weinheim an der*  
*Bergstrasse, Germany)* **20**, 12537-12543, doi:10.1002/chem.201402890  
(2014).
- 326 Shirani, H. *et al.* Synthesis of Thiophene-Based Optical Ligands That  
Selectively Detect Tau Pathology in Alzheimer's Disease. *Chemistry* **23**,  
17127-17135, doi:10.1002/chem.201703846 (2017).
- 327 Nilsson, K. P. Small organic probes as amyloid specific ligands--past and  
recent molecular scaffolds. *FEBS Lett* **583**, 2593-2599,  
doi:10.1016/j.febslet.2009.04.016 (2009).



- 328 Schutz, A. K. *et al.* The amyloid-Congo red interface at atomic resolution. *Angew Chem Int Ed Engl* **50**, 5956-5960, doi:10.1002/anie.201008276 (2011).
- 329 Michno, W. *et al.* Multimodal Chemical Imaging of Amyloid Plaque Polymorphism Reveals Abeta Aggregation Dependent Anionic Lipid Accumulations and Metabolism. *Analytical chemistry* **90**, 8130-8138, doi:10.1021/acs.analchem.8b01361 (2018).
- 330 Freundlich, M. M. Origin of the Electron Microscope. *Science* **142**, 185-188 (1963).
- 331 Knoll, M. & Ruska, E. Das Elektronenmikroskop. *Zeitschrift für Physik* **78**, 318-339, doi:10.1007/bf01342199 (1932).
- 332 Egerton, R. *Physical Principles of Electron Microscopy: An Introduction to TEM, SEM, and AEM.* (Springer US, 2011).
- 333 Williams, D. B. & Carter, C. B. *Transmission Electron Microscopy: A Textbook for Materials Science.* (Springer, 2009).
- 334 Winey, M., Meehl, J. B., O'Toole, E. T. & Giddings, T. H., Jr. Conventional transmission electron microscopy. *Mol Biol Cell* **25**, 319-323, doi:10.1091/mbc.E12-12-0863 (2014).
- 335 Crewe, A. V., Wall, J. & Langmore, J. Visibility of Single Atoms. *Science* **168**, 1338-1340, doi:10.1126/science.168.3937.1338 (1970).
- 336 Chandler, D. E. & Roberson, R. W. *Bioimaging: Current Concepts in Light and Electron Microscopy.* (Jones and Bartlett Publishers, 2009).
- 337 Allen, T. D. *Introduction to Electron Microscopy for Biologists.* (Elsevier Science, 2008).
- 338 Finck, H. Epoxy resins in electron microscopy. *J Biophys Biochem Cytol* **7**, 27-30, doi:10.1083/jcb.7.1.27 (1960).
- 339 Newman, G. R. & Hobot, J. A. Resins for Combined Light and Electron Microscopy: A Half Century of Development. *The Histochemical Journal* **31**, 495-505, doi:10.1023/a:1003850921869 (1999).
- 340 Luft, J. H. Improvements in epoxy resin embedding methods. *J Biophys Biochem Cytol* **9**, 409-414, doi:10.1083/jcb.9.2.409 (1961).
- 341 Spurr, A. R. A low-viscosity epoxy resin embedding medium for electron microscopy. *J Ultrastruct Res* **26**, 31-43 (1969).
- 342 Thorpe, J. R. The application of LR gold resin for immunogold labeling. *Methods Mol Biol* **117**, 99-110, doi:10.1385/1-59259-201-5:99 (1999).
- 343 Newman, G. R. & Hobot, J. A. Modern acrylics for post-embedding immunostaining techniques. *Journal of Histochemistry & Cytochemistry* **35**, 971-981, doi:10.1177/35.9.3302021 (1987).
- 344 Acetarin, J.-D., Carlemalm, E. & Villiger, W. Developments of new Lowicryl® resins for embedding biological specimens at even lower temperatures. *Journal of Microscopy* **143**, 81-88, doi:10.1111/j.1365-2818.1986.tb02766.x (1986).
- 345 Gordon, R. E. in *Histopathology: Methods and Protocols* (ed Christina E. Day) 119-135 (Springer New York, 2014).
- 346 Brorson, S. H. & Skjorten, F. Improved technique for immunoelectron microscopy. How to prepare epoxy resin to obtain approximately the same

- immunogold labeling for epoxy sections as for acrylic sections without any etching. *Micron* **27**, 211-217 (1996).
- 347 Skepper, J. N. & Powell, J. M. Immunogold Staining of Epoxy Resin Sections for Transmission Electron Microscopy (TEM). *CSH Protoc* **2008**, pdb.prot5015, doi:10.1101/pdb.prot5015 (2008).
- 348 Misell, D. L. & Brown, E. B. *Electron diffraction: an introduction for biologists*. (Elsevier, 1987).
- 349 Seligman, A. M., Wasserkrug, H. L. & Hanker, J. S. A new staining method (OTO) for enhancing contrast of lipid--containing membranes and droplets in osmium tetroxide--fixed tissue with osmiophilic thiocarbohydrazide(TCH). *The Journal of cell biology* **30**, 424-432, doi:10.1083/jcb.30.2.424 (1966).
- 350 Venable, J. H. & Coggeshall, R. A SIMPLIFIED LEAD CITRATE STAIN FOR USE IN ELECTRON MICROSCOPY. *The Journal of cell biology* **25**, 407-408, doi:10.1083/jcb.25.2.407 (1965).
- 351 Watson, M. L. Staining of tissue sections for electron microscopy with heavy metals. *J Biophys Biochem Cytol* **4**, 475-478, doi:10.1083/jcb.4.4.475 (1958).
- 352 Faulk, W. P. & Taylor, G. M. An immunocolloid method for the electron microscope. *Immunochemistry* **8**, 1081-1083 (1971).
- 353 Maranto, A. R. Neuronal mapping: a photooxidation reaction makes Lucifer yellow useful for electron microscopy. *Science* **217**, 953-955, doi:10.1126/science.7112109 (1982).
- 354 Adams, Stephen R. *et al.* Multicolor Electron Microscopy for Simultaneous Visualization of Multiple Molecular Species. *Cell Chemical Biology* **23**, 1417-1427, doi:<https://doi.org/10.1016/j.chembiol.2016.10.006> (2016).
- 355 Ekman, R. *et al.* *Mass Spectrometry: Instrumentation, Interpretation, and Applications*. (Wiley, 2008).
- 356 Karas, M. & Hillenkamp, F. Laser desorption ionization of proteins with molecular masses exceeding 10,000 daltons. *Analytical chemistry* **60**, 2299-2301, doi:10.1021/ac00171a028 (1988).
- 357 Tanaka, K. *et al.* Protein and polymer analyses up to m/z 100 000 by laser ionization time-of-flight mass spectrometry. *Rapid Communications in Mass Spectrometry* **2**, 151-153, doi:10.1002/rcm.1290020802 (1988).
- 358 Tucher, J., Somasundaram, P. & Tholey, A. in *Advances in MALDI and Laser-Induced Soft Ionization Mass Spectrometry* (ed Rainer Cramer) 77-90 (Springer International Publishing, 2016).
- 359 Strupat, K., Karas, M. & Hillenkamp, F. 2,5-Dihydroxybenzoic acid: a new matrix for laser desorption—ionization mass spectrometry. *International Journal of Mass Spectrometry and Ion Processes* **111**, 89-102, doi:[https://doi.org/10.1016/0168-1176\(91\)85050-V](https://doi.org/10.1016/0168-1176(91)85050-V) (1991).
- 360 Weinberger, S., Boernsen, O., W Finchy, J., Robertson, V. & Musselman, B. AN EVALUATION OF CRYSTALLIZATION METHODS FOR MATRIX-ASSISTED, LASER DESORPTION / IONIZATION OF PROTEINS. (1993).
- 361 Dai, Y., Whittal, R. M. & Li, L. Two-Layer Sample Preparation: A Method for MALDI-MS Analysis of Complex Peptide and Protein Mixtures. *Analytical Chemistry* **71**, 1087-1091, doi:10.1021/ac980684h (1999).

- 362 Xiang, F., Beavis, R. C. & Ens, W. A method to increase contaminant tolerance in protein matrix-assisted laser desorption/ionization by the fabrication of thin protein-doped polycrystalline films. *Rapid Communications in Mass Spectrometry* **8**, 199-204, doi:10.1002/rcm.1290080215 (1994).
- 363 Li, L., Golding, R. E. & Whittall, R. M. Analysis of Single Mammalian Cell Lysates by Mass Spectrometry. *Journal of the American Chemical Society* **118**, 11662-11663, doi:10.1021/ja9627499 (1996).
- 364 Hensel, R. R., King, R. C. & Owens, K. G. Electrospray sample preparation for improved quantitation in matrix-assisted laser desorption/ionization time-of-flight mass spectrometry. *Rapid Commun Mass Spectrom* **11**, 1785-1793, doi:10.1002/(sici)1097-0231(19971030)11:16<1785::Aid-rcm78>3.0.Co;2-q (1997).
- 365 Haddleton, D., Waterson, C. & Derrick, P. Comment: A simple, low-cost, air-spray method for improved sample preparation for matrix-assisted laser desorption/ionisation mass spectrometry of derivatised poly(ethylene glycol). *European Mass Spectrometry - EUR MASS SPECTROM* **4**, doi:10.1255/ejms.211 (1998).
- 366 Paine, M. R. L. *et al.* Mass Spectrometry Imaging with Isomeric Resolution Enabled by Ozone-Induced Dissociation. *Angewandte Chemie (International ed. in English)* **57**, 10530-10534, doi:10.1002/anie.201802937 (2018).
- 367 Soltwisch, J. *et al.* Mass spectrometry imaging with laser-induced postionization. *Science* **348**, 211-215, doi:10.1126/science.aaa1051 (2015).
- 368 Spivey, E. C., McMillen, J. C., Ryan, D. J., Spraggins, J. M. & Caprioli, R. M. Combining MALDI-2 and transmission geometry laser optics to achieve high sensitivity for ultra-high spatial resolution surface analysis. *Journal of Mass Spectrometry* **54**, 366-370, doi:10.1002/jms.4335 (2019).
- 369 Laiko, V. V., Baldwin, M. A. & Burlingame, A. L. Atmospheric pressure matrix-assisted laser desorption/ionization mass spectrometry. *Analytical chemistry* **72**, 652-657, doi:10.1021/ac990998k (2000).
- 370 Wu, K. J. & Odom, R. W. Matrix-enhanced secondary ion mass spectrometry: a method for molecular analysis of solid surfaces. *Analytical chemistry* **68**, 873-882, doi:10.1021/ac950717i (1996).
- 371 Delcorte, A. Matrix-enhanced secondary ion mass spectrometry: The Alchemist's solution? *Applied Surface Science* **252**, 6582-6587, doi:<https://doi.org/10.1016/j.apsusc.2006.02.076> (2006).
- 372 Svara, F. N., Kiss, A., Jaskolla, T. W., Karas, M. & Heeren, R. M. High-reactivity matrices increase the sensitivity of matrix enhanced secondary ion mass spectrometry. *Analytical chemistry* **83**, 8308-8313, doi:10.1021/ac202222h (2011).
- 373 Nunez, J., Renslow, R., Cliff, J. B., 3rd & Anderton, C. R. NanoSIMS for biological applications: Current practices and analyses. *Biointerphases* **13**, 03b301, doi:10.1116/1.4993628 (2017).
- 374 Van der Heide, P. *Secondary Ion Mass Spectrometry: An Introduction to Principles and Practices*. (John Wiley & Sons, Incorporated, 2014).

- 375 Wolff, M. M. & Stephens, W. E. A Pulsed Mass Spectrometer with Time  
Dispersion. *Review of Scientific Instruments* **24**, 616-617,  
doi:10.1063/1.1770801 (1953).
- 376 Wiley, W. C. & McLaren, I. H. Time-of-Flight Mass Spectrometer with  
Improved Resolution. *Review of Scientific Instruments* **26**, 1150-1157,  
doi:10.1063/1.1715212 (1955).
- 377 Mamyrin, B. A., Karataev, V. I., Shmikk, D. V. & Zagulin, V. A. Mass  
reflection: a new nonmagnetic time-of-flight high resolution mass-  
spectrometer. *Zh. Eksp. Teor. Fiz.* **64**: No. 1, 82-89(Jan 1973). Medium: X  
(1973).
- 378 Boxer, S. G., Kraft, M. L. & Weber, P. K. Advances in imaging secondary  
ion mass spectrometry for biological samples. *Annu Rev Biophys* **38**, 53-74,  
doi:10.1146/annurev.biophys.050708.133634 (2009).
- 379 Mattauch, J. A Double-Focusing Mass Spectrograph and the Masses of <sup>15</sup>N  
and <sup>18</sup>O. *Physical Review* **50**, 617-623, doi:10.1103/PhysRev.50.617 (1936).
- 380 Thomson, J. J. *Rays of Positive Electricity and Their Application to Chemical  
Analyses*. (Longmans, Green and Company, 1913).
- 381 Dempster, A. J. A new Method of Positive Ray Analysis. *Physical Review*  
**11**, 316-325, doi:10.1103/PhysRev.11.316 (1918).
- 382 Hanrieder, J., Phan, N. T. N., Kurczy, M. E. & Ewing, A. G. Imaging Mass  
Spectrometry in Neuroscience. *ACS Chemical Neuroscience* **4**, 666-679,  
doi:10.1021/cn400053c (2013).
- 383 Vickerman, J. C. Molecular imaging and depth profiling by mass  
spectrometry--SIMS, MALDI or DESI? *The Analyst* **136**, 2199-2217,  
doi:10.1039/c1an00008j (2011).
- 384 Michno, W., Wehrli, P. M., Blennow, K., Zetterberg, H. & Hanrieder, J.  
Molecular imaging mass spectrometry for probing protein dynamics in  
neurodegenerative disease pathology. *Journal of neurochemistry*,  
doi:10.1111/jnc.14559 (2018).
- 385 Kooijman, P. C. *et al.* Increased throughput and ultra-high mass resolution in  
DESI FT-ICR MS imaging through new-generation external data acquisition  
system and advanced data processing approaches. *Scientific reports* **9**, 8,  
doi:10.1038/s41598-018-36957-1 (2019).
- 386 Caprioli, R. M., Farmer, T. B. & Gile, J. Molecular Imaging of Biological  
Samples: Localization of Peptides and Proteins Using MALDI-TOF MS.  
*Analytical Chemistry* **69**, 4751-4760, doi:10.1021/ac970888i (1997).
- 387 Stoekli, M., Staab, D., Wetzel, M. & Brechbuehl, M. iMatrixSpray: a free  
and open source sample preparation device for mass spectrometric imaging.  
*Chimia (Aarau)* **68**, 146-149, doi:10.2533/chimia.2014.146 (2014).
- 388 Hankin, J. A., Barkley, R. M. & Murphy, R. C. Sublimation as a method of  
matrix application for mass spectrometric imaging. *Journal of the American  
Society for Mass Spectrometry* **18**, 1646-1652,  
doi:10.1016/j.jasms.2007.06.010 (2007).
- 389 Yang, J. & Caprioli, R. M. Matrix Sublimation/Recrystallization for Imaging  
Proteins by Mass Spectrometry at High Spatial Resolution. *Analytical  
Chemistry* **83**, 5728-5734, doi:10.1021/ac200998a (2011).

- 390 Huizing, L. R. S. *et al.* Development and evaluation of matrix application techniques for high throughput mass spectrometry imaging of tissues in the clinic. *Clinical Mass Spectrometry* **12**, 7-15, doi:<https://doi.org/10.1016/j.clinms.2019.01.004> (2019).
- 391 Peteranderl, R. & Lechene, C. Measure of carbon and nitrogen stable isotope ratios in cultured cells. *Journal of the American Society for Mass Spectrometry* **15**, 478-485, doi:10.1016/j.jasms.2003.11.019 (2004).
- 392 Ong, S.-E. *et al.* Stable Isotope Labeling by Amino Acids in Cell Culture, SILAC, as a Simple and Accurate Approach to Expression Proteomics. *Molecular & Cellular Proteomics* **1**, 376-386, doi:10.1074/mcp.M200025-MCP200 (2002).
- 393 McClatchy, D. B. & Yates, J. R., 3rd. Stable Isotope Labeling of Mammals (SILAM). *CSH Protoc* **2008**, pdb.prot4940, doi:10.1101/pdb.prot4940 (2008).
- 394 Ong, S.-E. & Mann, M. A practical recipe for stable isotope labeling by amino acids in cell culture (SILAC). *Nature Protocols* **1**, 2650-2660, doi:10.1038/nprot.2006.427 (2006).
- 395 Bendall, S. C. *et al.* Prevention of amino acid conversion in SILAC experiments with embryonic stem cells. *Molecular & cellular proteomics : MCP* **7**, 1587-1597, doi:10.1074/mcp.M800113-MCP200 (2008).
- 396 Geiger, T. *et al.* Use of stable isotope labeling by amino acids in cell culture as a spike-in standard in quantitative proteomics. *Nature Protocols* **6**, 147, doi:10.1038/nprot.2010.192 (2011).
- 397 Schwanhäusser, B., Gossen, M., Dittmar, G. & Selbach, M. Global analysis of cellular protein translation by pulsed SILAC. *PROTEOMICS* **9**, 205-209, doi:10.1002/pmic.200800275 (2009).
- 398 Merrill, A. E. *et al.* NeuCode labels for relative protein quantification. *Molecular & cellular proteomics : MCP* **13**, 2503-2512, doi:10.1074/mcp.M114.040287 (2014).
- 399 Hebert, A. S. *et al.* Neutron-encoded mass signatures for multiplexed proteome quantification. *Nat Methods* **10**, 332-334, doi:10.1038/nmeth.2378 (2013).
- 400 Kaboord, B. & Perr, M. Isolation of proteins and protein complexes by immunoprecipitation. *Methods Mol Biol* **424**, 349-364, doi:10.1007/978-1-60327-064-9\_27 (2008).
- 401 Lin, J. S. & Lai, E. M. Protein-Protein Interactions: Co-Immunoprecipitation. *Methods Mol Biol* **1615**, 211-219, doi:10.1007/978-1-4939-7033-9\_17 (2017).
- 402 Emon, J. M. v. *Immunoassay and Other Bioanalytical Techniques*. (Taylor & Francis, 2007).
- 403 Price, C. P. & Newman, D. J. *Principles and Practice of Immunoassay*. (Palgrave Macmillan UK, 1991).
- 404 Matos, L. L. d., Trufelli, D. C., de Matos, M. G. L. & da Silva Pinhal, M. A. Immunohistochemistry as an important tool in biomarkers detection and clinical practice. *Biomark Insights* **5**, 9-20 (2010).

- 405 Kim, S.-W., Roh, J. & Park, C.-S. Immunohistochemistry for Pathologists:  
Protocols, Pitfalls, and Tips. *J Pathol Transl Med* **50**, 411-418,  
doi:10.4132/jptm.2016.08.08 (2016).
- 406 Buchwalow, I. B. & Böcker, W. *Immunohistochemistry: Basics and Methods*.  
(Springer Berlin Heidelberg, 2010).
- 407 Jackson, J. E. A user's guide to principal components. *John Willey & Sons*,  
*New York* (1991).
- 408 Eriksson, L., Byrne, T., Johansson, E., Trygg, J. & Vikström, C. *Multi- and  
Megavariate Data Analysis Basic Principles and Applications*. (Umetrics  
Academy, 2013).
- 409 Wold, H. O. A. Estimation of principal components and related models by  
iterative least squares. *Multivariate analysis*, 391-420 (1966).
- 410 Wold, S., Ruhe, A., Wold, H. & W. J. Dunn, I. The Collinearity Problem in  
Linear Regression. The Partial Least Squares (PLS) Approach to Generalized  
Inverses. *SIAM Journal on Scientific and Statistical Computing* **5**, 735-743,  
doi:10.1137/0905052 (1984).
- 411 Bylesjö, M. *et al.* OPLS discriminant analysis: combining the strengths of  
PLS-DA and SIMCA classification. *Journal of Chemometrics* **20**, 341-351,  
doi:10.1002/cem.1006 (2006).
- 412 Trygg, J. & Wold, S. Orthogonal projections to latent structures (O-PLS).  
*Journal of Chemometrics* **16**, 119-128, doi:10.1002/cem.695 (2002).
- 413 Xu, D. & Tian, Y. A Comprehensive Survey of Clustering Algorithms.  
*Annals of Data Science* **2**, 165-193, doi:10.1007/s40745-015-0040-1 (2015).
- 414 Nikhare, N. B. & Prasad, P. S. in *2018 2nd International Conference on  
Inventive Systems and Control (ICISC)*. 215-217.
- 415 Caprioli, R. M., Farmer, T. B. & Gile, J. Molecular imaging of biological  
samples: localization of peptides and proteins using MALDI-TOF MS.  
*Analytical chemistry* **69**, 4751-4760 (1997).
- 416 Hanrieder, J., Phan, N. T., Kurczyk, M. E. & Ewing, A. G. Imaging mass  
spectrometry in neuroscience. *ACS chemical neuroscience* **4**, 666-679,  
doi:10.1021/cn400053c (2013).
- 417 McDonnell, L. A. & Heeren, R. M. Imaging mass spectrometry. *Mass  
spectrometry reviews* **26**, 606-643, doi:10.1002/mas.20124 (2007).
- 418 Philipson, O. *et al.* The Arctic amyloid-beta precursor protein (AbetaPP)  
mutation results in distinct plaques and accumulation of N- and C-truncated  
Abeta. *Neurobiology of aging* **33**, 1010.e1011-1013,  
doi:10.1016/j.neurobiolaging.2011.10.022 (2012).
- 419 Stoeckli, M., Staab, D., Staufienbiel, M., Wiederhold, K. H. & Signor, L.  
Molecular imaging of amyloid beta peptides in mouse brain sections using  
mass spectrometry. *Analytical biochemistry* **311**, 33-39 (2002).
- 420 Seeley, E. H. & Caprioli, R. M. Molecular imaging of proteins in tissues by  
mass spectrometry. *Proceedings of the National Academy of Sciences* **105**,  
18126-18131, doi:10.1073/pnas.0801374105 (2008).
- 421 Carlred, L. *et al.* Probing amyloid-beta pathology in transgenic Alzheimer's  
disease (tgArcSwe) mice using MALDI imaging mass spectrometry. *J  
Neurochem* **138**, 469-478, doi:10.1111/jnc.13645 (2016).



- 422 Rahman, S. M. J. *et al.* Lung cancer diagnosis from proteomic analysis of  
preinvasive lesions. *Cancer research* **71**, 3009-3017, doi:10.1158/0008-  
5472.CAN-10-2510 (2011).
- 423 Bacher, M. *et al.* MIF expression in the rat brain: implications for neuronal  
function. *Mol Med* **4**, 217-230 (1998).
- 424 Metz, C. N. & Bucala, R. Role of macrophage migration inhibitory factor in  
the regulation of the immune response. *Adv Immunol* **66**, 197-223 (1997).
- 425 Michno, W., Wehrli, P. M., Zetterberg, H., Blennow, K. & Hanrieder, J. GM1  
locates to mature amyloid structures implicating a prominent role for  
glycolipid-protein interactions in Alzheimer pathology. *Biochimica et  
biophysica acta. Proteins and proteomics*, doi:10.1016/j.bbapap.2018.09.010  
(2018).
- 426 Chaurand, P. *et al.* Integrating histology and imaging mass spectrometry.  
*Analytical chemistry* **76**, 1145-1155, doi:10.1021/ac0351264 (2004).
- 427 Dufresne, M. *et al.* Multimodal detection of GM2 and GM3 lipid species in  
the brain of mucopolysaccharidosis type II mouse by serial imaging mass  
spectrometry and immunohistochemistry. *Analytical and bioanalytical  
chemistry* **409**, 1425-1433, doi:10.1007/s00216-016-0076-x (2017).
- 428 Thomas, A. *et al.* Histology-driven data mining of lipid signatures from  
multiple imaging mass spectrometry analyses: application to human  
colorectal cancer liver metastasis biopsies. *Analytical chemistry* **85**, 2860-  
2866, doi:10.1021/ac3034294 (2013).
- 429 Soltwisch, J., Jaskolla, T. W., Hillenkamp, F., Karas, M. & Dreisewerd, K.  
Ion Yields in UV-MALDI Mass Spectrometry As a Function of Excitation  
Laser Wavelength and Optical and Physico-Chemical Properties of Classical  
and Halogen-Substituted MALDI Matrixes. *Analytical chemistry* **84**, 6567-  
6576, doi:10.1021/ac3008434 (2012).
- 430 Kaya, I. *et al.* Histology-Compatible MALDI Mass Spectrometry Based  
Imaging of Neuronal Lipids for Subsequent Immunofluorescent Staining.  
*Analytical Chemistry* (2017).
- 431 Huang, T. H., Yang, D. S., Fraser, P. E. & Chakrabarty, A. Alternate  
aggregation pathways of the Alzheimer beta-amyloid peptide. An in vitro  
model of preamyloid. *J Biol Chem* **275**, 36436-36440,  
doi:10.1074/jbc.M005698200 (2000).
- 432 Jiang, D., Rauda, I., Han, S., Chen, S. & Zhou, F. Aggregation pathways of  
the amyloid beta(1-42) peptide depend on its colloidal stability and ordered  
beta-sheet stacking. *Langmuir* **28**, 12711-12721, doi:10.1021/la3021436  
(2012).
- 433 Lord, A. *et al.* The Arctic Alzheimer mutation facilitates early intraneuronal  
Abeta aggregation and senile plaque formation in transgenic mice. *Neurobiol  
Aging* **27**, 67-77, doi:10.1016/j.neurobiolaging.2004.12.007 (2006).
- 434 Philipson, O. *et al.* A highly insoluble state of Abeta similar to that of  
Alzheimer's disease brain is found in Arctic APP transgenic mice. *Neurobiol  
Aging* **30**, 1393-1405, doi:10.1016/j.neurobiolaging.2007.11.022 (2009).
- 435 Tafesse, F. G. *et al.* Sphingomyelin synthase-related protein SMSr is a  
suppressor of ceramide-induced mitochondrial apoptosis. *Journal of cell  
science* **127**, 445-454, doi:10.1242/jcs.138933 (2014).

- 436 Vacaru, A. M. *et al.* Sphingomyelin synthase-related protein SMSr controls ceramide homeostasis in the ER. *The Journal of cell biology* **185**, 1013-1027, doi:10.1083/jcb.200903152 (2009).
- 437 Chalfant, C. E. & Spiegel, S. Sphingosine 1-phosphate and ceramide 1-phosphate: expanding roles in cell signaling. *Journal of cell science* **118**, 4605-4612, doi:10.1242/jcs.02637 (2005).
- 438 Gomez-Munoz, A. Ceramide 1-phosphate/ceramide, a switch between life and death. *Biochimica et biophysica acta* **1758**, 2049-2056, doi:10.1016/j.bbamem.2006.05.011 (2006).
- 439 Cederholm, T., Salem, N. & Palmblad, J. Omega-3 fatty acids in the prevention of cognitive decline in humans. *Adv Nutr* **4**, doi:10.3945/an.113.004556 (2013).
- 440 Calder, P. C. Omega-3 polyunsaturated fatty acids and inflammatory processes: nutrition or pharmacology? *British Journal of Clinical Pharmacology* **75**, 645-662, doi:10.1111/j.1365-2125.2012.04374.x (2013).
- 441 Calder, P. C. Polyunsaturated fatty acids and inflammatory processes: New twists in an old tale. *Biochimie* **91**, 791-795, doi:10.1016/j.biochi.2009.01.008 (2009).
- 442 Amtul, Z., Uhrig, M., Wang, L., Rozmahel, R. F. & Beyreuther, K. Detrimental effects of arachidonic acid and its metabolites in cellular and mouse models of Alzheimer's disease: structural insight. *Neurobiology of aging* **33**, 831.e821-831, doi:10.1016/j.neurobiolaging.2011.07.014 (2012).
- 443 Scheidt, H. A., Morgado, I., Rothemund, S., Huster, D. & Fandrich, M. Solid-state NMR spectroscopic investigation of Abeta protofibrils: implication of a beta-sheet remodeling upon maturation into terminal amyloid fibrils. *Angew Chem Int Ed Engl* **50**, 2837-2840, doi:10.1002/anie.201007265 (2011).
- 444 Kumar-Singh, S. *et al.* Nonfibrillar diffuse amyloid deposition due to a gamma(42)-secretase site mutation points to an essential role for N-truncated A beta(42) in Alzheimer's disease. *Human molecular genetics* **9**, 2589-2598 (2000).
- 445 Kawarabayashi, T. *et al.* Age-dependent changes in brain, CSF, and plasma amyloid (beta) protein in the Tg2576 transgenic mouse model of Alzheimer's disease. *J Neurosci* **21**, 372-381 (2001).
- 446 Kuo, Y. M. *et al.* The evolution of A beta peptide burden in the APP23 transgenic mice: implications for A beta deposition in Alzheimer disease. *Mol Med* **7**, 609-618 (2001).
- 447 Güntert, A., Döbeli, H. & Bohrmann, B. High sensitivity analysis of amyloid-beta peptide composition in amyloid deposits from human and PS2APP mouse brain. *Neuroscience* **143**, 461-475, doi:<http://dx.doi.org/10.1016/j.neuroscience.2006.08.027> (2006).
- 448 Michno, W. *et al.* Pyroglutamation of amyloid-beta(42) (Abeta(42)) followed by Abeta(1-40) deposition underlies plaque polymorphism in progressing Alzheimer's disease pathology. *J Biol Chem*, doi:10.1074/jbc.RA118.006604 (2019).
- 449 Czirr, E. *et al.* Independent generation of Abeta(42) and Abeta(38) peptide species by gamma-secretase. *J Biol Chem* **283**, 17049-17054, doi:10.1074/jbc.M802912200 (2008).



- 450 Paterson, R. W. *et al.* SILK studies - capturing the turnover of proteins linked  
to neurodegenerative diseases. *Nat Rev Neurol* **15**, 419-427,  
doi:10.1038/s41582-019-0222-0 (2019).
- 451 Wildburger, N. C. *et al.* Amyloid-beta Plaques in Clinical Alzheimer's  
Disease Brain Incorporate Stable Isotope Tracer In Vivo and Exhibit  
Nanoscale Heterogeneity. *Front Neurol* **9**, 169,  
doi:10.3389/fneur.2018.00169 (2018).
- 452 Steinhauser, M. L. *et al.* Multi-isotope imaging mass spectrometry quantifies  
stem cell division and metabolism. *Nature* **481**, 516,  
doi:10.1038/nature10734 (2012).
- 453 Zhang, D. S. *et al.* Multi-isotope imaging mass spectrometry reveals slow  
protein turnover in hair-cell stereocilia. *Nature* **481**, 520-524,  
doi:10.1038/nature10745 (2012).
- 454 Arts, M. *et al.* Detection of Localized Hepatocellular Amino Acid Kinetics  
by using Mass Spectrometry Imaging of Stable Isotopes. *Angew Chem Int Ed  
Engl* **56**, 7146-7150, doi:10.1002/anie.201702669 (2017).